Fluid-Electro-Mechanical Model of the Human Heart for Supercomputers

Ph.D. Thesis

Alfonso Santiago

Computer Applications in Science & Engineering dpt.
Barcelona Supercomputing Center (BSC)

Doctorat en Enginyeria Biomèdica
Universitat Politècnica de Catalunya

March 2018

This document is intended to be printed double sided.

Fluid-Electro-Mechanical Model of the Human Heart for Supercomputers

Submited in partial fulfillment of the requirements for the Ph.D. Degree in Biomedical engineering by the Escola Tècnica Superior d'Enginyeria Industrial de Barcelona

Alfonso Santiago

Advisor

Dr. Mariano Vazquez

Cover design

Fernando Cucchetti & Guillermo Marín

Computer Applications in Science & Engineering dpt.
Barcelona Supercomputing Center (BSC)

Doctorat en Enginyeria Biomèdica
Universitat Politècnica de Catalunya

March 2018

A Roby y Magda,
mis otros dos tercios

Agradecimientos

Ir y venir,
seguir y guiar,
dar y tener,
entrar y salir de fase,
Amar la trama más que el desenlace.

Jorge Drexler

Un día escuché que los expatriados son siempre forasteros, tanto en su nueva tierra como de la tierra donde vinieron. Aunque si es cierto que nunca te acabás de sentir como en tu casa en el nuevo país mientras que, a la vez, el lugar donde naciste ya dejó de ser *tu* casa, yo no lo veo así. En Barcelona fui encontrando gente que me hizo de casi-familia disfuncional adoptiva y en Argentina todavía tengo a la familia "que me tocó" y que me reciben con el mayor amor del mundo desde el momento que saben que tengo vuelos para ir.

Por eso, y en orden cronológico quiero empezar por agradecer a mis papás, Claudia y Roberto. La libertad guiada que me dieron me hizo como soy hoy. Tan agradecido como con ellos estoy con mis hermanos, Roby y Magda, chicos, me encantó vivir con ustedes mi infancia.

Mi experiencia de Barcelona es, por lejos, una de las mejores de mi vida. No voy a gastar una hoja entera contando como llegué acá, pero es una de esas historias que me hacen creer que es el lugar donde me tocaba estar. La pieza clave fue mi director. Mariano, ya te lo dije una vez en Petróplolis, en Febrero de 2014. Ahora te lo vuelvo a decir acá: gracias. Gracias por darme la oportunidad de venir, y gracias por el esfuerzo que hiciste estos años por mi. Además, agradezco a todos mis compañeros del doctorado. No los nombro para no dar un orden, pero saben que tienen todo mi cariño. Mi más especial agradecimiento en mi etapa en Barcelona va a Olga y su familia (Jordi, Ángels, Laia, Pol i Marc), que han estado años apoyándome y haciéndome sentir en su casa como si fuera la mía.

Lo que voy a decir ahora parece una joda, pero no lo es. Estoy super agradecido con mi bicicleta, una Peugeot de carretera azul de los 80' que es la envidia de todos los hipsters. Me llevó por todo Barcelona a las chapas,

no se pinchó nunca y solamente me la puse contra un auto una sola vez. Aguante mi bici. También quiero dejar mimos a Rex y Bolu[1], mis dos bichos de Barcelona y que quiero un montón aunque rompan bastante las bolas.

También quiero agradecer a la gente que me guió en las estancias que hice, entre ellos Pablo Blanco y su gente del Laboratorio Nacional de Computación Científica en Brasil y a la gente de Medtronic Minneapolis/Galway: Mark Palmer, Peter Zhang, Joshua and Darell, Jack Lee y Cahal McVeigh. Otro especial reconocimiento va a Ruth Arís que aportó incontables horas a mejorar este documento y a los revisores y jurados: Óscar Cámara, José Félix Rodriguez, Mark Palmer, Eduardo Soudah y Constantine Butakoff.

Antes de terminar, y como muchos de los que agarren este documento no van a pasar de esta página, quiero agradecer a todos los matemáticos, físicos e ingenieros que hicieron posible el mundo de hoy. Día a día nuestra vida es más fácil, cómoda (y hasta posible) gracias a ellos y creo que no son lo suficientemente valorados.

Por ultimo quiero decir que mi doctorado ha sido financiado mediante el apoyo del proyecto EUbrazilCC (614048) de la Comision Europea bajo el programa FP7, el proyecto CompBiomed (contrato nro. 675451) financiado por el programa Horizon 2020 y el ministerio de economía y competitividad bajo el proyecto Severo Ochoa (SEV 2011 00067).

[1] que en paz descanse, pobre Bolu.

Abstract

La ciencia es la expresión de una necesidad inherente al ser humano y, en todo caso, esta ligada a la función superior de su naturaleza inteligente: la capacidad de crear.

René Favaloro

The heart is a complex system. From the transmembrane cell activity to the spatial organization in helicoidal fibers, it includes several spatial and temporal scales. The heart muscle is surrounded by two main tissues that modulate how it deforms: the pericardium and the blood. The former constrains the epicardial surface and the latter exerts a force in the endocardium. The main function of this peculiar muscle is to pump blood to the pulmonary and systemic circulations. In this way, solid dynamics of the heart is as important as the induced fluid dynamics. Despite the work done in computational research of multiphysics heart modelling, there is no reference of a tightly-coupled scheme that includes electrophysiology, solid and fluid mechanics in a whole human heart. In this work, we propose, develop and test a fluid-electro-mechanical model of the human heart.

To start, the heartbeat phenomenon is disassembled in the different composing problems. The first building block is the electrical activity of the myocytes, that induces the mechanical deformation of the myocardium. The contraction of the muscle reduces the intracavitary space, that pushes out the contained blood. At the same time, the inertia, pressure and viscous stresses in this fluid exerts a force on the solid wall. In this way, we can understand the heart as a fluid-electro-mechanical problem.

All the models are implemented in Alya, the Barcelona Supercomputing Center simulation software. A multi-code approach is used, splitting the problem in a solid and a fluid domain. In the former, electrophysiology coupled with solid mechanics are solved. In the later, fluid dynamics in an arbitrary Lagrangian-Eulerian domain are computed. The equations are spatially discretized using the finite element method and temporally discretized using finite differences. Facilitated by the multi-code approach, a

novel high performance quasi-Newton method is developed to deal with the intrinsic issues of fluid-structure interaction problems in biomechanics. All the schemes are optimized to run in massively parallel computers.

A wide range of experiments are shown to validate, test and tune the numerical model. The different hypothesis proposed — as the critical effect of the atrium or the presence of pericardium — are also tested in these experiments. Finally, a normal heartbeat is simulated and deeply analyzed. This healthy computational heart is first diseased with a left bundle branch block. After this, its function is restored simulating a cardiac resynchronization therapy. Then, a third grade atrioventricular block is simulated in the healthy heart. In this case, the pathologic model is treated with a minimally invasive leadless intracardiac pacemaker. This requires to include the device in the geometrical description of the problem, solve the structural problem with the tissue, and the fluid-structure interaction problem with the blood. As final experiment, we test the parallel performance of the coupled solver. In the cases mentioned above, the results are qualitatively compared against experimental measurements, when possible.

Finally, a first glance in a coupled fluid-electro-mechanical cardiovascular system is shown. This model is build adding a one dimensional model of the arterial network created by the Laboratório Nacional de Computação Científica in Petropolis, Brasil. Despite the artificial geometries used, the outflow curves are comparable with physiological observations.

The model presented in this thesis is a step towards the virtual human heart. In a near future computational models like the presented in this thesis will change how pathologies are understood and treated, and the way biomedical devices are designed.

Resumen

El corazón es un sistema complejo. Desde la actividad celular hasta la organización en fibras helicoidales, incluye gran cantidad de escalas espaciales y temporales. El corazón está rodeado por dos tejidos que modulan su deformación: el pericardio y la sangre. El primero, restringe el movimiento de la superficie del pericardio, mientras el segundo ejerce presión sobre el endocardio. La función principal de este músculo, es bombear sangre a la circulación sistémica y a la pulmonar. De esta manera, la deformación del miocardio es tan importante como la fluidodinámica inducida. A pesar de los trabajo publicados en modelado multifísico del corazón, no existe referencia de un esquema fuertemente acoplado que incluya electrofisiología, mecánica del solido y mecánica de fluidos en un corazón humano completo. En esta tesis, proponemos, desarrollamos y probamos un modelo fluido-electro-mecánico del corazón.

Primero, el fenómeno es descompuesto en los distintos subproblemas. El primer bloque componente es la actividad eléctrica de los miocitos los cuales inducen la deformación del miocardio. La contracción de este músculo, reduce el espacio intracavitario, que empuja la sangre contenida. Al mismo tiempo, la inercia, presión y fuerzas viscosas del nombrado fluido inducen una tensión sobre la pared del sólido. De esta manera, podemos entender el latido cardíaco como un problema fluido-electro-mecánico.

El modelo es implementado en Alya, el software de simulación del Barcelona Supercomputing Center (BSC). Se utiliza un esquema multi-código, separando el problema según el dominio en sólido y fluido. En el primero, se resuelve electrofisiología acoplada con mecánica del sólido. En el segundo, fluido dinámica en un dominio arbitrario Lagrangiano-Euleriano. Las ecuaciones son discretizadas espacial y temporalmente utilizando el método de elementos finitos y diferencias finitas respectivamente. Facilitado por el diseño multi-código, se desarrolló un novedoso método quasi-Newton de alta performance, pensado específicamente para lidiar con los problemas intrínsecos de interacción fluido-estructura en biomecánica. Todos los esquemas son optimizados para correr en ordenadores masivamente paralelos.

Se presenta un amplio espectro de experimentos con el fin de validar, probar y ajustar el modelo numérico. Las diferentes hipótesis propuestas

– tales como el efecto producido por la presencia de las aurículas o del pericardio – son también demostradas en estos experimentos. Finalmente, un latido normal es simulado y sus resultados son analizados con profundidad. El corazón computacional sano es, primeramente, afectado con un bloqueo de rama izquierda. Posteriormente, se restaura la función normal mediante la terapia de resincronización cardíaca. Luego, se afecta al corazón de un bloqueo atrioventricular de tercer grado. Esta patología es tratada mediante la implantación de un marcapasos intracardíaco. Para tal efecto, es preciso incluir el dispositivo en la descripción geométrica, resolver el problema estructural con el tejido y resolver la interacción fluido-estructura con la sangre. Como experimento numérico final, se prueba el desempeño paralelo del modelo acoplado. En los casos presentados, los resultados numéricos son comparados con mediciones experimentales, en la medida que es posible.

Finalmente, se muestran resultados preliminares para un modelo fluido-electro-mecánico del sistema cardiovascular. Este modelo se construye agregando un modelo unidimensional desarrollado por el Laboratório Nacional de Computação Científica en Petrópolis, Brasil. A pesar de las geometrías artificiales usadas, la curva de flujo en la raíz aórtica es comparable con observaciones experimentales.

El modelo presentado en esta tesis representa un paso más hacia el corazón humano virtual. En un futuro cercano, modelos como el presentado en este documento, cambiarán la forma en la que se entienden y tratan las enfermedades y la forma en la que los dispositivos biomédicos son diseñados.

Acronyms

A

ADAN Anatomically Detailed Arterial Network. xix, xxvi, 102, 103, 106–108

AHA American Heart Association. xxiii, 1, 57–59

ALE arbitrary Lagrangian-Eulerian. xxi, 11, 21, 23, 26, 27, 39, 51, 52, 76, 77, 112, 113, 116

AV atrioventricular. 4, 88, 92–94, 96, 99, 113, 115

B

BSC Barcelona supercomputing center. 3, 18, 26, 102

C

CFD computational fluid dynamics. xxi, xxiv, xxvi, xxix, 3, 27, 29, 39, 70, 71, 76, 77, 81, 88, 94, 99, 105, 112, 113

CIQN Compact interface quasi-Newton. xxiv, xxix, 41, 47–49, 64–69, 76, 113, 114

CRT cardiac resynchronization therapy. xxv, xxix, 15, 16, 87, 88, 90–92, 113, 115, 116

CSM computational solid mechanics. xxi, xxiv, xxix, 26, 27, 29, 39, 70, 71, 76, 77, 94, 112, 116

CT computed tomography. 117

CVD Cardiovascular disease. 2

D

D-N Dirichlet-Neumann. 39

d.o.f. degrees of freedom. 44

DTI diffusion tensor imaging magnetic resonance. 32

E

ECC excitation contraction coupling. 5, 10, 16, 17, 22

ECG Electrocardiography. xxi, 4, 7, 8, 13, 90, 93

EDV end diastolic volume. xxix, 81

EF ejection fraction. xxix, 81, 88, 91, 92, 113, 115, 116

EP electrophysiology. xxi, 26, 27, 29, 112

ESV end systolic volume. xxix, 81, 91, 92, 113

F

FDA food and drug administration. 20

FEM finite element method. 6, 18, 26, 37, 38

FSI Fluid-Structure Interaction. xxiii, xxiv, xxix, 11–15, 18, 23, 29, 38, 39, 52, 63–69, 71, 76, 92, 102, 104–106, 112, 114–116

H

HPC high performance computing. 14, 26, 69

I

IB immersed boundary. 11, 39, 112, 113, 116

IQN interface quasi-Newton. 41, 42, 44, 47

L

LA left atria. xxi, 3–5

LBBB left bundle branch block. xxv, xxix, 15, 16, 87–92, 113, 115

LNCC Laboratório Nacional de Computação Científica. 16, 102

LV left ventricle. xxi, xxv, xxix, 3–5, 33, 81, 82, 88–91, 100, 113, 121, 123

M

MPI Message Passing Interface. xxii, 27, 40, 47, 48, 70

MRI Magnetic Resonance Imaging. xxv, 8, 12, 29, 80–82, 117

O

ODE ordinary differential equation. 3, 9, 19, 20, 22, 112

P

PDE partial differential equation. 26

R

RA right atria. xxi, 3–5

RV right ventricle. xxi, xxv, xxvi, xxix, 3–5, 33, 81, 82, 88–94, 100, 113, 121

S

SA sinoatrial. 4

U

US United States. 2

V

VMS variational multiscale. 37

Contents

Agradecimientos **vii**

Abstract **ix**

Resumen **xi**

Acronyms **xiii**

1 Foreword **1**
1.1 Motivation 1
1.2 Cardiovascular physiology 3
1.2.1 Anatomy and function 3
1.2.2 Histology of the myocardium 5
1.2.3 The cardiac cycle 7
1.2.4 Relations of the heart 8
1.3 State of the art review 9
1.3.1 The starting point: electrophysiology modelling 9
1.3.2 The evolution: coupled electro-mechanics 10
1.3.3 Whole heartbeat modelling: fluid-electro-mechanics . . 11
1.3.4 Current challenges 12
1.3.5 HPC-based models in cardiac simulations 14
1.4 Goals and contributions of this thesis 14
1.5 Reach of the model presented 15
1.6 Structure of this thesis 16

2 Governing equations **17**
2.1 Heartbeat: three coupled physics problem 17
2.2 Electrophysiology 18
2.3 Solid mechanics 20
2.4 Fluid dynamics 21
2.5 Coupling the physics 22

2.5.1 Excitation contraction coupling and mechano-electric feedback . . . 22
2.5.2 Fluid-structure interaction . . . 23

3 Computational implementation 25
3.1 Alya: HPC-based multi-physics and multi-scale simulation code for supercomputers . . . 25
3.1.1 Code description . . . 26
3.1.2 Programming framework: divide and conquer . . . 26
3.1.3 Modelling pipeline . . . 28
3.2 Computational description of the heart . . . 29
3.2.1 Geometry and spatial discretization . . . 29
3.2.2 Fibre and cell distribution . . . 32
3.2.3 Bi-ventricular version . . . 34
3.3 Computational implementation: The structure domain . . . 35
3.3.1 Electrical wave: electrophysiology modelling . . . 35
3.3.2 Myocardium mechanical deformation: CSM . . . 36
3.4 Computational implementation: The fluid domain . . . 37
3.4.1 Intraventricular blood flow: CFD . . . 37
3.4.2 Deformable fluid domain: the ALE problem . . . 38
3.5 Fluid-structure interaction . . . 39
3.5.1 Computational framework for the FSI problem . . . 39
3.5.2 Added mass instability . . . 41
3.5.3 High performance interface quasi-Newton algorithm . 42
3.5.4 Boundary conditions for the fully coupled fluid-electro-mechanical problem . . . 50
3.5.5 Summary of the fluid-electro-mechanical heart model . 52

4 Basic experiments in simplified geometries 55
4.1 Electrical propagation simulations . . . 55
4.1.1 Mesh convergence . . . 55
4.2 Coupled electro-mechanical simulations . . . 57
4.2.1 Contracting hexahedron: a simple reproducible test . . 57
4.2.2 Sliding pericardium boundary condition . . . 59
4.2.3 Effect of the angle variation in the rule-based model of fibre distribution . . . 63
4.2.4 Mechanical effect of the atrium . . . 64
4.3 Bidirectional fluid-structure interaction test simulations . . . 66
4.3.1 Algorithm validation . . . 67
4.3.2 A biomedically inspired problem: a 3D 2-field case . . 68
4.4 Parallel performance for the fluid-electro-mechanical model . 71

5 Fluid-electro-mechanical simulations in a whole-heart geometry 77
5.1 Computational scenario 78
5.2 Analysis of a healthy systole 79
5.2.1 Description 79
5.2.2 Results 79
5.3 Clinical application I: left bundle branch block 88
5.3.1 Background and description 89
5.3.2 Results 89
5.4 Clinical application II: leadless pacemaker 93
5.4.1 Background and description of the case 94
5.4.2 Results 95

6 Expanding the model: coupling the computational heart with a 1D arterial network 103
6.1 Background 103
6.2 Governing equations 106
6.2.1 For the 3D heart model 106
6.2.2 For the 1D arterial network model 106
6.2.3 Coupling strategy 106
6.2.4 Computational implementation 108
6.3 Numerical experiments 108
6.3.1 A 3D-1D validation case 108
6.3.2 Simplified ventricle coupled with ADAN55 109

7 Conclusions and future lines 113
7.1 Summary 113
7.1.1 Discussion of this thesis chapter by chapter 113
7.1.2 Accomplishments of this thesis 116
7.1.3 Uses for the proposed model: a computational cardiac workbench 117
7.2 Future work 118
7.3 Scientific publications 119
7.3.1 In peer-reviewed journals: 119
7.3.2 In conferences, seminars and workshops: 120

8 Appendix 123
8.1 Appendix I: Results for a left ventricular implanted leadless pacemaker 123
8.1.1 Behavior of the treated heart 123
8.1.2 Analysis of the device-tissues interaction 125

Bibliography **127**

List of Figures

1.1 Anatomy and function. Scheme of a human heart, representing the four chambers left ventricle (LV), right ventricle (RV), left atria (LA) and right atria (RA) and the main vessels that direct the blood in and out the organ. The specialized conduction system is also detailed. Illustration taken from [4]. 4

1.2 Histology of the myocardium. The heart wall. From inside to outside: endocardium, myocardium and pericardium. Image taken from [6]. 6

1.3 Cardiac cycle. Wiggers diagram. Pressure and volume curves associated with the Electrocardiography (ECG) phases. The ventricular depolarization (QRS complex) can be associated with the isovolumic contraction and systole. 7

1.4 Relations of the heart in a transverse view. The heart is located in the center of the mediastinum, with a close relation with the neighboring tissues. Image taken from [15]. 8

2.1 A three physics problem. The system can be decomposed in two bidirectionally coupled problems: the electro-mechanical and the fluid-mechanical one. These two problems can be decomposed in sub-problems leading to three systems of equations to solve: electrophysiology, solid mechanics, and fluid mechanics in deformable mesh. 18

3.1 Alya Framework. Scheme of the multi-code implementation solving the electrophysiology (EP) and computational solid mechanics (CSM) in one Alya instance and another instance solving the arbitrary Lagrangian-Eulerian (ALE) and computational fluid dynamics (CFD) problems in another mesh. 27

3.2 Physical sub-problems Ω_a and Ω_b in contact by the wet surface Γ_c. Each physical sub-problem is subdivided in three computational sub-domains. To be parallelly efficient, communications for the contact surface Γ_c between the sub-problems must be carefully designed. 28

3.3 Modelling pipeline to for pre-processing, simulation and post-processing. 28

3.4 Computational description of the heart. Complete geometry of the original Zygote human heart model [83]. 30

3.5 Computational description of the heart. Left: mesh of the modified version. Center: slice of the geometry showing the filled atrium and the ventricular cavities. Right: Fibre description of the ventricles, top and frontal view. 31

3.6 Element volume distribution for the solid and the fluid mesh. 32

3.7 Fibre an cell distribution form endocardium to epicardium. . 33

3.8 Computational description of the heart. Biventricular geometry overview. 34

3.9 Implementation framework. Schematic trace for the Gauss-Seidel approach The parallel solvers are executed in a block manner. The right side remarks the Message Passing Interface (MPI) communication points in the used scheme. 41

4.1 Electrophysiology set-up. Scheme of the geometry proposed by [126]. 56

4.2 Electrophysiology set-up Left: mesh convergence for a given set of parameters. Right: activation time (isochrones) for a converged simulation. 57

4.3 Electro-mechanical simulations. Scheme for the geometry (proposed in [56]). Starting stimulus point and measuring points are marked. 58

4.5 Electro-mechanical simulations. Left: normalized electrical depolarization and displacement increments (ΔX,ΔY and ΔZ) for the measuring point. Right: simulation snapshots. . 58

4.6 Pericardial boundary condition. The top left figure shows a slice of the geometry and the apex-base unitary vector ($abv_i = (-0.75,\ 0.57,\ -0.327)$ for the original Zygote coordinates). The other figures show a scheme of the 32 segment representation [132] and the correspondent mapping in a frontal and top view of the ventricles. 60

4.7 Effect of pericardium boundary condition in a bi-ventricular geometry. Normalized electrical depolarization is shown as a reference for the reader (A). The following three plots show overall (B), basal (C) and apical (D) longitudinal strain, respectively. Then (E), snapshots at maximum contraction ($t = 120\,[ms]$) for the three boundary conditions are shown. From left to right: Free (F), Base fixed (T), and sliding pericardium (SP). Finally (F), the longitudinal strain is shown in the American Heart Association (AHA) plot segment-wise for each case. 61

4.8 Effect of sliding pericardium in myocardial dynamics. Longitudinal strain measurements captured using speckle tracking echocardiography for a healthy heartbeat. Image taken from [19]. 62

4.9 Effect of the fiber distribution in the bi-ventricular study. The surface plot shows the linear fiber distribution, and the outline shows the cubic fiber distribution. Long and short axis slices are shown for both configurations at $t = 120[ms]$. 63

4.10 Effect of the fiber distribution in the bi-ventricular study. Cubic and linear distributions are compared. Similar basal and apex longitudinal strains are observed, with a appreciable difference in the apical deformation. The overall second invariant, showing the cutting stresses, is also shown. 64

4.11 Mechanical effect of the atria presence. Left side compared a bi-ventricular simulation against the whole-heart undeformed mesh. Right side shows the whole heart simulation against the original mesh. 65

4.12 Mechanical effect of the atria presence. Normalized electrical depolarization is shown for reference, together with base and apex longitudinal strain. The effect of the atria presence can be seen not only in the base, restraining its deformation due to the mass of the added structures but also, with a smaller impact, in the apex. 66

4.13 Method Validation. Part of the domain proposed by [137] in time $t = 3\,[s]$. Deformation is represented on the bar and velocity field in the fluid domain. 67

4.14 Biomedically inspired Fluid-Structure Interaction (FSI) case. Geometry, showing dimensions and fluid direction. 68

4.15 Typical convergence for the coupling. Left: number of coupling iterations for the first 10 time steps. Right: residue of the coupling for the first time step. 69

4.16 Biomedically inspired FSI case. Left: snapshot of the simulation at $t = 0.4$ $[s]$ for the biomechanical inspired case. Right: Accumulated solver iterations in each time step for the best variant in each algorithm family. The different acronyms stand for: atkd, Aitken relaxed in displacement; brdd, Broyden relaxed in displacement; iqnd, Compact interface quasi-Newton (CIQN) relaxed in displacement. 69

4.17 Biomedically inspired FSI case. Top left: coupling iteration distribution. For each candle the middle line represents the median, and the upper and lower lines the 25% and 75% percentiles. Top right: convergence for the Aitken family. Bottom left: convergence for the Broyden family. Bottom right: convergence for the CIQN family. 71

4.18 Massively parallel performance. Speed up and efficiency for the CFD and CSM solvers running separately. 73

4.19 Massively parallel performance. Trace for three iterations of a coupled problem. The same number of cores (p_f and p_s) were assigned the parallel solvers. First, there is an initialization stage (Ini). The solid solver executes (S_{solve}) while the fluid solver waits for the results (F_{wait}), then the fluid portion is computed (F_{solve}) while the solid thread waits (S_{wait}). Once solved both, the coupling iterations (Cou) start to converge the wet surface. Three complete time steps are shown. 74

4.20 Parallel performance analysis. Speed-up and Efficiency for a core allocation of $p = p_f + p_s$, where $p_f = \{256, 512, 1024, 2048\}$ in the core count for the fluid, and $p_s = \{64, 128, 256, 512, 1024, 2048\}$ for the solid. An optimal allocation p_{opt} which allows to achieve the maximum efficiency E_{p_f} of the coupled system can be found for each curve S_{p_f}. 75

5.1 Computational scenario. Wiggers diagram (see Section 1.2.3) for a healthy heart systole showing the simulation time frame. 78

5.2 Analysis of an healthy systole. Simulation snapshots. The deforming slice in the myocardium shows a long axis view, coloured by electrical depolarization. The arrows in the fluid domain shows the velocity field. 80

5.3 Simulation of a healthy systole. Material point tracking in the myocardium. The left side shows the position for the basal, medial and apical slices. In the right, top and side views for the slices. 81

5.4 Simulation of a healthy systole. Ventricular volumes. Top plot shows the ventricular volume as a function of time. The image sequence shows the deformation of the ventricles. . . . 82

5.5 Analysis of a healthy systole. Left: Simulation results for the LV and RV outflows. Right: experimental/modelling curves taken from [143]. the PC-Magnetic Resonance Imaging (MRI) curve is the experimental measurement taken using MRI. The model curve is the numerical result obtained by the cited authors. 83

5.6 Analysis of a healthy systole. Image sequence showing a four-chamber slice in the myocardium and Q-criterion isosurfaces (value of $5000[s^{-2}]$) for the fluid dynamics domain. The isosurfaces are colored by velocity module. 84

5.7 Analysis of a healthy systole. Image sequence similar to Figure 5.6 but using Q-criterion isosurfaces at $50[s^{-2}]$. Please that the scale of the velocity module goes up to $20[cm/s]$. . . 85

5.8 Analysis of a healthy systole. Detail of the ventricular electrical depolarization, deformation and fluid dynamics. . . 86

5.9 Simulation of a healthy heart. Detail of the apical region. The upper row shows the fluid mesh, and velocity arrows. The lower row shows a slice of the geometry, plotting electrical field in the solid domain and velocity in the fluid domain. . . 86

5.10 Analysis of a healthy systole. Image sequence for the aorta showing the co-planar aortic arch output, the brachiocephalic output and the left common carotid artery output. Arrows and colors represents velocity. A short axis view for the aortic root is also shown. In this last view the helical pattern in the aortic root is clearly seen. 87

5.11 Simulation of a healthy systole. Left: MRI 4D flow image taken from [152]. Right: simulation results with the whole heart model. 88

5.12 Left bundle branch block (LBBB). The slice in the myocardium shows that the RV is depolarized first, and the LV is depolarized due to the wave coming from the RV. This dyssynchrony reduces the cardiac output. 90

5.13 LBBB. Basal slice with material points and pathlines. The figure shows the dyssynchrony of the RV and LV. 91

5.14 cardiac resynchronization therapy (CRT) for LBBB. The normalized electrical depolarization (plot A) and ventricular outflow (plot B) is shown for the healthy heartbeat, the LBBB case and the different CRT timings. Outflows for both chambers are also shown. snapshots in plot C shows electrical activation times for the pathological case (LBBB) and the three resynchronization cases. 92

5.15 Leadless pacemakers. Left: Medtronic's Micra and St. Jude's nanostim leadles pacemakers. Both devices are implanted in the RV using different anchoring strategies. 94
5.16 Clinical application II. Geometry of the heart including the implanted leadless pacemaker. 95
5.17 Clinical application II: A leadless pacemaker. The long axis slice shows muscle deformation and is coloured by electrical depolarization. The arrows in the fluid domain show the fluid velocity field. 96
5.18 Clinical application II. Normalized electrical depolarization and ventricular outflow comparing a healthy case with the paced third grade ventricular block. 97
5.19 Clinical application II: A leadless pacemaker. The long axis myocardium slice shows electrical depolarization and muscle deformation. Q-criterion isosurfaces ($5000[s^{-2}]$) coloured by velocity are shown. The apical stimuli gives a distinctive ventricular vortex pattern. The scales are replicated from Figure 5.6 to ease comparison. 98
5.20 Clinical application II: A leadless pacemaker. This figure is presented similarly to Figure 5.19, except that Q-criterion isosurfaces are at $50[s^{-2}]$. This figure is directly comparable with Figure 5.7. 99
5.21 Clinical application II. Von Mises stresses at maximum contraction for the solid mechanics in the apical region, including the device. 99
5.22 Clinical application II. Sequence of images showing a detail of the apical region and the interaction of the leadless pacemaker with the surrounding tissues. 100

6.1 Anatomically Detailed Arterial Network (ADAN)55 model. Left side: whole 1D model. The radius of the arteries are plotted as tubes, so the radius of the vessels can be observed. Right side: detail of the upper part of the model. 104
6.2 Scheme of the coupled problem. The electrophysiology model acts on the solid mechanic problem. The solid mechanics deforms the intracavitary space that pumps out the fluid. This fluid is sent to the arterial network model that returns back a pressure. 105
6.3 Dimensionally heterogeneous model of the cardiovascular system. The scheme shows how the 1D arterial network model is coupled with the fluid-electro mechanical model. In this black-box approach the arterial model is only connected with the CFD problem. 107

6.4 Scheme of the model used in the first numerical test. A 3D cylinder was solved with Alya and a 1D cylinder was solved with ADAN. 109
6.5 3D-1D coupling, validation case. Flow and pressure in the coupling point, next to relative error. 109
6.6 Detail of the results for the coupled cardiovascular model. The ventricle shows depolarization of the myocardium and the 1D model the flow wave. 110
6.7 Simplified ventricle. This figure shows an image sequence of the simplified ventricle that is coupled with the arterial network model. 111
6.8 Coupled cardiovascular model. Flow and pressure in the coupling point, next to the relative error for each unknown. . 111

8.1 Leadless pacemaker in the left ventricle. Normalized electrical depolarization and ventricular outflow for the healthy and the pathologic case. 124
8.2 Leadless pacemaker in the left ventricle.Depolarization, contraction and fluid velocities for the paced heart. 124
8.3 Leadless pacemaker in the left ventricle. The contours show the Q-criteria ($5000[s^{-2}]$), and are colored by velocity magnitude. 125
8.4 Leadless pacemaker in the left ventricle. Detail of the apical region and the interaction of the leadless pacemaker with the surrounding tissues. 126

List of Tables

4.1 Biomedically inspired FSI case. Summary of the experiment. The different acronyms stand for: atk, Aitken family; brd, Broyden family; iqn, CIQN family. If the family name is followed by "displ" it is relaxing the Dirichlet variable; if it is followed by "force", it is relaxing the Neumann variable. In the iqn family, the number of past saved variables can be modified. In this case, five (r5) and twenty (r20) iterations were tested. 70
4.2 Massively parallel performance. Speed up and efficiency for the fluid dynamics CFD and solid mechanics CSM solvers running separately. 72

5.1 End diastolic volumes (EDVs), End systolic volumes (ESVs) and ejection fraction (EF) for the LV and RV for the healthy heart simulation. 83
5.2 CRT for LBBB. Depolarization time, EF for the LV and RV and ESV for both ventricles is shown. 92

Chapter 1

Foreword

La ciencia es sólo un ideal.
La de hoy corrige a la de ayer,
y la de mañana, la de hoy.

José Ortega y Gasset

Summary: This introductory chapter starts describing the economic and social burden produced by the cardiovascular disease. This analysis highlights the importance of the tight relationship between experimental medicine and computational simulations, which is the motivation of this work. After that, a brief description of the cardiovascular physiology is included. In it, a close relationship between the electrical, mechanical and fluid activity can be understood. Regarding the fluid-electro-mechanical simulation, the surrounding tissues are considered critical in this thesis. Understanding the relations of the heart with the neighboring tissues, allow to correctly define the physical problem, providing boundary conditions. Then, a thorough review of the state-of-the-art in cardiac modelling is presented. First, computational electrophysiology is reviewed, followed by electro-mechanical models and finishing with the most complete fluid-electro-mechanical computational simulations. Once understood the reach and limitations of the heart models that are currently under development, goals and reach are defined for this work. This chapter finishes describing the structure of this thesis.

1.1 Motivation

Every year the American Heart Association (AHA) publishes [1] a new revision of the "Heart Disease and Stroke Statistics", with relevant

information on how these pathologies are distributed amongst the worldwide population. Cardiovascular disease (CVD) is the most common cause of death in the world, accounting for an estimate of 17.3 million every year. About 92.1 million adults in United States (US) (more than 30% of the population) have at least one type of CVD. By 2030, a 43.9% is projected to have some form of CVD. Since the begining of the XIX century, CVD accounted for more deaths than any other leading cause in the US. The high prevalence of this type of disease produces immense health and economic burdens in the US and globally, becoming one of the greater problems in public health. It is no surprising that there is a great interest in understanding the heart and vasculature, its normal behavior and how to restore the function after a pathology develops.

It is true that since modern medicine was born, *in-vivo* studies have become essential to understand our body, improve diagnosis methods and develop novel treatment techniques. But it is also true that, since the first computers were developed (even mechanical ones [2]), these machines permeated and improved every field of human interest and physics was not the exception. That was the case of the experimental medicine, which took advantage from studies developed for mechanical engineering. Soft tissues respect the basic postulates like the conservation of mass, momentum and energy and the basic concepts such as stress and strain. Moreover, biomechanics can be defined as the development, extension and application of mechanic purposes to better understanding physiology, diagnosis and treatment of disease. Thus, mechanics of soft tissues owes much to those who led the post second World War renaissance in nonlinear continuum mechanics [3].

While the models become more complex, and the computers more capable, *in-silico* experiments are becoming ingrained in medical research. Nowadays, there are models and supercomputers capable of solving complex physiological events. The advantage of *in-silico* experiments is that they are cheaper, faster and do not have the ethical burden that governs *in-vivo* experimentation. Thanks to this, biomechanical simulations gained great attention from the medical community. Regarding cardiac modelling, computational simulations provide a powerful tool to understand heart function and its behavior under congenital and acquired pathologies. Despite this, such type of computational models are still far away from everyday clinical use.

Modelling the heartbeat is a highly complex task that involves several scales and different tightly coupled problems. A large number of spatial orders of magnitude are linked, from the microscopic cell arrangement into a volumetric description, to the macroscopic shape of the cardiac chambers. In the same way, several temporal scales coexist, from the fast intracellular chemical reactions to the long term remodeling of the heart.

From the engineering point of view, the heartbeat can be decomposed in three different physical problems. In the muscle, the electrical stimuli propagates along the cardiac myocytes, which contract deforming the macroscopic geometry. This produces a change of the volume within the cardiac chambers that are filled with blood. Ventricular computational fluid dynamics (CFD) has to be solved in order to compute the pressure produced by the blood against the endocardium. Since we can decompose the problem in these three sub-problems, we can say that the heartbeat is a fluid-electro-mechanical phenomenon. Each one of these sub-problems is computationally demanding by itself. On the one hand, non-linear ordinary differential equations (ODEs) governs the electrical propagation and an exponential orthotropic material models the myocardium solid mechanics. On the other hand, large deformation occurs in the fluid domain with step changes in the velocities. When these problems are coupled, the computational cost multiplies making supercomputer resources a requirement to solve the proposed model.

Due to the previously exposed reasons, modelling the heartbeat requires, not only knowledge about the anatomy and physiology of the heart, but also experience in multi-physics modelling and massively parallel programming. This is why the Barcelona supercomputing center (BSC) CASE (Computer Applications in Science and Engineering[1]) department is the ideal place to develop a model with such features. The CASE department is composed by programmers, physicists, engineers and bioengineers providing a truly multi disciplinary work environment to develop an HPC-based, fluid-electro-mechanical model of the whole heart. Motivated by clinician's questions, we design computational experiments that show the impact of the proposed model in clinical applications.

1.2 Cardiovascular physiology

1.2.1 Anatomy and function

Brief anatomical description The heart is a remarkably complex and efficient mechanical pump, designed to deliver blood to the entire body through the circulatory system. The structure of the heart can be differentiated in right and left, atrium and ventricles resulting in four quadrants: right atria (RA), right ventricle (RV), left atria (LA) and left ventricle (LV). These four chambers compose two serial-connected pumps. Four valves regulate the fluid path in the heart. The tricuspid and mitral valves produce an unidirectional flow from the atrium to the ventricles for the right and left sides respectively. The aortic and pulmonary valves regulate the flow from the ventricles to the vessels, which guide the blood flow to the

[1] Visit `bsc.es/discover-bsc/organisation/scientific-structure/case`

systemic or pulmonary circulation. For a graphic reference see Figure 1.1.

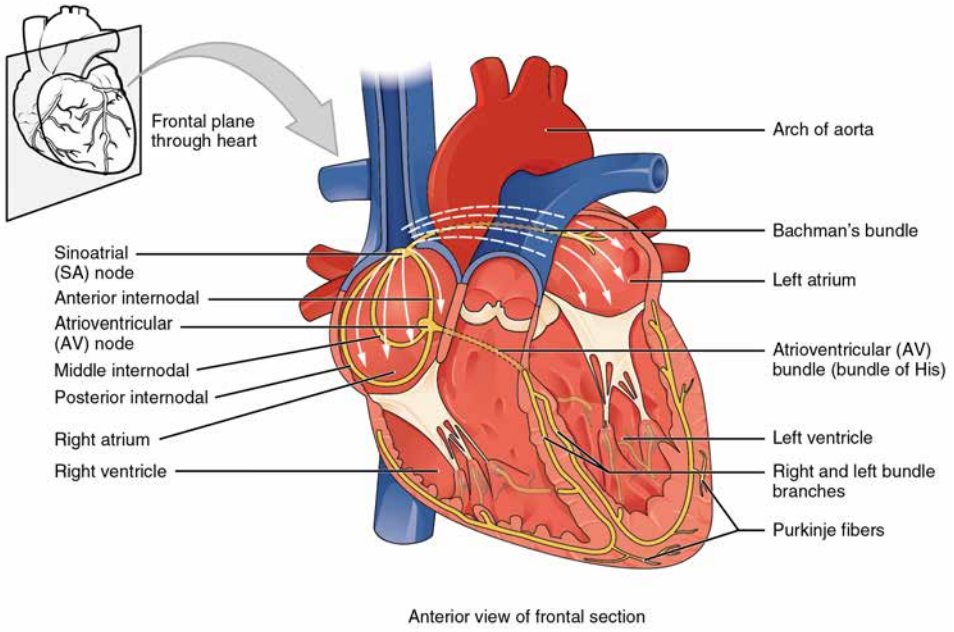

Figure 1.1: Anatomy and function. Scheme of a human heart, representing the four chambers LV, RV, LA and RA and the main vessels that direct the blood in and out the organ. The specialized conduction system is also detailed. Illustration taken from [4].

Heart depolarization is orchestrated by the specialized conduction system, that is in charge to synchronously depolarize the four chambers (for a graphical reference see Figure 1.1). It is composed by the sinoatrial (SA) node, the internodal fibers, the atrioventricular (AV) node and the Purkinje fibres. The SA node, which is located in the RA, paces the rest of the system and triggers the depolarization of both atria. The AV node is located under the valvular plane and delays the propagation of the wave (about $120\,[ms]$), so the atrial contraction can fill the ventricles. After that delay, the AV node starts the action potential that is conducted by the Purkinje network and almost instantaneously depolarizes the left and right endocardium, leading to systole. Factors like blood pressure, oxygen saturation, and humoral and nervous stimuli modulate the action of the SA, regulating the depolarization frequency. Human heartbeat rate varies from $60 - 90\,[bpm]$ (beats per minute) at rest, up to $200\,[bpm]$ at intense exercise. The electrical activity of the heart can be easily visualized with an Electrocardiography (ECG). In this technique, with surface electrodes in the patient skin, the different phases of the electrical activity can be seen.

Function of the heart The vascular system carries the blood from the heart to every part of the human body. Oxygenated blood nourishes the tissues and removes CO_2 by reducing hemoglobin. This deoxygenated blood flows through the venous system up to the RA. This chamber acts as a distensible venous reservoir. From the RA the blood flows to the RV during diastole. Then, with a ventricular contraction, this deoxygenated blood moves out of the RV to the pulmonary artery. Once oxygenated by the lungs, the blood returns to the heart through the pulmonary veins to the LA. With the atrial contraction, the blood moves through the mitral valve to the LV. Finally, during systole, a fraction of this blood is ejected out of the LV to the aorta through the aortic valve.

From the paragraph above, we can understand the heart as two serially connected pumps. The right heart receives low pressure, deoxygenated blood from the systemic circulation and sends it to the pulmonary circulation. The left heart receives low pressure, oxygenated blood from the lungs and sends it into the high-pressure systemic circulation. Both sides of the heart beat in perfect synchrony. When this does not occurs, the efficiency of the pump is drastically reduced [5].

1.2.2 Histology of the myocardium

Histology is defined as the study of the fine structure of tissues [3]. Thus, histological description of the myocardium is also critical for the cardiac function.

Myocytes: the unitary building block The heart muscle is mainly composed by myocytes. These are long tubular cells with two main functions: electrical conduction and contraction. The former happens, mainly, in the cell membrane as a consequence of the induced transmembrane currents. When this surface is depolarized, an all-or-nothing process starts where the electrical impulse is spread all along the cell. The contraction of the myocyte happens exclusively in the interior of the cell, the so called cytoplasm or sarcoplasm. Myocytes are filled with myofilaments, that are long protein structures that reacts with the presence of Calcium ($[Ca^{+2}]$) released by the sarcoplasmic reticulum, once the cell membrane is depolarized. This process is called excitation contraction coupling (ECC).

The heart wall It is generally accepted that the heart can be decomposed in three layers, from the inside to the outside: the endocardium, the myocardium and the epicardium (see Figure 1.2).

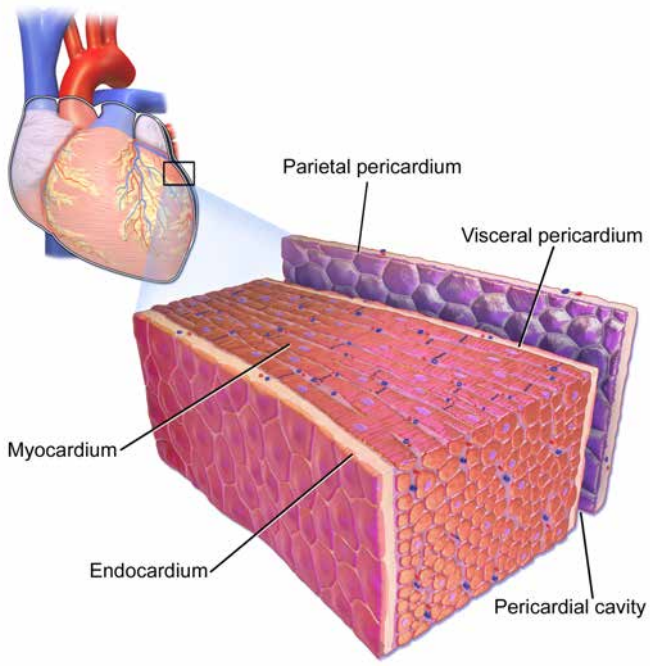

Figure 1.2: Histology of the myocardium. The heart wall. From inside to outside: endocardium, myocardium and pericardium. Image taken from [6].

The myocardium can be characterized as an orthotropic material, with a longitudinal preference in the electrical conduction and the generated stresses. Due to this, cell distribution is a major determinant in how the muscle depolarizes and contracts (see Section 3.2.2 for a detailed description). This has been described [7, 8] as an helicoidal fibrous structure with transmural angle variation from $-60°$ to $60°$. Beside the variation in the fibre distribution, histological differences can be found from endocardium to epicardium, and in apex-base direction [9, 10, 11, 12]. The fibre distribution in the atrium has also been described [13], but with a more complex and less organized pattern. Due to the orthotropic characteristic of the tissue, this histological description affects both, the electrical depolarization and the muscle deformation.

The heart and the continuum hypothesis From the description above, it is valid to question if myocardial contraction can be modeled by continuum mechanics. An average myocyte has a diameter $25[\mu m]$, a length of $100[\mu m]$ [14] and a $490[\text{p}m^3]$ volume. This means that in a cube with side equal $1[mm]$ (and volume equal to $1[mm^3]$) fits about 20000 myocytes. The continuum hypothesis, in which is based the finite element method (FEM) technique used in this work, assumes that the unitary spatial discretization behaves exactly as the macroscopic geometry. Therefore, if we consider that

20000 myocytes behaves as a characterizable continuum material, a spatial discretization of $1[mm^3]$, is compliant with the continuum hypothesis.

1.2.3 The cardiac cycle

Te cardiac cycle is composed by the periodic filling of the ventricles and the subsequent ejection of blood. It can be split in four different phases: diastole, isovolumic contraction, systole and isovolumic relaxation (see Figure 1.3).

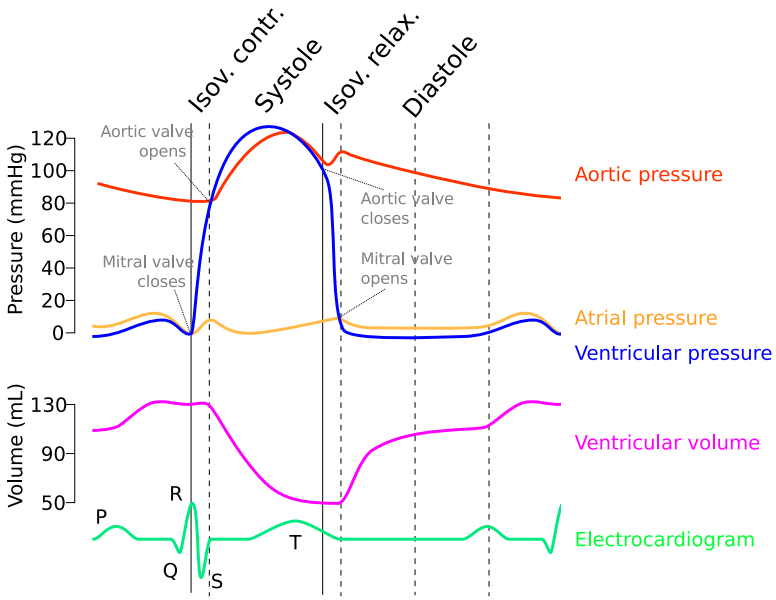

Figure 1.3: Cardiac cycle. Wiggers diagram. Pressure and volume curves associated with the ECG phases. The ventricular depolarization (QRS complex) can be associated with the isovolumic contraction and systole.

Description of the cycle Diastole, is the portion of the cycle when the atrium fills the ventricles. This is, mainly, caused by the pressure difference between the upper and the lower chambers, but also by the atrial kick. The isovolumic contraction is a short phase after the ventricles start contracting when the intracavity pressure rises without changing volume. Once the intraventricular pressure rises above the pressure on the vessels, the valve opens initiating the systole. This phase occurs until the pressures in the ventricle and the aorta are equilibrated again, closing the aortic and pulmonary valves. This leads to the isovolumic relaxation of the ventricles, where the intracavitary pressure decays with a constant volume. This phase finishes when the ventricular pressure is low enough to open the atrioventricular valves and let the blood flow from the atrium to the ventricles.

The ECG These phases are closely related to the ECG as they are a consequence of the electro-mechanical activity of the myocardium. The ECG plot has three main features: the P wave, the QRS complex, and the T wave. P wave is produced by the auricular depolarization, the QRS complex is due to the ventricular depolarization and T wave in produced by the ventricular re-polarization. The reader may note that the description lacks of an auricular repolarization, but this small wave is hidden in the QRS complex.

1.2.4 Relations of the heart

The surrounding structures of the heart have a critical function as they modulate the deformation of the muscle, affecting the way the heart beats. The organ is located in the mediastinum in contact with the lungs, the diaphragm, and the great vessels. It is in intimate relation with the pericardium, a thin fibrous membrane that covers the organ and modulates the ventricular deformation. Between the pericardium and the epicardium, we can find a fluid that lubricates the contact between both surfaces.

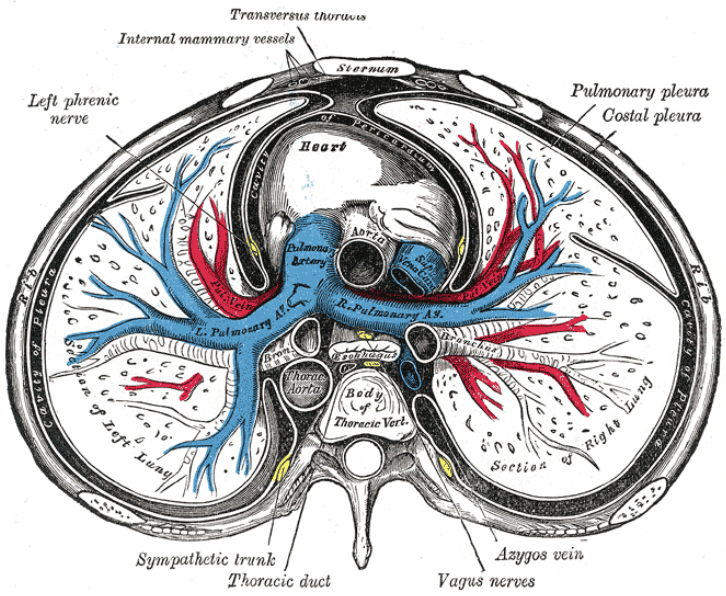

Figure 1.4: Relations of the heart in a transverse view. The heart is located in the center of the mediastinum, with a close relation with the neighboring tissues. Image taken from [15].

Recently developed imaging techniques as speckle tracking [16] echocardiography and diffusion tensor Magnetic Resonance Imaging (MRI) [17, 18] give a deeper understanding of cardiac mechanics [19, 20]. These new imaging techniques confirmed that, due to the described histological and

mechanical conditions, the ventricular contraction involves the base of the heart rather than the apex. The basal plane moves in base-apex direction, with a slight torsion of the ventricles due to the helicoidal structure of the fibres [20]. This twisting creates an energetically efficient swirling effect in the ventricular flow [21, 22]. Due to the pericardium [20], the epicardium has barely not normal displacement, while is free to move in the tangential direction.

1.3 State of the art review

1.3.1 The starting point: electrophysiology modelling

Historically speaking, the first steps in computational heart modelling were in models of the electrical activity of the heart. The first electrophysiology cell model, described by Hodgkin and Huxley [23], made the authors winners of the Nobel prize in medicine (1963). This set of equations described the transmembrane voltage and ionic currents in an axon.

The electrophysiology models rapidly evolved from axon model to tissue-specific models. By 1961 the first phenomenological set of equations for cardiac cells appeared [24]. These models reproduce the shape of the electrical voltage in the cell membrane, but they cannot give information about the transmembrane currents. Due to their relative simplicity, phenomenological models become widely used and evolved with more complex and detailed descriptions [25, 26]. For some applications, where the ionic currents are required to faithfully reproduce the event under study [27], phenomenological models are extremely oversimplified.

Cell models were the following step in electrophysiology simulations. Nowadays, authors proposing this type of equations create the models fitting ODEs to experimentally measured transmembrane currents. Today most complex cell models include a wide range of transmembrane ionic currents measured in dog [28] or human [29] tissue. These complex models are used to simulate the electrical activity of the heart in normal conditions and under complex chaotic depolarization patterns like re-entrance [30, 31, 32].

Despite cell models are preferred due to the high detail of the transmembrane currents, these are more computationally expensive and rely on a large set of parameters difficult to personalize. Due to this, phenomenological models are still popular. In this way, the electrophysiological models used nowadays can be classified in phenomenological and cell models. An extensive review on electrophysiology models can be found in [33].

1.3.2 The evolution: coupled electro-mechanics

Despite the intrinsic difficulty behind these simulations, electrophysiology is only one portion of the heartbeat problem. The electrical activity of the cells is occurring in a solid domain that is deforming. In this way, the mechanical deformation of the tissue is as important as the electrical activity.

When modelling the solid mechanics of the heart, two sources of stresses should be accounted, the passive and active portion. Passive stresses are a consequence of the structural properties of the cells and the connective tissues. Active stresses are a consequence of the electro-mechanical activity of the heart. The final stresses produced in the tissue are obtained adding the passive stresses ($\boldsymbol{\sigma}_{pas} = \sigma_{ij}^{pas}$) and the active stresses ($\boldsymbol{\sigma}_{act} = \sigma_{ij}^{act}$).

Modelling passive stresses Soft tissue passive cardiac mechanics, evolved parallely to the electrophysiology models. From early stages [34] soft-tissue behavior was described as non-linear over finite strains. Despite this, the simplicity and familiarity of the linearized theory, induced the first soft-tissue models to be linear [35, 36]. Soon after [37], soft tissue biomechanics was placed within the framework of finite elasticity. In 1973 the first model of arterial and ventricular stresses was developed [38]. Nowadays, the great majority of the models [39, 40] are based on the 1981 Yin [41] model. These modern models also include some type of orthotropic properties derived from the known helicoidal fibre distribution of the heart [7].

Coupling the active stresses When the first models of active stress generation appeared, electrophysiology and passive tissue behavior crossed roads. ECC is the phenomenon in which the membrane depolarization induces a mechanical response in the myocytes. So the first active stress models [42] were, in some way, voltage-stress transfer functions. Although there are various models for ECC, none enjoys widespread acceptance [43, 44]. Both, passive stress models and ECC models, quickly evolved allowing complex computational experiments in cardiac electro-mechanical modelling [45, 46, 47, 48].

Bidirectional electro-mechanical models ECC is a two side problem. Electrical activity induces mechanical deformation but, also, mechanical stimulus can also induce transmembrane currents that develop in electrical activity. *E.g.* it has been proven [49] that ventricular filling slows down epicardial conduction and increases action potential duration. Also, in [31], the authors demonstrate that mechanical deformation could affect complex electrophysiological phenomena like spiral wave breakup. This effect, where mechanical stimulus induce electrical activity, is called mechano-electric feedback. This is a complex phenomena and only a few models exist for

such behavior [50, 48, 51].

1.3.3 Whole heartbeat modelling: fluid-electro-mechanics

Great advances has been done in electro-mechanical modelling. Despite this, the main function of the heart is pumping blood. This fluid exerts a force in the endocardial wall that have to be computed to know the precise solution to this problem. Also, in some cases, the electro-mechanical activity of the heart is not the focus of interest, but the focus is in the intracavitary fluid dynamics. If a more accurate solution for the solid mechanics is required, or the interest is in the intracavitary flow, ventricular fluid dynamics should be computed. This phenomenon, where the fluid exerts a force on a solid that deforms and modifies the fluid solving domain is called Fluid-Structure Interaction (FSI). Although great advances has been done in the independent fields (electro-mechanical simulations and in FSI) fluid-electro-mechanical models of the heart are unusual, even for single-ventricle geometries. We acknowledge that efforts are being carried out on this line by a few groups worldwide, although hitherto published references are not existent to the authors knowledge.

Two ways to solve the FSI problem Once the electro-mechanical simulations were mature enough, and FSI techniques were sufficiently complex to deal with highly deformable domains, the first partial fluid-electro-mechanical models appeared. Two popular FSI techniques are generally used in biomechanics (for a further explanation see Section 3.5). The arbitrary Lagrangian-Eulerian (ALE) method deforms the fluid mesh using imposed boundary displacements. The immersed boundary (IB) technique uses a fixed mesh in the fluid and interpolates the wet surface position from the Lagrangian solid mesh. These methods can be one-way, or bidirectional. If the method is one way, only displacements are transferred from the solid to the fluid. If the technique is bidirectional, there is also communication from the fluid to the solid, requiring iterations to converge position and force in the contact boundary.

Review on fluid-electro-mechanical models of the heart The simplest approach to solve the FSI problem of the heart, is to use a one-way FSI coupling. In this technique, the electro-mechanical simulation computes the deformation of the mesh, and these boundary displacements are imposed in the deformable fluid domain, technique used in [52, 5, 53]. With this approach, forces computed by the fluid dynamics solver are not imposed in the solid wet boundary. This feature is required to correctly reproduce the involved physics. Despite all the efforts done, there is only one documented case of a bidirectionally coupled FSI model of the ventricles [54]. In both

unidirectional and bidirectional cases, Navier-Stokes equations are solved in the fluid domain to compute fluid dynamics. In one exceptional (and arguable, as [55] explains) unidirectional case [56] a turbulence model is also included.

The overall complexity of the fluid-electro-mechanical model of the heart, not only lies in the type of FSI method. On the contrary, each one of the building blocks contribute to the completeness of the overall model. *E.g.* some models [52, 54] use phenomenological models like the Fitzhugh-Nagumo [24], and others [56], use more detailed cell models like the Tentusscher [57].

To sum-up, the most advanced coupled fluid-electro-mechanical model so far is that of the University of Tokyo, known as UTHeart (University of Tokyo Heart simulator) [54, 58, 59], where a bi-ventricular geometry is used as simulation scenario. In [5], the authors present a model based on cable methods for a heart, where a complete model is solved in simplified geometries. Finally, in [53] and in [56] a one-way FSI model is solved in a single-ventricle scenario.

Importance of the solving domain Finally, there are other two important aspects to consider in the heart simulation: geometry and spatial discretization. In the reviewed literature, single and bi-ventricular geometries are the most frequent scenario in electrophysiology, electromechanical or fluid-electro-mechanical cardiac modelling. In [53] and [60] the authors take a step further, creating the biventricular geometry from MRI images. Although bi-ventricular domains are very useful for electrophysiology, these type of geometries present important disadvantages when used for electro-mechanical simulations. Moreover, when simulating fluid-electro-mechanical models, the problem becomes more apparent, rendering them almost useless for such multi-coupled cases. The reason is evident: the richer the physics included in the problem, the higher the requirements of geometry definition. For instance, such kind of incomplete geometries do not contract in a realistic way because mechanical behavior require the missing parts to impose boundary conditions and to consider mechanical inertia. In this way, we suggest that a 4-chamber geometry is required for a more accurate simulation of the heart. Only in one case, the authors use a four-chamber model, but with an oversimplified geometry [5]. Spatial discretization is also important; a coarse mesh as the used in [58] does not allow to visualize details in electrical depolarization or ventricular flow. Both, geometry and spatial discretization, contribute to the completeness of the heart model.

1.3.4 Current challenges

Great advances have been achieved in heart modelling from the first electrical wave propagation simulations. Current models are incremental evolutions

from previous, slightly simpler stages. Creating a fluid-electro-mechanical model of the heart is a new required stage to improve heart models. Despite all the efforts done, none of the models cited above include all the physics involved in the heartbeat –electrophysiology, solid mechanics and fluid dynamics– in a whole-heart geometry.

FSI, the Achilles' heel of current models Almost all the cited works choose for a one-way FSI, as this approach eases implementation and convergence. The downside of this technique is that it does not faithfully reproduces the FSI physics, as the phenomenon is lacking the bidirectional response. When using a bidirectional approach for the FSI problem, fluid forces are imposed in the solid boundary, modifying the solid domain solution. Using this FSI coupling approach in soft tissues is challenging due to the numerical instabilities that may arise (see Section 3.5) and the associated computational cost. At the same time, complex models have to be solved in both sides: the fluid and the structure. Highly non-linear phenomenon occurs in the myocardial tissue, while a large mesh displacements and step changes in velocities are induced in the blood. From the description above, it can be understood that supercomputing resources are required for a model with all the desired features.

Simulations on *heart* geometries In the reviewed bibliography, it seems that the solving domain is underestimated. Great efforts are done in creating complex models for the involved phenomena but, then, less importance is given to the solving domain.

Creating computational geometries from medical images is a challenging area by itself, as it requires a very handcraft work from the medical image to the computational mesh. Despite this, obtaining an accurate and complete description of the whole organ is important for a faithful physical description.

Importance of the three-physics The heart has three different tightly-coupled physical systems: the electrical, mechanical and fluid dynamics. Physicians evidence this three-way coupling on a daily basis. The ECG, which measures electrical potentials in the skin of the patient, can be used to diagnose mechanical pathologies like myocardial hypertrophy [61]. In the same way, a reduced ventricular output can have an electrical or mechanical etiology. Electrophysiology or electromechanical models are useful when analyzing localized events in the heart (for a deeper discussion see Section 1.5). But, if a more extensive overview in the heartbeat phenomena is expected, it is required to increase the model complexity including the blood fluid dynamics. As Lee et al[62] states: "*(...) these separated models are limited. Both types of decoupled models are hindered by the need of a detailed a priori knowledge of the forces or dynamics of the*

fluid/solid interface, effectively requiring that the dynamic interplay between fluid and solid be prescribed (...)". Adding the FSI model not only makes the model more accurate, but also provides a new set of data to evaluate heart function and compare with experimental measurements. Due to this, the main goal of this work is to provide a complete computational model of the human heart.

1.3.5 HPC-based models in cardiac simulations

Each one of the independent problems (electrophysiology, solid mechanics and fluid dynamics) is, by itself, computationally demanding. When these problems are coupled, computational costs grows more than the sum of the independent parts. For this reason, efficient and scalable solvers for each problem are required, together with a proven performance for the coupled model. There are four reasons that justify the high computational cost and the requirement of supercomputing resources for fluid-electro-mechanical simulations of the whole heart:

- Non-linear material model for solid mechanics.
- Fluid dynamics modelling.
- Implicit coupling for the FSI problem.
- Mesh refinement to capture geometry details.

Despite this, parallel performance for cardiac biomechanics has not been extensively developed in the bibliography. In [63] the authors present a detailed high performance computing (HPC) study for an electrophysiology model, aimed to obtain clinical time-scales. In [59], the authors analyze how to extend the flud-electro-mechanical model presented to more complex cases using HPC techniques, but the named improvements are never presented.

1.4 Goals and contributions of this thesis

Goals The main goal of this work is to present a fluid-electro-mechanical model of the human heart and show potential clinical applications for it. The work done during this Ph.D. thesis differentiates from other publications mainly for two reasons:

a. A whole heart geometry is used to run the simulations.

b. The FSI scheme used to couple both domains is bidirectional.

Despite this two facts, the combination of other features makes this work noteworthy compared with other previous publications. To summarize, the presented model includes:

- A human cell electrophysiology model.
- A ventricular solid mechanic model, including passive and active stresses.
- Intracavitary fluid dynamics bidirectionally coupled with the solid mechanics problem.

This three problems are solved in a whole heart geometrical description. This geometry includes ventricles, atria, great vessels, a rule-based fibre description and boundary conditions based in published experimental observations. This multi-physics model of the human heart is used to model and analyze:

- A healthy heartbeat.
- A left bundle branch block (LBBB) model.
- A cardiac resynchronization therapy (CRT) treatment for the LBBB case.
- A heart beating as a consequence of an intracavitary pacemaker and the impact produced in the surrounding tissues.

Contributions The top contributions of this thesis, are:

- An FSI coupling algorithm capable of dealing with the instabilities present in biomechanical simulations.
- A fluid-electro-mechanical model of a whole human heart.
- The analysis of the model in healthy and pathological conditions, comparing the numerical results with published experimental data.
- A simplified version of a coupled cardiovascular system including heart and main arteries.

1.5 Reach of the model presented

In this thesis, the heartbeat is understood as a tightly coupled multi-physics problem. With the experiments presented ahead, we prove that the heart model is able to simulate a systole including all the involved physics: electrophysiology, solid mechanics, and fluid dynamics. Despite these facts, a fluid-electro-mechanical in a whole heart model is not always necessary. The requirements of the used model depend on two factors: *(1)* the initial hypothesis and *(2)* the purpose of the study.

(1) **Initial hypothesis** The features of the chosen models must fit and be able to reproduce the assumptions made in the simulation design stage. Also, the hypothesis made for one model should be extrapolated to the remaining models. For example, if a bidirectional electro-mechanic model is used [50, 48, 51], special care must be taken in the solid boundary conditions and body forces. With this we mean that, if such a detailed ECC model is used, the same level of detail has to be used in the other solid mechanic forces, as the pressure computed by the blood. As [49] shows, cardiac filling affects repolarization of the ventricle.

(2) **Purpose of the study** In the same way, the variables to solve and measure should be coherent with the needs of the ongoing work. For instance, computing the aortic root blood flow seems unnecessary if the objective is to study the re-entrance phenomena [27] produced by an ischemic scar [64].

A general rule cannot be made, but this hypothesis-method-objectives coherence should stand. In the two clinical cases presented in this thesis, a three-physics model is mandatory. For the LBBB and CRT cases (Section 5.3), an electrophysiology-only approach would give a partial understanding on the pathology and the treatment, as explained in the results of the cited experiment. Even though an electrophysiology-only model can show the resynchronization of both ventricles, it cannot reflect that improvement in the cardiac output. In the same way, the fluid-electro-mechanical model is required for the leadless pacemaker case (Section 5.4). An electro-mechanic model for this problem would not be able to reflect the fluid effect against the device.

1.6 Structure of this thesis

This document is organized as follows. First, in Chapter 1, we have introduced this thesis, cardiac anatomy, the different physical problems involved, and the state of the art in cardiac modelling. In Chapter 2 the continuum equations for the different physical problems are described. Following, in Chapter 3, the governing equations are translated to the discrete temporal/spatial domain, explaining the computational implementation for the involved models. After this, in Chapters 4 and 5 we present a series of numerical experiments to validate and test the methods developed. In the same chapter, results for the fluid-electro-mechanical model of the heart are shown. Then, in Chapter 6, we present a first glance on a cardiovascular coupled model, developed together with the Laboratório Nacional de Computação Científica (LNCC) in Petropolis, Brasil. Finally, in Chapter 7, we close this work discussing the results and showing the scientific contributions and proposing future research lines from this work.

Chapter 2

Governing equations

Poets say science takes away
from the beauty of the stars
- mere globs of gas atoms.
I too can see the stars
on a desert night,
and feel them.
But do I see less or more?

Richard Feynman

Summary: In this chapter the continuum equations that model the human heartbeat are described. The problem is analyzed as a three coupled physics system. First of all, each one of composing problems are described, electrophysiology, solid mechanics and fluid dynamics in a deformable domain. After that, the equations that model the coupling points between the different building blocks are shown.

2.1 Heartbeat: three coupled physics problem

In Chapter 1 we described the heartbeat as phenomena that can be decomposed in three, more simple coupled problems: *(a)* the electrical depolarization, *(b)* the solid mechanics and *(c)* the fluid dynamics. These three problems are tightly related, and must be solved in a coupled way. In the previous chapter, we saw that the propagation of the electrical depolarization in the muscle cells induces the mechanical deformation of the myocardium in a process called excitation contraction coupling (ECC) (see Section 1.2). Also, we saw that the intracavitary and vascular fluid dynamics is induced by the deformation of the ventricular cavities and, as a reaction, the fluid exerts a force against the solid wall. From the description

in the previous lines, we identify two coupling points. On the one hand we have the electro-mechanical coupling between the electrophysiology and the solid mechanics models. On the other hand, we have the bidirectional structure-fluid coupling, frequently called Fluid-Structure Interaction (FSI).

Breaking the heartbeat apart To ease the analysis and implementation of the three problems, we can categorize them depending on the domain they are solved. Electrophysiology and solid mechanics are solely solved in the myocardium, this is to say the solid or structural domain. On the contrary, the fluid dynamics problem is only solved in the deformable fluid domain. Figure 2.1 shows a graphical reference for a problem splitting as the described above. The arrows represent the coupling points, and the dotted lines the two bidirectional problems.

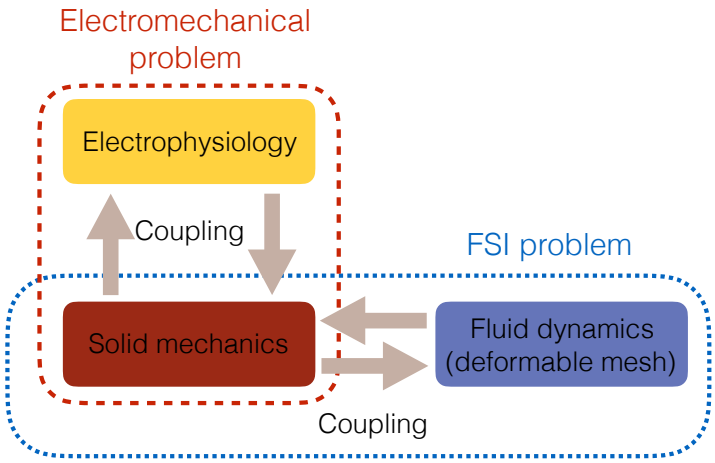

Figure 2.1: A three physics problem. The system can be decomposed in two bidirectionally coupled problems: the electro-mechanical and the fluid-mechanical one. These two problems can be decomposed in sub-problems leading to three systems of equations to solve: electrophysiology, solid mechanics, and fluid mechanics in deformable mesh.

All the equations described in this chapter, are temporally and spatially discretized with the techniques described in Chapter 3 and implemented in Alya, the Barcelona supercomputing center (BSC) in-house workbench for finite element method (FEM).

2.2 Electrophysiology

The electrical depolarization of the heart is orchestrated by the specialized conduction system (see Section 1.2.1), which regulates heart rate and synchronous depolarization. When talking about normal ventricular

depolarization, the phenomena starts in the Purkinje network, that guides the electrical impulse to almost every point of the ventricular endocardium, initiating the depolarization of the myocardium.

Once a few myocytes are excited, a so called all-or-nothing process starts, where the induced electrical wave propagates to the whole heart. There is evidence that, at cell scale, the action potential propagation is a discrete process [65]. However, at larger spatial scales (few thousands cells) depolarization appears to propagate smoothly [66]. A common and important assumption is that this discrete nature can be neglected, and propagation can be considered as continuous. Therefore, cardiac tissue behaves as a functional syncytium, supporting propagating waves of depolarization and repolarization. Due to this, the electrical propagation phenomenon can be modeled under the continuum mechanics hypothesis.

Equation for the wave propagation Once the tissue is depolarized and the all-or-none barrier for the cell model is surpassed, the ionic currents along the membrane produce the action potential that travels along the fibres. The equation for the electrical activation potential ($\boldsymbol{\phi}$) propagation reads:

$$C_m \frac{\partial \boldsymbol{\phi}}{\partial t} + \frac{\partial}{\partial x_i}\left(\frac{G_{ij}}{S_v}\frac{\partial \boldsymbol{\phi}}{\partial x_j}\right) + I_{ion}\left(\boldsymbol{\phi}\right) = 0, \tag{2.1}$$

where $\boldsymbol{\phi}$ is the activation potential and S_v the surface to volume ratio. The left-hand side is the tissue propagation model that is based on the continuum cable equation. The conductivity tensor G_{ij} comes from the transversally isotropic fibre-like structure of the tissue. The anisotropic tensor is computed by rotating the material fiber framework to the global system using transformation matrix T_{ij}, resulting in:

$$G_{ij} = T_{ik}\, G^{\mathrm{d}}_{kl}\, T^{-1}_{lj}, \tag{2.2}$$

where G^{d}_{kl} is the fibre conductivity for the material coordinates. The conductivity tensor G_{ij} can also be written as:

$$G_{ij} = g_0\left[(1-r)n_i n_j + r\delta_{ij}\right], \tag{2.3}$$

where g_0 is the conductivity along the fibre, n_i is a vector defining the fibre direction r is transverse/longitudinal conductivity ratio and δ_{ij} the identity tensor. In Equations (2.1) and (2.2) the Latin subscripts label the space dimension. C_m and S_v are the membrane capacitance and the surface-to-volume ratio model constants, respectively. Diffusion governs the passive propagation of the wave over the tissue. The reactive part I_{ion} is modeled by a set of ordinary differential equation (ODE) and is what, in the end, forms the pointwise wave shape.

Model for the ionic current Several phenomenological and cell models (Section 1.3.1) has been proposed for the I_{ion} term [67, 68, 69, 70, 71, 66, 24, 25, 57, 26, 29]. In this work we use the O'Hara-Rudy model [29]. It is partially[1] human-based, and one of the most complete cell models. The authors used an ODEs fitting technique to create this cell model. The used model includes $\sim$ 50 equations that modulate 41 state variables in which there are included all the critical transmembrane currents like Sodium, Potassium, Chlorum and their different channels and exchangers. This model not only have scientific relevance as it allows to model complex physiological, pathological and pharmacological events [72, 73], but also it has been chosen by the Cardiac Safety Research Consortium [74] (a consortium partially sponsored by the food and drug administration (FDA)) as the gold standard for electrophysiology modelling.

2.3 Solid mechanics

To model solid mechanics we use the finite elasticity framework. The solid mechanics in the heartbeat problem should include the stresses produced by the material model, the boundary conditions, the fluid that is making pressure in the solid walls, and the active tension induced by the myocytes. The way pressure is imposed in the endocardium and the equations for active tension, are treated ahead in this chapter. In the following lines, we describe the passive behavior of the tissue. The solid problem is governed by the linear momentum balance:

$$\rho^s \frac{\partial^2 u_i}{\partial^2 t} = \frac{\partial P_{iJ}}{\partial X_J} + \rho^s B_i, \tag{2.4}$$

where ρ^s is the density of the material. The Cauchy stress $\boldsymbol{\sigma} = J^{-1}\boldsymbol{P}\boldsymbol{F}^T$, is related to the nominal stress P_{iJ} through the deformation gradient $F_{iJ} = \partial x_i / \partial X_J$ and $J = det(\boldsymbol{F})$ is the Jacobian determinant. In cardiac tissue [3], stress is assumed to be a combination of passive and active stress:

$$\boldsymbol{\sigma} = \boldsymbol{\sigma}_{pas} + \boldsymbol{\sigma}_{act}(\lambda, [Ca^{2+}])\boldsymbol{f} \otimes \boldsymbol{f}, \tag{2.5}$$

accounting for the passive ($\boldsymbol{\sigma}_{pas} = \sigma_{ij}^{pas}$) and the contractile ($\boldsymbol{\sigma}_{act} = \sigma_{ij}^{act}$) parts respectively. The active part will be defined in Section 2.5.1.

Model for passive stresses The passive part is modeled as a slightly compressible invariant-type material [39] and through a transverse isotropic exponential strain energy function $W(\boldsymbol{b})$. This constitutive relation describe the response of a material to applied loads, which depends on the internal

[1] To date, there are no action potential models based on experimental data from a single specie.

constitution of the material. The energy function $W(\boldsymbol{b})$ relates to the Cauchy stress $\boldsymbol{\sigma}_{pas}$ to the right Cauchy-Green deformation $\boldsymbol{b}$ and the strain invariants. For the slightly compressible Invariant-type material used in this work [39], the pseudostrain energy function has an exponential stress-strain behavior:

$$J\boldsymbol{\sigma}_{pas} = (a\ e^{b(I_1-3)} - a)\boldsymbol{b} + 2a_f(I_4-1)e^{b_f(I_4-1)^2}\boldsymbol{f}\otimes\boldsymbol{f} + K(J-1)\boldsymbol{I}. \quad (2.6)$$

The strain invariants I_1 and I_4 represent the non-collagenous material and the muscle fibres, respectively. Parameters a, b, a_f, b_f are determined experimentally. K sets the compressibility. Vector $\boldsymbol{f}$ defines the fibre direction, modifying the electrophysiology propagation through Equation (2.2). This near incompressibility is physiologically justified with the high volume fraction of water in most soft tissues that do not diffuse in or out during the period of interest.

2.4 Fluid dynamics

The last building block in the heartbeat problem is the set of equations to model fluid dynamics.

Momentum and continuity in the fluid The blood is modeled as Newtonian and incompressible. This fluid is modeled with the Navier-Stokes equations in deformable domain, this means with an arbitrary Lagrangian-Eulerian (ALE) formulation:

$$\rho^f \frac{\partial v_i}{\partial t} + \rho^f \left(v_j - v_j^d\right)\frac{\partial v_i}{\partial x_j} + \frac{\partial}{\partial x_j}\left[+p\delta_{ij} - \mu\left(\frac{\partial v_i}{\partial x_j} + \frac{\partial v_j}{\partial x_i}\right)\right] = \rho^f f_i \quad (2.7)$$

$$\frac{\partial v_i}{\partial x_i} = 0, \quad (2.8)$$

where μ is the dynamic viscosity of the fluid, ρ^f the density, v_i the velocity, p is the mechanical pressure, f_i the volumetric force term and v_j^d is the domain velocity.

Deformable domain As the fluid domain deforms due to the imposed boundary displacements, the deformation for the inner portion of the domain must also be solved. To do this, we use the technique proposed in [75]. Dirichlet conditions imposed in boundaries of the domain, are diffused thorough the whole domain with a Laplacian equation:

$$\frac{\partial}{\partial x_j}\left(\left[1+\alpha^e\right]\frac{\partial b_i}{\partial x_j}\right) = 0, \quad (2.9)$$

where b_i are the components of the displacement in each point for the domain. In Equation (2.9), the diffusive term α^e controls how the domain deforms with the imposed boundary conditions.

2.5 Coupling the physics

2.5.1 Excitation contraction coupling and mechano-electric feedback

Excitation contraction coupling ECC is the way the electrophysiology model has to induce an active tension in the solid mechanics model. As explained in Section 1.2.2, muscle contraction starts with the depolarization of the cell membrane. This electrical effect triggers Calcium ($[Ca^{+2}]$) release from the sarcoplasmic reticulum in the cell, which ultimately generates the mechanical contraction of the sarcomeres in the myocytes.

As it has been said in Section 2.3, the stress produced in the solid domain has two components. The passive portion σ_{ij}^{pas} is due to the connective tissue and is modeled by the material model, already described in Section 2.3. The active portion σ_{ij}^{act} is produced by contraction of the myocytes and is a function of the Calcium concentration (see Equation (2.5)). Several models are proposed for the ECC, but in this work the Hunter-McCulloch [76] model is used due to its simple Calcium-stress relation. The equation reads:

$$\sigma_{ij}^{act} = \frac{\left[Ca^{+2}\right]^n}{[Ca^{+2}]^n + C_{50}^n} + \sigma_{ij}^{max}(1 + \eta(\lambda - 1)), \tag{2.10}$$

where C_{50} is the Calcium concentration for 50% of σ_{ij}^{max}, n is a coefficient that controls the shape of the curve, and σ_{ij}^{max} is the maximum tensile stress generated at $\lambda = 1$.

Mechano-electric feedback In Section 1.3.2 we described the mechano-electric feedback as the phenomena in which mechanical deformations modulate the electrical activity, by an explicit set of ODE [50, 48, 51]. In this thesis, we do not include such modulation as our focus is on the overall deformation of the heart and not on localized electromechanical phenomena (recall Section 1.5).

Bidirectional electromechanical formulation Despite not using an mechano-electric feedback, we use a bidirectional coupling in the electromechanical model. With this approach, both involved models (electrophysiolgy and solid mechanics) are solved under the same deformable solid domain (see Equation (2.2)). Computing the electrophysiology equations in the deformed mesh do not create new transmembrane currents,

but changes the electrophysiology module solution to accurate solving domain.

2.5.2 Fluid-structure interaction

The last item lacking of physical description is the structure-fluid coupling. FSI is the process where a fluid and and a solid interact through a wet surface, inducing forces and displacements on each other. Lets call Ω_a the fluid domain, and Ω_b the solid domain, interacting in the wet surface Γ_c. In the fluid domain, Navier-Stokes with ALE formulation is solved and, in the other domain, (at least[2]) the solid mechanics model is solved.

Let us label with "nsi" (after Navier-Stokes incompressible) and "sld" the fluid and solid sides of a coupled FSI problem. Then, at the contact or "wet" surface Γ_c, displacements d_i and stresses σ_{ij} must be continuous:

$$ {}^{\text{nsi}}d_i^{\Gamma_c} = {}^{\text{sld}}d_i^{\Gamma_c} \tag{2.11} $$

$$ {}^{\text{nsi}}\sigma_{ij}^{\Gamma_c} n_j = {}^{\text{sld}}\sigma_{ij}^{\Gamma_c} n_j, \tag{2.12} $$

where ${}^{\text{nsi}}d_i^{\Gamma_c}$ and ${}^{\text{sld}}d_i^{\Gamma_c}$ are the deformation in the contact boundary for the fluid and for the solid respectively; and ${}^{\text{sld}}\sigma_{ij}^{\Gamma_c}$ and ${}^{\text{nsi}}\sigma_{ij}^{\Gamma_c}$ and are the stresses in the contact boundary. Both equations represent continuity of displacements and forces respectively. We have to add that during the fluid dynamics modelling (Section 2.4), The stresses ${}^{\text{nsi}}\sigma_{ij}^{\Gamma_c}$ are translated as a volumetric force applied in the contact boundary Γ_c as:

$$ f_i = {}^{\text{nsi}}\sigma_{ij}^{\Gamma_c} \cdot n_j, \tag{2.13} $$

where f_i is the traction in Equation (2.7) and n_j is the normal to the surface.

[2]Afterwards, other models can be added to each side of the problem.

Chapter 3

Computational implementation

"To whom speed means
freedom of the soul"

Vanishing Point (1971)

Summary: The objective of this chapter is to describe the numerical methods to run computational experiments. To do this, the continuum equations for the electrical, mechanical and fluid portions are translated to the discrete spatial and temporal domain, explaining the solution strategies for each model. First, the simulation software, Alya, is described. Then, the geometrical description of the heart, the domain where the equations are solved, is detailed. This description includes the geometry, spatial discretization, fibre and cell distribution. After that, the numerical strategies for each model are detailed, starting with electrophysiology, following with solid mechanics and finishing with fluid dynamics. The FSI problem is solved using a novel HPC coupling strategy, called interface quasi-Newton. The implementation is eased by the computational framework used in this Thesis. Finally, the boundary conditions for the problem are detailed.

3.1 Alya: HPC-based multi-physics and multi-scale simulation code for supercomputers

All developments in this thesis are programmed in Alya, the BSC's in-house simulation software, optimized to run in large-scale computers. This code is versatile enough to easily write new models and solving techniques while hiding a big deal of the parallel implementation burden. Among other features, Alya is capable of running in a multi-code environment that provides flexibility at the time of developing new solving strategies.

3.1.1 Code description

Alya is the Barcelona supercomputing center (BSC) in-house tool used in this work to solve the models and to implement the solving strategies. This software is designed from scratch to run efficiently in high performance computers, with a tested scalability up to 100.000 cores [77, 78, 79, 80, 81].

The code is programmed in a modular way, with a kernel in charge of generic input/output subroutines, solvers, mathematical functions and services like parallelization or other complementary tools. Then, there are several modules, allowing to solve a wide range of coupled problems such as radiation, compressible and incompressible fluids, excitable media and solid mechanics. The software is written in Fortran 90/95. The time dependent partial differential equations (PDEs) are solved using, mainly, finite element method (FEM), but finite volumes can also be used for some problems. The platform is designed to be multiphysics and flexible for coding and running in high performance computing (HPC) machines.

In this thesis a maximum of four physics are used: electrophysiology, solid mechanics, fluid mechanics and the arbitrary Lagrangian-Eulerian (ALE) solver for the deforming meshes. In all the cases FEM is the spatial discretization strategy and, except said otherwise, the code is run in parallel.

3.1.2 Programming framework: divide and conquer

Alya is prepared to run in a multi-code environment. With a built-in library, our simulation tool can be coupled with other modelling software, or with other(s) Alya instance(s). In this work, and for the most general case computed, a multi-code approach is used. Two Alya instances are coupled to solve the fluid-electro-mechanical model, splitting the whole domain in two parts: the fluid sub-problem (blood) and the solid sub-problem (tissue). Each part is solved in one of the instances of the code. Each instance works in a sandbox manner, being completely independent from the other, with their own input configuration and mesh files. Both instances communicates with a black-box approach, knowing only the coupling points and the variables to be transferred.

The fluid-electro-mechanical problem in a multi-code approach The most integrative cases solved in this thesis are the fluid-electro-mechanical cases. As said before, this multiphysics problem can be naturally decomposed in two sub-problems: solid and fluid. Using the multi-code approach available in the simulation tool, we can distribute the involved physics, depending on the sub-problem where they are being solved.

With this approach, the solid domain runs in one Alya instance, computing the electrophysiology (EP) (explained in Section 3.3.1) model and the computational solid mechanics (CSM) (detailed in Section 3.3.2)

equations under the same mesh. The fluid domain runs in another instance of Alya computing the ALE deformable domain (explained in Section 3.4.2) and the computational fluid dynamics (CFD) (detailed in Section 3.4.1) problem, in another mesh. Both codes communicate through a set of integrated *ad-hoc* Message Passing Interface (MPI) subroutines in specific coupling points (see Figure 3.1).

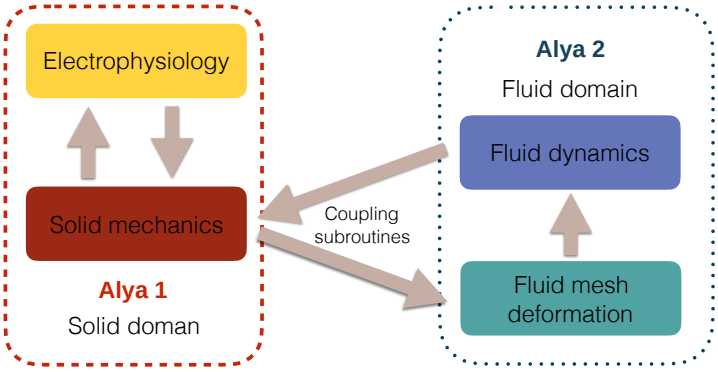

Figure 3.1: Alya Framework. Scheme of the multi-code implementation solving the EP and CSM in one Alya instance and another instance solving the ALE and CFD problems in another mesh.

This coupled multi-physics problem is then solved in a staggered way. Each Alya instance solves two problems: on one side, electrophysiology and tissue mechanics; and on the other side, fluid mechanics and mesh deformation. In turn and for each iteration, each of the four physical problems is solved independently. This strategy has its benefits and drawbacks. Among the benefits is its flexibility, because each physical problem can be programmed independently of the other, with smaller problem matrices and its own best-suited solution strategy, allowing to solve the problems in a standalone way if required or adding more and more problems to solve. The drawback is that the coupling strategy must be robust and efficient enough to take real profit of the advantages. The efficiency issue is important not only from the algorithmic viewpoint but also from the parallel implementation one, especially when the two instances are coupled. In this work we show at what extent these drawbacks are overcame.

Domain partition and communication points Both of the multi-code approach sub-problems (*e.g.* Ω_a and Ω_b) are potentially very large, requiring in turn parallel runs. Each sub-problem is then partitioned using a mesh partitioner such as METIS [82] and distributed to many MPI parallel threads, every thread with its corresponding sub-domain: Ω_a^1, Ω_a^2, Ω_a^3, $(\cdots)$ and Ω_b^1, Ω_b^2, Ω_b^3, $(\cdots)$. If both sub-problems are parallelized, then an efficient MPI point-to-point communication scheme is required for the wet surface Γ_c,

as can be seen in Figure 3.2.

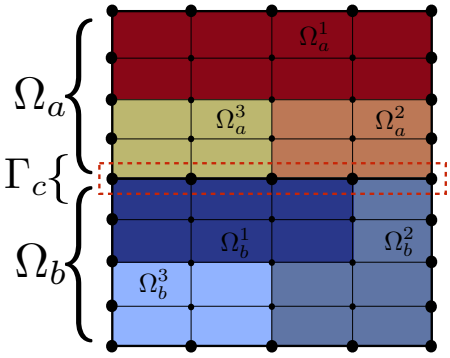

Figure 3.2: Physical sub-problems Ω_a and Ω_b in contact by the wet surface Γ_c. Each physical sub-problem is subdivided in three computational sub-domains. To be parallelly efficient, communications for the contact surface Γ_c between the sub-problems must be carefully designed.

3.1.3 Modelling pipeline

The pipeline used to obtain the simulations results is shown in Figure 3.3.

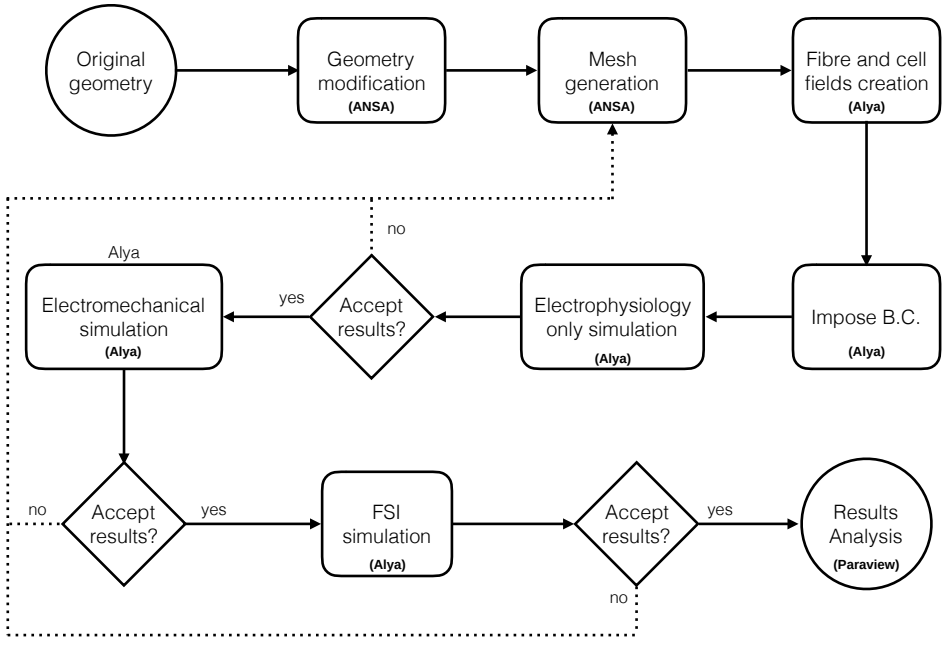

Figure 3.3: Modelling pipeline to for pre-processing, simulation and post-processing.

As a first step, the original geometry is modified, and the mesh is created with a pre-processor software (explained in Section 3.2). Then, the fibre and cell distribution are computed through a rule-based method (described in Section 3.2.2), and the boundary conditions (B.C.) are imposed for each physic. After, each one of the problems is incrementally added to the model, starting with EP (Section 3.3.1), following with CSM (Section 3.3.2) and finishing with the coupled Fluid-Structure Interaction (FSI) (Section 3.5) problem that includes the CFD (Section 3.4.1) formulation. Once each physic is added, the simulations results are analysed to look for convergence problems and physical consistency with the originally defined problem. The most common encountered issue was after including the FSI formulation. Often, the intracavitary space contracts in such a manner that the elements of the fluid domain get extremely flatten and the CFD problem diverge or the elements are inverted. In that case, the mesh should be rebuilt taking special care in that conflictive region.

3.2 Computational description of the heart

In this section we describe the domain where the computational models are solved. As said in Section 1.2, the heart not only has a complex geometry, but also a complex histology. Due to this fact, many critical information intrinsic to the geometry as fibre and cell distribution (Section 3.2.2) is required.

Two geometries are presented. Firstly, we show a full heart geometry, that is the most complete geometrical description in the work. Then, we present a ventricles-only geometry, used to run simpler experiments.

3.2.1 Geometry and spatial discretization

Geometry generation The whole heart geometry used in this thesis comes from the Zygote Solid 3D heart model [83] shown in Figure 3.4. This geometry represents the 50th percentile U.S. 21-year-old healthy Caucasian male (average error under 5 %). Images were reconstructed from 0.75 $[mm]$ thick Magnetic Resonance Imaging (MRI) slices [83].

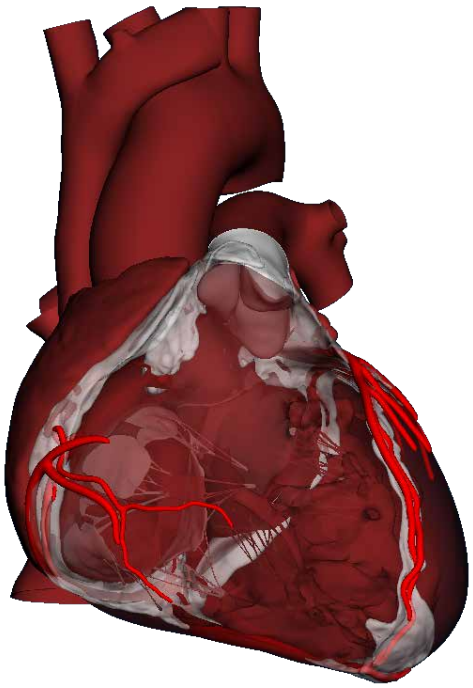

Figure 3.4: Computational description of the heart. Complete geometry of the original Zygote human heart model [83].

Even though the acquisition and reconstruction were performed during 70% diastole, the geometry is subjected to residual stresses. The geometry could be pre-stressed using a fictitious configuration technique [84, 85], but due to the known condition of end-diastolic configuration, we assume that the geometry is stress-free.

Modifying the geometry To modify the geometry and create the mesh, the proprietary software ANSA pre-processor [1] was used. This is a very handcrafted job that took several trial and error iterations until the mesh was good enough for modelling. The main modifications of the Zygote geometry were:

- The non-specific structures were removed (*i.e.* fat and vessels).
- The valvular leaflets were removed, closing the space with a plane surface in the atrioventricular case.
- The geometry surfaces were modified to make them fit between each other.

[1] visit `https://www.beta-cae.com/ansa.htm` for more information.

- The atria was filled with an isotropic lineal solid material, with a density of $\rho = 1.04\,[g/cm^3]$, a young modulus of $E = 5\,[Ba]$ and a Poisson ratio of $\nu = 0.0005$. This allows a physiological dynamic of the structure without modelling the atrial inner fluid dynamics.
- The inner surface of the endocardium were smoothed to reduce possible mesh inverting problems in the fluid mesh.
- The inner cavities volumes were created.

In Figure 3.5 the modified geometry next to the ventricular fibres can be seen.

Figure 3.5: Computational description of the heart. Left: mesh of the modified version. Center: slice of the geometry showing the filled atrium and the ventricular cavities. Right: Fibre description of the ventricles, top and frontal view.

Spatial discretization As seen from literature of cardiac electro-mechanical coupling (at least for the relatively few cases reported), the most common approach so far has been to use [86, 87, 54, 88] different meshes to simulate electrophysiology and solid mechanics, even though they are virtually the same domain. This approach is generally motivated by two reasons. On one hand, is generally observed that while the electrophysiology problem is eventually well parallelized, solid mechanics is not. On the other hand, it is generally stressed that electrophysiology needs a finer mesh definition that solid mechanics. It is worth to remark that the use of different mesh sizes do not represent a problem per se (it is well known that solving in different mesh sizes and interpolating fields can arise stability problems). However, Alya is highly efficient to solve in parallel all of its programmed

models. Therefore, we use the same mesh for the electrical and the solid mechanical problems. For this work, an average element size of 250 $[\mu m]$ is used. Figure 3.6 shows histograms for the element volume distribution for the solid mesh and the fluid mesh.

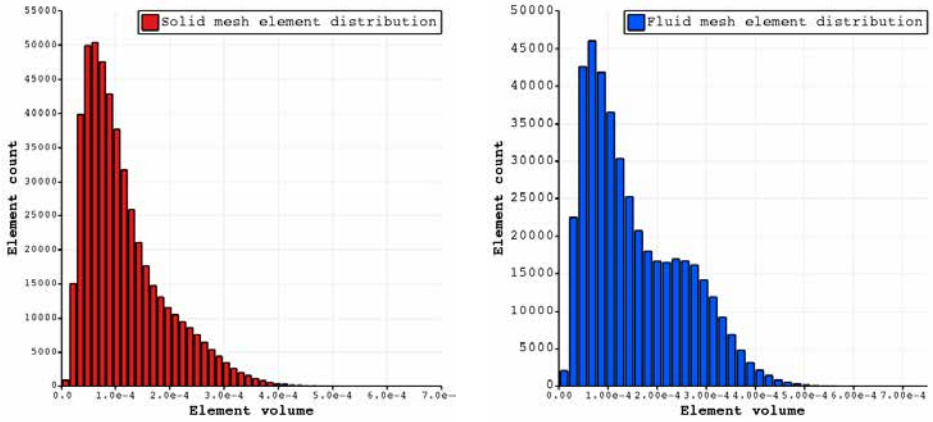

Figure 3.6: Element volume distribution for the solid and the fluid mesh.

The meshing strategy fits, whenever possible, larger elements in the non-conductive volumes (atria and vessels), obtaining a non-uniform element volume across de mesh. This allows to have an appropriate spatial discretization in the regions required, while maintaining the element overall element count as small as possible. For the fluid domain mesh this constrain is not required, so bigger elements are allowed. Despite this, as both meshes are enforced to have matching nodes in the contact boundary, the fluid domain mesh results almost as fine as the solid mesh.

3.2.2 Fibre and cell distribution

As discussed in Section 1.2.1, fibre and cell distribution are critical for the electrical depolarization and mechanical deformation of the myocardium. The fiber distribution can be experimentally recovered from animal or *ex-vivo* organs with diffusion tensor imaging magnetic resonance (DTI) [18, 89], allowing to have fibre distribution from biological tissues. This technique measures water molecules diffusion to reveal microscopic detail about fibre architecture. However, as the water molecules diffuse in all directions, DTI does not provide a good spatial resolution and results in very noisy data. On the other hand, fibre distribution can be generated with rule-based methods [90, 91, 92, 7, 93]. These techniques find the relative position for each node in the domain with respect to the endocardium and the epicardium and assigns a fibre direction and cell tag.

Streeter fiber model In this work we create the fibres with the algorithm developed in [94, 7], which we briefly describe here. For each node in the ventricles, the minimal distance to endocardium and epicardium is computed (d_{endo}, d_{epi}). After this, a thickness parameter e is defined:

$$e = \frac{d_{endo}}{d_{endo} + d_{epi}}. \tag{3.1}$$

The fibres are build orthogonal to the local base generated, ensuring a smooth angle variation. Fibre orientation is then determined by:

$$\alpha = \frac{\pi}{3}(1 - 2e)^n, \tag{3.2}$$

where n determines a linear ($n = 1$) or cubic ($n = 3$) variation (see Figure 3.7 for a comparison of both functions). $\pi/3$ is the maximum and minimum angles for the fibres $(-60°, 60°)$. Through Equation (3.1) cell differentiation is also assigned, being the first $1/3$ endocardial cells, the second $1/3$ mid-myocardial cells and the last $1/3$ epicardial cells, with slightly different electrophysiology parameters. For a graphical reference of the fibre an cell distribution see Figure 3.7.

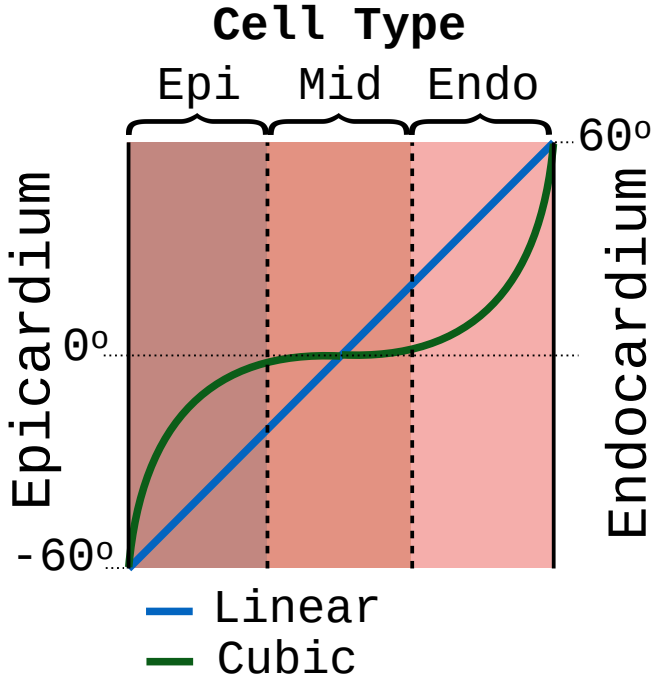

Figure 3.7: Fibre an cell distribution form endocardium to epicardium.

In this thesis the fibre distribution in the left ventricle (LV) and in the right ventricle (RV) are similarly treated with the Streeter algorithm. This is

a simplification, as the RV fibre distribution can be separately characterized [95]. Such a feature could be included implementing an algorithm as the described in [90, 93].

Atria fibre model As explained in the last pages, in the whole-heart model proposed in this thesis, atria do not depolarize or contract. Despite it is true that the passive mechanical properties of the tissue are also aligned with the fibre distribution, the main source of internal stresses come from the active contraction (explained ahead). Due to this, the fibre distribution in the atria is extrapolated from the ventricles, following the helicoidal shape, given by the outer and inner walls and the Streeter rule-based method described above. This is a simplification that must be tackled when the whole heart model includes contractile atria, as the fibre field in these structures follow a complex distribution [13, 96]. But, under the hypothesis we use, a simplified fibre distribution should not have a great impact as the passive deformation of both atrium are small compared against the active deformation of the ventricles.

3.2.3 Bi-ventricular version

We also propose a ventricle-only version of the Zygote human heart geometry. For this, we apply the same process as the described in Sections 3.2.1 and 3.2.2 but only to the surfaces related to the ventricles. The geometry and mesh are shown in Figure 3.8. A slice and other views of the same geometry are shown in Figure 4.6. The bi-ventricular geometry is very similar to those simplified geometries when the electrophysiology problem is solved alone. We will use it here to show some features of the coupled problem when running on such kind of scenarios.

Figure 3.8: Computational description of the heart. Biventricular geometry overview.

Spatial discretization The mesh has 500k elements and 80k nodes. Although the element size and shape is not constant, mesh quality is

evaluated using the scaled Jacobian (SJ), which is kept within the range 0.3-1.0, with only 3000 elements below 0.5.

3.3 Computational implementation: The structure domain

Here we describe the problems solved in the solid sub-problem, which are the electrical wave propagation and the deformation of this domain due to the electrical activity. As said above, both sets of equations are solved in the same computational mesh and computed by one Alya instance, *i.e.* the left side of Figure 3.1.

3.3.1 Electrical wave: electrophysiology modelling

The electrical propagation is ruled by Equation (2.1) described in Section 2.2. The continuum equations are discretized in time and space using finite differences and finite element, respectively.

Discretized form The linear diffusive terms can be integrated by parts using either open or closed rules. Closed integration is used in the ionic current term $I_{ion}(\boldsymbol{\phi})$ to preserve the nodal character. This strategy used for the non-linear part produces a trivially invertible diagonal mass matrix. Once discretized, Equation (2.1) becomes:

$$\left(\frac{\mathbf{M}}{\Delta t}+\theta\mathbf{K}\right)\Delta\boldsymbol{\phi}+\mathbf{M}^{d}\mathbf{I}_{ion}=-\mathbf{K}\boldsymbol{\phi}^{n} \tag{3.3}$$

where $\Delta\boldsymbol{\phi}=\boldsymbol{\phi}^{n+1}-\boldsymbol{\phi}^{n}$ is the unknown difference between two time steps. θ determines if the time integration scheme is Forward Euler (first order explicit, $\theta=0$), Backward Euler (first order implicit, $\theta=1$) or Crank-Nicolson (second order implicit, $\theta=0.5$) respectively.

Solving strategy The discrete equations in Equation (3.3) are solved using a first order Yanenko operator splitting:

$$\begin{aligned}
\text{Cell model}(\Delta\boldsymbol{\phi}^{*}):&\quad \frac{\Delta\boldsymbol{\phi}^{*}}{\Delta t}+\mathbf{I}_{ion}(\boldsymbol{\phi})=0\\
\text{Tissue model}(\Delta\tilde{\boldsymbol{\phi}}):&\quad \left(\frac{\mathbf{M}}{\Delta t}+\mathbf{K}\right)\Delta\tilde{\boldsymbol{\phi}}=-\mathbf{K}\boldsymbol{\phi}^{*},\quad \text{where}\quad \Delta\boldsymbol{\phi}^{*}=\boldsymbol{\phi}^{*}-\boldsymbol{\phi}^{n}\\
\text{Update}(\boldsymbol{\phi}^{n+1}):&\quad \boldsymbol{\phi}^{n+1}=\boldsymbol{\phi}^{n}+\Delta\boldsymbol{\phi}^{*}+\Delta\tilde{\boldsymbol{\phi}}.
\end{aligned}$$

where the Cell Model is explicitly solved using a Forward Euler scheme and the Tissue Model is solved implicitly with either a Backward Euler or a Crank-Nicolson scheme. From numerical experiments we observed that as

the main critical time limitation comes from the Tissue Model, the proposed scheme is both efficient and accurate enough.

3.3.2 Myocardium mechanical deformation: CSM

Equations in Section 2.3, which governs the mechanical solid dynamics in the heart tissue, are spatially discretized with finite elements and temporally discretized with finite differences.

Discretized form Discretizing Equation (2.4) leads to a matrix equation of the form:

$$\rho^s \mathbf{M} \frac{\Delta \boldsymbol{u}}{\Delta t^2} + \mathbf{K}(\boldsymbol{u})\boldsymbol{u}^{n+1} = \mathbf{R} \tag{3.4}$$

where $\boldsymbol{u}$ is the unknown displacement, $\mathbf{R}$ is the force term, $\mathbf{M}$ is the mass matrix, and $\mathbf{K}(\mathbf{u})$ is the stiffness matrix.

Solving strategy The resulting system is solved using a Newmark scheme,

$$\begin{aligned}
&\mathbf{u}^* = \mathbf{u}^n + \Delta t v^n + \Delta t^2 (\frac{1}{2} - \beta)\mathbf{a}^n \\
&\frac{\rho^s \mathbf{M}}{\Delta t^2 \beta} \left(\mathbf{u}^{n+1} - \mathbf{u}^*\right) + \mathbf{K}\mathbf{u}^{n+1} = -\mathbf{f}_{\text{ext}} \\
&\mathbf{a}^{n+1} = \frac{1}{\Delta t^2 \beta} \left(\mathbf{u}^{n+1} - \mathbf{u}^*\right) \\
&\mathbf{v}^{n+1} = \mathbf{v}^n + \Delta t(1-\gamma)\Delta t \gamma \mathbf{a}^{n+1}.
\end{aligned} \tag{3.5}$$

In this work we solve the second system in an explicit way, where parameters β and γ are chosen for good stability properties (see [80]).

Dynamic problem treatment and spurious oscillation control In this work, we solve all problems dynamically. Therefore, either a physical (adding viscoelastic terms to the material model) or numerical strategy (adding artificial dissipation to the equations) is required, because hyperelastic-type materials can present spurious oscillations if no additional dissipation is considered. In this work we prefer the second one, where dissipation can be added as a Rayleigh damping term, which leads to modify Equation (3.4):

$$\boldsymbol{\rho}\mathbf{M} \frac{\Delta \boldsymbol{u}}{\Delta t^2} + \mathbf{C}(\boldsymbol{u}) \frac{\Delta \boldsymbol{u}}{\Delta t} + \mathbf{K}(\boldsymbol{u})\boldsymbol{u}^* = \mathbf{R} \tag{3.6}$$

where $\mathbf{C}(\boldsymbol{u}) = \alpha \mathbf{M} + \beta \mathbf{K}(\boldsymbol{u})$. Parameters α and β are computed depending on the frequency range to be damped. In [97] we propose to use $\beta = 0$ and $\alpha = c\omega$ with $c = 5$. The frequency target ω is obtained after a frequency spectrum analysis on a large number of simulations on smaller pieces of tissue with the same material model and no Rayleigh damping.

3.4 Computational implementation: The fluid domain

The main problem to be solved in the fluid mesh is the incompressible Navier-Stokes equation. But also, the way in which the fluid mesh deform, should be computed. Both problems belong to the same physical domain, the fluid sub-problem. In this way, they are solved in the same computational mesh, in the second Alya instance.

3.4.1 Intraventricular blood flow: CFD

As said in Section 2.4 the physics describing the fluid inside the ventricles are governed by the incompressible Navier Stokes equation (Equation (2.7)).

Discrete compact form for the Navier-Stokes equation For the sake of simplicity, let us rewrite the equations in a more compact form. First, lets define $\mathbf{v} := v_i$ and let ε and σ be the velocity rate of deformation and the stress tensors respectively, defined as:

$$\varepsilon(\mathbf{v}) = \frac{1}{2}\left(\nabla\mathbf{v} + \nabla\mathbf{v}^T\right) = \left(\frac{\partial v_i}{\partial x_j} + \frac{\partial v_j}{\partial x_i}\right) \tag{3.7}$$

$$\sigma = -p\mathbf{I} + 2\mu\varepsilon(\mathbf{v}). \tag{3.8}$$

With this, we can define vector with the unknowns $\mathbf{U} = [\mathbf{v}, p]^T$, a differential operator $\mathcal{L}(\mathbf{U})$ and a force term $\mathbf{F}$ as:

$$\mathcal{L}(\mathbf{U}) = \begin{bmatrix} \rho^f \left[\left(\mathbf{v} - \mathbf{v}^d\right)\cdot\nabla\right]\mathbf{v} - \nabla\cdot\left[2\mu\varepsilon(\mathbf{v})\right] + \nabla p \\ \nabla\cdot\mathbf{v} \end{bmatrix} \tag{3.9}$$

$$\mathbf{F} = \begin{bmatrix} \rho^f\mathbf{f} \\ 0 \end{bmatrix}, \tag{3.10}$$

$$\tag{3.11}$$

where the domain velocity $\mathbf{v}^d$ becomes the mesh velocity $\mathbf{v}^m$ once the equation is discretized. If the matrix $\mathbf{M} = \text{diag}\left(\rho^f\mathbf{I}, 0\right)$, where $\mathbf{I}$ is the identity tensor, we can write the incompresible Navier-Stokes in the compact form:

$$\mathbf{M}\partial_t\mathbf{U} + \mathcal{L}(\mathbf{U}) = \mathbf{F}. \tag{3.12}$$

The numerical model is based on FEM, using the variational multiscale (VMS) method [98] to stabilize convection and pressure. The formulation is obtained by splitting the unknowns into grid scale and a subgrid scale

components, $\mathbf{U} = \mathbf{U}_h + \tilde{\mathbf{U}}$. This subgrid scale $\tilde{\mathbf{U}}$ is also modeled. Lets define $\mathcal{R}\left(\tilde{\mathbf{U}}\right)$ the Navier-Stokes residue as:

$$\mathcal{R}\left(\tilde{\mathbf{U}}\right) = \mathbf{F} - \mathbf{M}\partial_t \mathbf{U} - \mathcal{L}\left(\mathbf{U}\right). \tag{3.13}$$

Then, the expression:

$$\tilde{\mathbf{U}} = \tau \mathcal{R}\left(\tilde{\mathbf{U}}\right), \tag{3.14}$$

is considered for the stabilization where τ is a diagonal matrix, depending on the convection velocity.

Solving strategy The resulting system is solved through a velocity-pressure splitting strategy, already implemented in the Alya simulation code. Time discretization is based on second order backwards differences, and linearization is carried out using Picard method. At each time step, the system:

$$\begin{bmatrix} \mathbf{A}_{uu}\mathbf{A}_{up} \\ \mathbf{A}_{pu}\mathbf{A}_{pp} \end{bmatrix} \begin{bmatrix} \mathbf{u} \\ \mathbf{p} \end{bmatrix} = \begin{bmatrix} \mathbf{b}_u \\ \mathbf{b}_p \end{bmatrix}, \tag{3.15}$$

must be solved for velocity ($\mathbf{u}$) and pressure ($\mathbf{p}$) vectors. In order to solve this system efficiently in supercomputers, a split approach is used [77]. The Schur complement is obtained and solved with an Orthomin(1) algorithm [99]. To do so, the momentum equation is solved twice using GMRES (Generalized Minimal Residual Method) and the continuity equation is solved with the Deflated Conjugate Gradient algorithm.

3.4.2 Deformable fluid domain: the ALE problem

The Laplacian equation that rules the fluid domain deformation is proposed in [75]. Once the volume is discretized, the position of each node (b_i) in the mesh is computed as:

$$\frac{\partial}{\partial x_j}\left(\left[1+\alpha^e\right]\frac{\partial b_i}{\partial x_j}\right) = 0. \tag{3.16}$$

The factor α^e controls de mesh distortion depending on the volume of each element:

$$\alpha^e = \frac{1 - V_{min}/V_{max}}{V_e/V_{max}}. \tag{3.17}$$

In this way, while small elements remain almost undeformed, large elements suffer the larger deformations. In the last expression V_{max} and V_e are the maximum and current element size in the grid. This equation spatially discretized using the FEM and solved with a Deflated Conjugate Gradient algorithm [100].

3.5 Fluid-structure interaction

In this section we discuss the FSI coupling. As it is a key part of the algorithm, we will do it in a deeper way following what is presented in [101]. We need to compute the solution for the contact boundary (also called wet surface) Γ_c (see Figure 3.2). In this surface, the solid domain deforms the boundary and the fluid imposes forces due to the inertia, the pressure and the viscous stresses of the blood. In this part of the problem is where the multi-code approach described in Section 3.1.2 eases the implementation. Having two Alya instances solving the domain-specific problems, allows to easily implement the FSI relaxation strategies. For the sake of simplicity, as FSI problem is independent of the electrophysiology model, the electrical wave propagation will be avoided in this section. Despite this, all said in the next pages stands if the electrophysiology model is included.

3.5.1 Computational framework for the FSI problem

Strategies to solve the FSI problem The main two families of methods to solve FSI problem are the following: the ALE and the immersed boundary (IB) methods [102]. The former deforms the fluid mesh following the solid wet boundary, and the latter tracks the wet surface in an Eulerian fluid mesh to enforce velocities in the fluid. The ALE method may require remeshing, but has a more precise solution. The IB method mesh requirements are more lenient, but the continuity equation (Equation (2.8)) may have convergence problems due to the spatial interpolation. Also, due to the same reason, the IB method lacks numerical precision. Alya (Section 3.1.2), already have efficient CSM and CFD solvers. In this way, reusing this codes to solve the FSI problem with the partitioned ALE method, is a natural way to proceed in our work.

Dirichlet-Neumann decomposition of the problem The classical technique to solve the FSI problem with a partitioned ALE method is to use a Dirichlet-Neumann (D-N) splitting approach [103]. When using this technique, one of the sides computes the Dirichlet part (displacement, d_α) and the other computes the Neumann one (force, f_α). Generally, the solid side computes the Dirichlet problem (*i.e.* $d_\alpha = \mathrm{S}(f_\alpha)$), and the fluid side computes the Neumann problem (*i.e.* $f_\alpha = \mathrm{F}(d_\alpha)$). With this, we can write the fixed point equation as:

$$f_\alpha^{I+1} = \mathrm{F}(\mathrm{S}(f_\alpha)), \tag{3.18}$$

where I is the coupling iteration. Computing Equation (3.18) solves both problems for each time step.

Algorithms to solve the D-N splitting The fixed point equation can be solved through either Gauss-Seidel or Jacobi schemes. In the former, the solvers runs one after the other, improving convergence but penalizing performance. In the later both solvers runs at the same time, improving performance but penalizing convergence [104].

In this work, we use the Gauss-Seidel scheme to ease convegence. Both algorithms are shown in Algorithm 1. The term φ_{GS} and φ_J in Algorithm 1 is what relaxes the solution before a new iteration.

while *Time loop* **do**
  $d_\alpha = d_\alpha^{ini}$
  while *Coupling loop* **do**
    $f_\alpha^I = \mathrm{F}(\mathrm{S}(\tilde{f}_\alpha))$
    $\tilde{f}_\alpha^{I+1} = \varphi_{GS}(f_\alpha^I)$
  end
end

while *Time loop* **do**
  $d_\alpha = d_\alpha^{ini}$
  while *Coupling loop* **do**
    $d_\alpha = \mathrm{S}(\tilde{f}_\alpha)\ ;\ f_\alpha = \mathrm{F}(\tilde{d}_\alpha)$
    $< \tilde{d}_\alpha^{I+1}, \tilde{f}_\alpha^{I+1} >= \varphi_J(d_\alpha, f_\alpha)$
  end
end

Algorithm 1: Gauss-Seidel (left) and Jacobi (right) schemes. φ_{GS} and φ_J are the convergence acceleration algorithm for each case. $\tilde{d}_\alpha$ and $\tilde{f}_\alpha$ represent the relaxed variables. Note that in the Gauss-Seidel approach the problems are solved in a block-sequential way, and in the Jacobi approach in a block-parallel way.

Left side of Algorithm 1 shows the Gauss-Seidel scheme. In it, for each coupling iteration, the Alya instances run one after the other in a block serial manner. Due to this, one of the solvers is idle while the other is computing. When both problems (*i.e.* $\mathrm{S}(f_\alpha)$ and $\mathrm{F}(d_\alpha)$) are solved, the convergence acceleration algorithm (φ_{GS}) executes and a new coupling iteration starts. This temporal scheme can be visualized in the schematic trace in Figure 3.9.

On the contrary, in the Jacobi scheme (right side of Algorithm 1), the fluid and solid solvers run at the same time. In this way, no solver has to wait for the results of the other. Similarly as the Gauss-Seidel scheme, after both problems are solved, the convergence acceleration algorithm φ_J executes before starting a new iteration.

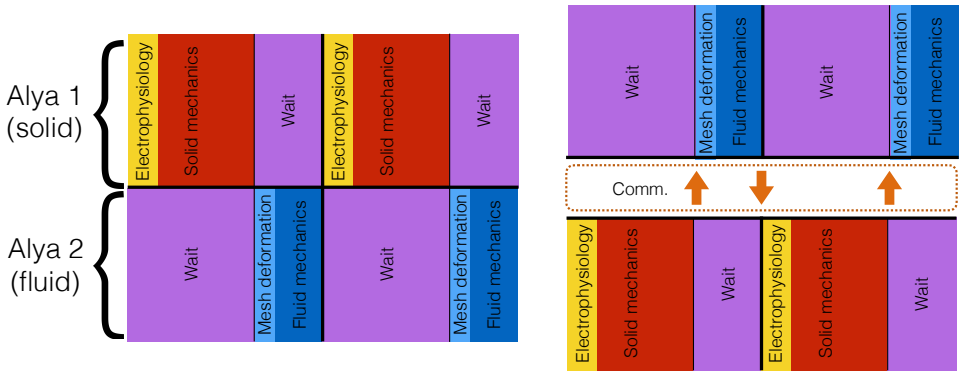

Figure 3.9: Implementation framework. Schematic trace for the Gauss-Seidel approach The parallel solvers are executed in a block manner. The right side remarks the MPI communication points in the used scheme.

3.5.2 Added mass instability

Added mass instability, is a numerical problem that appears with similar fluid and solid densities, and incompressible formulations [105, 106, 107]. This instability aggravates when:

- Time step decreases
- Viscosity of the fluid increase
- Rigidity of the solid decreases
- Temporal discretization order increases

In this work we focus our interest in biomechanics applications, specially heart modelling. As tissue and blood have very similar densities, the added mass effect can affect convergence of the solution procedure in partitioned schemes. In order to deal with this instability, non-trivial relaxation schemes were developed.

These type of algorithms can be classified in two categories: scalar and vectorial. In the former, like the popular Aitken algorithm [108], one relaxation parameter is found for all the contact surface. In the latter, like the Broyden scheme [109], one relaxation parameter is computed for each node in the boundary. This second group of algorithms work better when different type of dynamics rule the coupling surface, as the relaxation parameter is computed pointwise. Such is the case of the heartbeat, where there are two virtually disjoint surfaces (right and left ventricles). In the following pages we explain the interface quasi-Newton (IQN) scheme[110]. After that, we propose a high performance implementation, the Compact interface quasi-Newton (CIQN) algorithm.

3.5.3 High performance interface quasi-Newton algorithm

In this section we firstly give a general description of the algorithm (Section 3.5.3.1). Next, we propose several improvements to obtain the CIQN iterative coupling scheme (Section 3.5.3.2), especially designed for large-scale problems (Section 3.5.3.3).

A note on index notation convention In order to better describe the implementation, the Einstein notation [111] will be followed. This notation is particularly helpful on computational grounds, because it simultaneously describes the mathematics, the physics and the computational implementation aspects. Depending on the context, whether the problem is continuum or discretized, we use different labeling sets. For the continuum problem, the convention on repeated indices is the usual one, with indices labeling space dimensions. On the other hand, once the continuum problem is discretized and we obtain a system matrix, we identify different labeling sets. The lowercase Greek alphabet $\alpha = 1, \cdots p$ labels the total number of degrees of freedom p, *i.e.* the matrix rows. The lowercase Latin alphabet labels the matrix columns, $i = 1, \cdots q-1$ where q is the last stored iteration. In the CIQN scheme matrices are not square, with $p \gg q$. Additionally, a capital latin subindex labels the IQN iteration $I = 1, \cdots q-1$, where q is again the last stored iteration and, to simplify notation, the current iteration is not explicitly indexed. A final rule is how those indices operate: only those of the same kind contract. For instance, $Q^{I-1}_{\alpha i}$ is the Q matrix for iteration $I-1$ with rows labeled α and columns i. When this matrix is multiplied by a certain vector B_i, it results in a given vector A^{I-1}_{α}:

$$A^{I-1}_{\alpha} = Q^{I-1}_{\alpha i} B_i = \sum_{i}^{q} Q^{I-1}_{\alpha i} B_i,$$

where Latin indices i contract.

3.5.3.1 General overview of the IQN algorithm

The first implementation of the IQN algorithm is described in [110], which can be considered an improvement of the Aitken algorithm. Whereas the Aitken algorithm can be understood as a quasi-Newton scheme where the Jacobian is enforced to be a scalar, in the IQN the Jacobian is approximated by a field defined in the contact surface and depending on the local residual variation over a given number of iterations [112].

Let us restate Equation (3.18) as $\widetilde{x}_\alpha = H(x_\alpha)$. If the residual at each iteration is:

$$r_\alpha = H(x_\alpha) - x_\alpha = \widetilde{x}_\alpha - x_\alpha, \tag{3.19}$$

the problem is converged when $r_\alpha = 0$. To solve this problem using Newton-Raphson iterations, the derivative with respect to the variable must be computed:

$$\frac{\partial r_\alpha}{\partial x_\beta}\Delta x_\beta = -r_\alpha. \tag{3.20}$$

Solving this system, Δx_β is obtained and the next iteration unknown is computed as:

$$x_\alpha^{I+1} = x_\alpha + \Delta x_\alpha. \tag{3.21}$$

Generally $\partial r_\alpha / \partial x_\beta$ cannot be computed or it is computationally expensive to do so. But, the inverse Jacobian fulfills the secant equation:

$$\left(\frac{\partial r_\alpha}{\partial x_\beta}\right)^{-1} V_{\alpha i} \approx W_{\beta i}, \tag{3.22}$$

where:

$$V_{\alpha i} = \left[\Delta r_\alpha^{I-1}, \Delta r_\alpha^{I-2}, ..., \Delta r_\alpha^{0}\right] \tag{3.23}$$

$$W_{\alpha i} = \left[\Delta \widetilde{x}_\alpha^{I-1}, \Delta \widetilde{x}_\alpha^{I-2}, ..., \Delta \widetilde{x}_\alpha^{0}\right]. \tag{3.24}$$

At each iteration I, the columns of the increment matrices are built as follows:

$$\Delta r_\alpha^{I-1} = r_\alpha^{I-1} - r_\alpha \qquad \text{for matrix } V_{\alpha i} \tag{3.25}$$

$$\Delta \widetilde{x}_\alpha^{I-1} = \widetilde{x}_\alpha^{I-1} - \widetilde{x}_\alpha \qquad \text{for matrix } W_{\alpha i} \tag{3.26}$$

where r_α and $\widetilde{x}_\alpha$ are the values in the actual iteration and r_α^{I-1} and $\widetilde{x}_\alpha^{I-1}$ are the values in the saved past iterations ($I = 1, \cdots q-1$). The residual increment of the current iteration is approximated as a linear combination of the previous residuals increments:

$$\Delta r_\alpha = V_{\alpha i}\lambda_i, \tag{3.27}$$

where $\lambda_i \in \mathbb{R}^{q\times 1}$ is the solution of the optimization problem $\parallel \Delta r_\alpha - V_{\alpha i}\lambda_i \parallel$ described in [113]. It is worth to remark that matrices Equations (3.23) and (3.24) are far from being square, because while the number of rows corresponds to the total number of degrees of freedom, the number of columns is the stored number of Newton-Raphson iterations done.

Firstly, the matrix $V_{\alpha i}$ is decomposed by a QR decomposition, where an orthogonal matrix $Q_{\alpha\beta} \in \mathbb{R}^{p\times p}$ and an upper triangular $U_{\alpha i} \in \mathbb{R}^{p\times q}$ are obtained:

$$V_{\alpha i} = Q_{\alpha\beta}U_{\beta i}. \tag{3.28}$$

As $U_{\alpha i}$ is upper triangular, only the first q rows are different from zero, which means that only the first q columns of the matrix Q are relevant to

solve the system. Then, a modified QR decomposition can be built with $U_{ij} \in \mathbb{R}^{q \times q}$ and $Q_{\alpha i} \in \mathbb{R}^{p \times q}$ such that:

$$V_{\alpha i} = Q_{\alpha k} U_{k i}, \tag{3.29}$$

highly reducing the amount of memory and computing effort required, as described below in Sections 3.5.3.2 and 3.5.3.3. After this decomposition, the vector λ_i can be built by backsubstitution of the upper triangular matrix U_{ij}:

$$U_{ij} \lambda_j = Q_{\alpha i} \Delta r_\alpha. \tag{3.30}$$

As $Q_{\alpha i}$ is orthogonal, the inverse is equal to the transpose, avoiding the inversion of this matrix. Also, as $\Delta r_\alpha = r_\alpha^{I-1} - r_\alpha$ and the objective is to get $\Delta r_\alpha = 0_\alpha - r_\alpha$, we can say:

$$U_{ij} \lambda_j = -Q_{\alpha i} r_\alpha. \tag{3.31}$$

Once λ_i is computed, the increment of the unknown Δx_α can be computed as $\Delta x_\alpha = W_{\alpha i} \lambda_i$, and the update of the unknown as:

$$x_\alpha^{I+1} = \widetilde{x}_\alpha + W_{\alpha i} \lambda_i. \tag{3.32}$$

The simplest description of the IQN coupling technique is summarized in Algorithm 2. In the first step, an initial guess for both fluid and solid solvers are computed together with the first residual r_α^0. In the first coupling iteration, a fixed relaxation ω_0 is used. After the first iteration, the loop continues until convergence is achieved. Once computed the second iteration, the increment matrices $V_{\alpha i}$ and $W_{\alpha i}$ can be built. Each matrix has p rows (the total number of contact degrees of freedom (d.o.f.)), and q columns (the number of past increments saved). Generally (see Section 3.5.3.2) p is much larger than q. It is worth to remark that q is set as the number of stored iterations, being usually lower than the performed iterations, i.e. only the q newer past increments are used, discarding the older ones. To develop an efficient yet accurate implementation of the IQN algorithm, we should focus in the QR decomposition, which involves complex matrix operations.

For each time step, solve:
$x_\alpha^0 = x_\alpha^{ini}$
$\widetilde{x}_\alpha^0 = H(x_\alpha^0)$
$r_\alpha^0 = \widetilde{x}_\alpha^0 - x_\alpha^0$
update $x_\alpha^1 = \widetilde{x}_\alpha^1 + \omega_0 r_\alpha^0$
while *problem not converged* **do**
  $\widetilde{x}_\alpha = H(x_\alpha)$
  $r_\alpha = \widetilde{x}_\alpha - x_\alpha$
  build $V_{\alpha i} = \left[\Delta r_\alpha^{I-1}, ..., \Delta r_\alpha^0\right]$; with $\Delta r_\alpha^I = r_\alpha^I - r_\alpha$
  build $W_{\alpha i} = \left[\Delta \widetilde{x}_\alpha^{I-1}, ..., \Delta \widetilde{x}_\alpha^0\right]$; with $\Delta \widetilde{x}_\alpha^I = \widetilde{x}_\alpha^I - \widetilde{x}_\alpha$
  decompose $V_{\alpha j} = Q_{\alpha i} U_{ij}$ (by QR decomposition)
  solve $U_{ij}\lambda_j = -Q_{\alpha i} r_\alpha$
  update $x_\alpha^{I+1} = \widetilde{x}_\alpha + W_{\alpha i}\lambda_i$
end

Algorithm 2: Simplest version of the IQN algorithm.

3.5.3.2 Compact matrix-free QR decomposition algorithm

The QR decomposition by Householder reflections [114] can be seen as a change of base, from a linearly independent set of vectors sorted in a matrix, to an orthogonal base of the original matrix. The goal is to obtain the orthogonal matrix $Q_{\alpha\beta}$ and the upper triangular matrix $U_{\alpha i}$, with the following shape:

$$Q_{\alpha\epsilon} = {}^1B_{\alpha\beta}\ {}^2B_{\beta\gamma}... \ {}^qB_{\gamma\epsilon} \tag{3.33}$$

$$U_{\alpha i} = {}^qB_{\alpha\beta}... \ {}^2B_{\beta\gamma}\ {}^1B_{\gamma\epsilon} V_{\epsilon i}, \tag{3.34}$$

where $B_{\alpha\beta}$ are intermediate matrices obtained during the iterative decomposition. At each of these iterations, the matrix $V_{\alpha i}$ is modified column by column. We use a left supraindex to identify the corresponding iteration. We do not apply the repeated index convention to the left supraindices. This structure can be considered as a set of q ordered vectors:

$$V_{\alpha i} = \left[\begin{bmatrix} v_{11} \\ v_{21} \\ \vdots \end{bmatrix} \quad \begin{bmatrix} v_{12} \\ v_{22} \\ \vdots \end{bmatrix} \quad \cdots \quad \begin{bmatrix} v_{1q} \\ v_{2q} \\ \vdots \end{bmatrix} \right] = \left[v_{\alpha 1}, v_{\alpha 2}, \cdots, v_{\alpha q}\right]. \tag{3.35}$$

It is worth to remind that the total number of stored iterations q, *i.e.* the rows of $V_{\alpha i}$, will be always much lower than the total number of degrees of freedom p, *i.e.* the columns of $V_{\alpha i}$.

The QR decomposition iteratively makes each column orthogonal to the original base and to each other column in the matrix. The QR decomposition starts iteration j with a matrix ${}^jV_{\alpha i}$ obtained with data from iteration $j-1$.

To decompose the $j-th$ column of ${}^{j}V_{\alpha i}$, a unitary vector u_α has to be built:

$$u_\alpha = \frac{n_\alpha}{\|n_\alpha\|} \quad \text{with,} \quad n_\alpha = v_\alpha - \|v_\alpha\| \, {}^{j}e_\alpha, \tag{3.36}$$

where v_α is the column to decompose and ${}^{j}e_\alpha$ is a unitary vector with $j-th$ position equal to 1 and to 0 otherwise. Then,

$${}^{j}B^{*}_{\alpha\beta} = \delta_{\alpha\beta} - 2u_\alpha u_\beta \tag{3.37}$$

is the Householder matrix associated to the original plane, and $\delta_{\alpha\beta}$ is the identity matrix. If the matrix ${}^{j}V_{\alpha i}$ is premultiplied by ${}^{j}B^{*}_{\alpha\beta}$, a new matrix ${}^{j}B^{*}_{\alpha\beta}\ {}^{j}V_{\beta i}$ is obtained (recall that repeated left supraindices do not sum). The resulting matrix is upper triangular in all the j first columns; and dense everywhere else. For the decomposition of the first column of the matrix ${}^{1}V_{\alpha\beta}$ this would look like:

$${}^{1}B^{*}_{\alpha\beta}\ {}^{1}V_{\alpha i} = \begin{bmatrix} \|v_{\alpha 1}\| & \cdots & \cdots & \cdots \\ 0 & & & \\ \vdots & & {}^{2}V_{\beta j} & \\ 0 & & & \end{bmatrix} \tag{3.38}$$

A new submatrix ${}^{j+1}V_{\beta j}$ is therefore defined as the remainder of ${}^{1}V_{\alpha i}$ after erasing the first column and row. This process can be repeated until the initial matrix becomes upper triangular.

Once the algorithm is computed for all the columns of the original matrix ${}^{1}V_{\alpha i}$, a set of q gradually smaller matrices ${}^{1}B^{*}_{\alpha i} \in \mathbb{R}^{p\times p}$, ${}^{2}B^{*}_{\alpha i} \in \mathbb{R}^{p-1\times p-1}$ ... ${}^{j}B^{*}_{\alpha i} \in \mathbb{R}^{p-(j-1)\times p-(j-1)}$ ... ${}^{q}B^{*}_{\alpha i} \in \mathbb{R}^{1\times 1}$ are obtained. In order to properly compute Equations (3.33) and (3.34), matrices ${}^{j}B_{\alpha i}$ are filled with the identity:

$${}^{j}B_{\alpha i} = \begin{bmatrix} I_{ij} & 0 \\ 0 & {}^{j}B^{*}_{\alpha i} \end{bmatrix} \tag{3.39}$$

where $I_{ij} \in \mathbb{R}^{j-1\times j-1}$. Finally, the matrix $V_{\alpha i}$ is decomposed in an upper triangular U_{ij} and an orthogonal matrix $Q_{\alpha i}$, such that $V_{\alpha i} = Q_{\alpha i}U_{ij}$. The

process is described in Algorithm 3.

l ${}^{1}V_{\alpha i} = V_{\alpha i}$
for *j=1...q* **do**
  choose $v_\alpha = {}^{j}V_{\alpha i}$ with $\alpha = j...p$ and $i = j$
  $n_\alpha = v_\alpha - \|v_\alpha\| e_\alpha$
  $u_\alpha = n_\alpha / \|n_\alpha\|$
  $B^{*}_{\alpha\beta} = I - 2\ u_\alpha\ u_\beta$
  ${}^{j+1}V_{\alpha i} = B_{\alpha\beta}\ V_{\beta i}$
end
$Q_{\alpha\epsilon} = {}^{1}B_{\alpha\beta}\ {}^{2}B_{\beta\gamma}... {}^{q}B_{\gamma\epsilon}$
$U_{\alpha i} = {}^{q}B_{\alpha\beta}\ {}^{q-1}B_{\beta\gamma}... {}^{1}B_{\gamma\epsilon} V_{\epsilon i}$

Algorithm 3: Overview of the QR decomposition algorithm.

In order to improve computing and memory cost, we propose some modifications, especially targeted to solving large-scale problems. As ${}^{j}B_{\alpha\beta}$ is obtained by the relation Equation (3.37), the product ${}^{j}B_{\alpha\beta}\ {}^{j}V_{\beta i}$ can be expanded as:

$$ {}^{j}B_{\alpha\beta}\ {}^{j}V_{\beta i} = (\delta_{\alpha\beta} - 2u_\alpha u_\beta)\ {}^{j}V_{\beta i} = {}^{j}V_{\alpha i} - 2u_\alpha u_\beta\ {}^{j}V_{\beta i}. \tag{3.40} $$

In this way, instead of computing and storing ${}^{j}B_{\alpha\beta}$ of size $p \times p$ for each iteration j, we compute and save q vectors u_α of size p. Moreover, $Q_{\alpha\beta}$, which is used in the backsubstitution (see Equation (3.31)), is never completely computed. Instead, the vector $-Q_{\alpha i} r_\alpha$ is directly computed, using a strategy similar to Equation (3.40). The difference here, is that $Q_{\alpha\epsilon} = {}^{1}B_{\alpha\beta} \cdots {}^{q}B_{\gamma\epsilon}$, so after computing ${}^{q}B_{\alpha i} r_\alpha$, the rest of the matrices $B_{\alpha\beta} = \delta_{\alpha\beta} - 2u_\alpha u_\beta$ have to be premultiplied. For the first product ${}^{q}B_{\alpha\beta} r_\beta$ the expansion is:

$$ {}^{q}B_{\alpha\beta} r_\alpha = (\delta_{\alpha\beta} - 2\ {}^{q}u_\alpha\ {}^{q}u_\beta) r_\beta = r_\beta - 2\ {}^{q}u_\alpha\ {}^{q}u_\beta r_\beta. \tag{3.41} $$

As the result of Equation (3.41) is a vector, the rest of the premultiplications are computed similarly. Note that this algorithm not only avoids building the intermediate matrices $B_{\alpha\beta}$ but also the construction of the final matrix $Q_{\alpha\beta}$ of the QR decomposition. In this way, matrices B in Equations (3.33) and (3.34) are never completely computed and stored. The proposed changes

are described in Algorithm 4.

$\mathrm{l}\ {}^{1}V_{\alpha i} = V_{\alpha i}$
for *j=1...q* **do**
  if $j > 1$ **then**
    ${}^{j+1}V_{\alpha i} = {}^{1}V_{\beta i} - 2u_\alpha u_\beta\ {}^{1}V_{\beta i}$
  end
  choose $v_\alpha = {}^{j}V_{\alpha i}$ with $\alpha = j...p$ and $i = j$
  $n_\alpha = v_\alpha - \|v_\alpha\| e_\alpha$
  ${}^{j}u_\alpha = n_\alpha / \|n_\alpha\|$
end
$U_{ij} = (\delta_{i\gamma} - 2\ {}^{q}u_i\ {}^{q}u_\gamma) \cdots \left(\delta_{\gamma\alpha} - 2\ {}^{2}u_\gamma\ {}^{2}u_\alpha\right) \left(\ {}^{1}V_{\alpha j} - 2\ {}^{1}u_\alpha\ {}^{1}u_\beta\ {}^{1}V_{\beta j}\right)$
$-Q_{\alpha i} r_\alpha = -\left(\delta_{i\gamma} - 2\ {}^{1}u_i\ {}^{1}u_\gamma\right) \left(\delta_{\gamma\beta} - 2\ {}^{2}u_\gamma\ {}^{2}u_\beta\right) \cdots (r_\beta - 2\ {}^{q}u_\beta\ {}^{q}u_\alpha r_\alpha)$

Algorithm 4: Compact matrix-free QR decomposition.

3.5.3.3 Compact matrix-free QR decomposition parallel implementation

When using domain decomposition methods as parallelization strategy [115], work and data are distributed among MPI tasks in partitions of the original discretization. Therefore, the contact surface will also be distributed in this MPI tasks (see Figure 3.2 for a graphical reference) and so the increment matrix $V_{\alpha i}$ (Equation (3.35)).

The proposed algorithm is a collection of matrix-vector and vector-vector products restricted to the contact or wet surface. An efficient parallelization of the algorithm requires a proper point-to-point MPI communication and a fusion of the compact QR decomposition and the backsubstitution step. Therefore, the input of the parallel algorithm will be the $V_{\alpha i}$ matrix and the residuals vectors to operate in the backsubstitution (see Equation (3.31)), and the output will be the coefficient vector α_i. This is what we call it the *Compact IQN algorithm* or CIQN. The whole sequence of steps is described in Algorithm 6.

The mesh partitioner [82] divides the mesh minimizing the area between sub-problems but without any requirements on the wet surface, as depicted in Figure 3.2. Then, we have to derive the upper triangular matrix from $V_{\alpha i}$ in an efficient way. We firstly look for a partition with a number of nodes on the wet surface that is, at least, equal to the amount of iterations stored q. We call this first partition the "leader" partition. With this information, we renumber matrix $V_{\alpha i}$ so the first rows correspond to the leader partition and we start the algorithm.

Two critical operations to parallelize are matrix-matrix product $B_{\alpha\beta}\ {}^{j}V_{\beta i}$ and the matrix-vector product $Q_{\alpha i} r_\alpha$. But if the former product is studied

carefully, it is actually a matrix-vector product. As $B_{\alpha\beta}\ {}^{j}V_{\beta i}$ is obtained by the relation Equation (3.40), the multiplication sequence can be expanded as:

$$(\delta_{\alpha\beta} - 2u_\alpha u_\beta)\ {}^{j}V_{\beta i} = \delta_{\alpha\beta}\ {}^{j}V_{\beta i} - 2u_\alpha u_\beta\ {}^{j}V_{\beta i} = {}^{j}V_{\alpha i} - 2u_\alpha \left(u_\beta\ {}^{j}V_{\beta i}\right). \tag{3.42}$$

Now, the product $u_\alpha\ {}^{j}V_{\alpha i}$ can be computed first, then compute $u_\alpha(u_\beta\ {}^{j}V_{\beta i})$ and finally subtract $I_{\alpha\beta}\ {}^{j}V_{\beta i} - 2u_\alpha u_\beta\ {}^{j}V_{\beta i}$.

To compute U_{ij} (see Equation (3.34)) we proceed similarly, but this time the first operation is $(\delta_{\alpha\beta} - 2\ {}^{1}u_\alpha\ {}^{1}u_\beta)V_{\beta i}$ and the rest of the matrices $(\delta_{\alpha\beta} - 2u_\alpha u_\beta)$ are premultiplied. Something similar happens with $Q_{\alpha i}r_\alpha$. The first multiplication, detailed in Equation (3.41) can be expanded as:

$$(\delta_{\alpha\beta} - 2\ {}^{q}u_\alpha\ {}^{q}u_\beta)r_\beta = \delta_{\alpha\beta}r_\beta - 2\ {}^{q}u_\alpha\ {}^{q}u_\beta r_\beta = r_\alpha - 2\ {}^{q}u_\alpha\,(\ {}^{q}u_\beta r_\beta) \tag{3.43}$$

The product ${}^{q}u_\beta r_\beta$ is firstly computed and then $r_\alpha - 2\ {}^{q}u_\alpha(\ {}^{q}u_\beta r_\beta)$. The resulting vector is multiplied by $\delta_{\alpha\beta} - 2\ {}^{(q-1)}u_\alpha\ {}^{(q-1)}u_\beta$ until $\delta_{\alpha\beta} - 2\ {}^{1}u_\alpha\ {}^{1}u_\beta$ is multiplied. In this way, matrices ${}^{q}B_{\alpha i}$ are never completely computed, we only compute those entries that are needed. The steps to compute Equations (3.42) and (3.43) are depicted in left and right sides of Algorithm 5.

function `SMat_x_mat()`

Data: v_α and $V_{\alpha i}$
Result: $AUX_{\alpha i}$

$aux_i = v_\alpha V_{\alpha i}$
`MPI_SUM(`aux_i`)`
$AUX_{\alpha i} = V_{\alpha i} - 2v_\alpha aux_i$

`return` $AUX_{\alpha i}$

function `SMat_x_vec()`

Data: v_α and r_α
Result: aux_α

$a = v_\alpha r_\alpha$
`MPI_SUM(`a`)`
$aux_\alpha = v_\alpha - 2v_\alpha a$

`return` aux_α

Algorithm 5: Parallel implementation. Algorithms for computing the products $B_{\alpha\beta}V_{\beta i} = (\delta_{\alpha\beta} - 2u_\alpha u_\beta)\ {}^{j}V_{\beta i}$ (left) and $B_{\alpha\beta}r_\beta = (\delta_{\alpha\beta} - 2u_\alpha u_\beta)\ {}^{j}r_\beta$ (right).

The backsubstitution is computed once U_{ij} and $Q_{\alpha i}r_\alpha$ are built in parallel. As all the non-zero elements of the upper triangular matrix U_{ij} are located in the leader partition, so this operation is computed only in this MPI task, with no extra communication. Finally the λ_i vector is scattered to the rest of sub-problems, obtaining the result of the parallel algorithm. The complete CIQN algorithm is depicted in Algorithm 6. We remark again that thanks to the fusion between the QR decomposition and the preoperations

for the backsubstitution, intermediate matrices (such as ${}^{q}B_{\alpha i}$) are never completely computed and stored.

Initialize problem and Chose leader partition
while *not the last time step* **do** ▷ `time loop`
  $x_\alpha^0 = x_\alpha^{ini}$
  $\widetilde{x}_\alpha^0 = H(x_\alpha^0)$
  $r_\alpha^0 = \widetilde{x}_\alpha^0 - x_\alpha^0$
  update $x_\alpha^1 = \widetilde{x}_\alpha^1 + \omega_0 r_\alpha^0$
  while *problem not converged* **do**
    $\widetilde{x}_\alpha = H(x_\alpha)$
    $r_\alpha = \widetilde{x}_\alpha - x_\alpha$
    build $V_{\alpha i} = \left[\Delta r_\alpha^{I-1}, ..., \Delta r_\alpha^0\right]$; with $\Delta r_\alpha^I = r_\alpha^I - r_\alpha$
    build $W_{\alpha i} = \left[\Delta \widetilde{x}_\alpha^{I-1}, ..., \Delta \widetilde{x}_\alpha^0\right]$; with $\Delta \widetilde{x}_\alpha^I = \widetilde{x}_\alpha^I - \widetilde{x}_\alpha$
    ${}^{1}V_{\alpha i} = V_{\alpha i}$
    for *j=1...q* **do** ▷ `QR decomposition loop`
      if $j > 1$ **then** ${}^{j+1}V_{\alpha i} = {}^{1}V_{\beta i} - 2u_\alpha u_\beta \, {}^{1}V_{\beta i}$
      if *I am the leader* **then**
        $v_\alpha = {}^{j}V_{\alpha i}$ with $\alpha = j...p$ and $i = j$ (cropped)
      else
        $v_\alpha = {}^{j}V_{\alpha i}$ with $\alpha = 1...p$ and $i = j$ (not cropped)
      end
      parallel compute $\|v_\alpha\|$
      if *I am the leader* **then** $n_\alpha = v_\alpha - \|v_\alpha\| \, {}^{j}e_\alpha$
      parallel compute $\|n_\alpha\|$
      $u_\alpha = n_\alpha / \|n_\alpha\|$
    end
    $U_{ij} = (\delta_{i\gamma} - 2 \, {}^{q}u_i \, {}^{q}u_\gamma) \cdots \left({}^{1}V_{\alpha j} - 2 \, {}^{1}u_\alpha \, {}^{1}u_\beta \, {}^{1}V_{\beta j} \right)$
    $-Q_{\alpha i} r_\alpha = - \left(\delta_{i\gamma} - 2 \, {}^{1}u_i \, {}^{1}u_\gamma\right) \cdots (r_\beta - 2 \, {}^{q}u_\beta \, {}^{q}u_\alpha r_\alpha)$
    if *I am the leader* **then** backsubstitute $U_{ij}\lambda_j = -Q_{\alpha i} r_\alpha$
    $x_\alpha^{I+1} = \widetilde{x}_\alpha + W_{\alpha i}\lambda_i$ ▷ `variable update`
  end
end

Algorithm 6: Compact Interface quasi-Newton (CIQN) algorithm.

3.5.4 Boundary conditions for the fully coupled fluid-electro-mechanical problem

In this section we discuss the boundary conditions for the fully coupled problem.

Electrophysiology Equation (2.1) is the continuum model for the electrophysiology depolarization. Neumann zero-flow boundary condition is imposed everywhere: $\phi n_i = 0$, where n_i is the surface normal vector. As initial condition, the system is excited with a nodal variation of the voltage. This stimuli can be imposed as a voltage or as a current density. Except specified the contrary, the left and right endocardial surfaces are excited synchronously. In the heart, the Purkinje network is in charge to depolarize these two structures. As the Purkinje network is distributed along the vast majority of the endocardium [116] and the depolarization process occurs in a few miliseconds, exciting both of the inner ventricular surfaces synchronously is a good approximation for this initial excitation. Despite we acknowledge this is a simplified approach, not valid for complex electrophysiology scenarios, it is still useful when the main interest is not in the electrophysiology behavior.

Solid mechanics As said in Section 1.2.4, physiologic deformation of the ventricles includes a displacement of the valvular plane towards the apex of the ventricle, inducing apex-base shortening. In this way, articles that have reported results with excessively constrained boundary conditions like fixing the base of the heart, cannot reproduce at all the physiological movement of the ventricles. In [117, 118] authors from two different research groups propose a pericardium boundary condition as a frictionless contact problem. In [119] we propose a solution that with a different approach achieves a similar result, which is used in this work. We propose to restrict the normal displacements $d_i n_i = 0$ at the ventricular pericardium for the *deformed* configuration while allowing free displacements at the tangential planes, letting the boundary to slide. As a matter of fact, the "sliding pericardiaum" condition is not imposed in all of the pericardium, because we leave free the region near the valve plane to allow a more uniform and realistic movement. We acknowledge that this condition is a first order approach, because a better one should allow some normal movement but with a damper, combining a spring and a velocity-related viscous force. In this work we show that even with the first order approach, the improvement is clear. The forces computed by the fluid mechanics are imposed in the endocardium. It is worth to remark that in our simulations, there is no other artificial endocardium boundary condition imposed. When used in the reviewed articles, such condition is applied on the normal direction (*i.e.* pressure) through a Windkessel function. Authors using this approach have the intention to model the work done by the fluid against the endocardium, as it is pumped out of the ventricles. However, when simulating single or bi-venticular geometries, applying this force requires to also fix the heart displacement somewhere else. As it is clearly shown in [56], when a pressure endocardium function is combined with fixing the base the resulting systolic movement is incorrect. In

[56], although ventricles contract along their long-axis, the apex has a large displacement in apex-base direction and the base remains, of course, fixed. Although this can be visually corrected (quoting [56], *"For visualization we shifted the deformed configuration such that the apex is fixed"*) this effect is not physiologically correct. On the other hand, we have observed that the pericardium and endocardium boundary conditions proposed in this work, produce a much more physiologically realistic movement.

Fluid mechanics As stated in Equations (2.11) and (2.12) we enforce continuity of interface unknowns in the wet surface. This means that an input force is added to the right hand side of Equation (2.7) through the Equation (2.13) as a weakly imposed Neumann boundary condition. No slip condition $v_i = 0$ is also used on the wet surface for the fluid mechanics problem. For the outflow boundaries, as flow may not always be fully developed, a stabilization boundary condition must be used. Here we use the technique described in [120]:

$$\mathbf{n}^T \boldsymbol{\sigma} \mathbf{n} + C_a \int_{\Gamma_{out}} \mathbf{v}\mathbf{n} d\Gamma_{out} + p_0 = 0, \tag{3.44}$$

with:

$$\boldsymbol{\sigma}\mathbf{n} = -p\mathbf{n} + 2\mu\nabla\mathbf{v}\cdot\mathbf{n} - \rho^f \left(\{\mathbf{v}\cdot\mathbf{n}\}_-\right)\mathbf{v}, \tag{3.45}$$

where Γ_{out} are the boundary surfaces to impose Equation (3.44), ρ_f is the fluid density and the term $\{\mathbf{v}\cdot\mathbf{n}\}_-$ denotes the negative part of $\mathbf{v}\cdot\mathbf{n}$, this is to say $\{\mathbf{v}\cdot\mathbf{n}\}_- = \mathbf{v}\cdot\mathbf{n}$ if $\mathbf{v}\cdot\mathbf{n} > 0$ or $\{\mathbf{v}\cdot\mathbf{n}\}_- = 0$ otherwise. The term $\mathbf{n}^T\boldsymbol{\sigma}\mathbf{n}$ stabilizes the outflow, while the integral term in Equation (3.44) acts as an order-zero Windkessel model, imposing a pressure proportional to the outflow.

Arbitrary Lagrangian-Eulerian problem The boundary conditions for the ALE problem are Dirichlet everywhere. In the wet boundary Γ_c where the displacements computed in the solid problem are imposed (see Equation (2.11)). Otherwise, it is set to zero deformation.

3.5.5 Summary of the fluid-electro-mechanical heart model

Features of the model To sum up, the model presented in this thesis includes:

- A human cell electrophysiology model.
- A bidirectionally coupled electro-mechanical model of the myocardium, with passive and active stresses and a popularly accepted solid material model.

- A bidirectional FSI formulation for the contained fluid using the ALE method.
- A whole heart geometry of an average healthy human heart, including atria, ventricles, and great vessels.
- Detailed boundary conditions for the electrophysiology, solid and fluid mechanics.
- Anisotropic electrophysiology and mechanical ventricles behavior.
- High space resolution for both tissue and blood, solved in large-scale tetrahedral meshes.

Limitations The presented model does not include:

- Purkinje network model. Despite not including a Purkinje network, the electrophysiology model is excited in a physiologically accurate manner.
- Valve model. 3D modelling of the heart valves is a scientific challenge by itself [121, 122, 123, 124]. Also, the ALE method used in this work is not convenient to model them, as the fluid mesh will invert for sure when the valves are about to close completely.
- Fluid mechanics model of the atrium. As the atrium has thin walls and a complex geometry [125], the FSI problem becomes more unstable, due to the smaller inertia of the muscular structure. Also, to include the fluid dynamics of the atria, a model for the atrioventricular valves should be included, enormously increasing the computational cost of the problem. As there is no fluid model of the atrium, diastole is not modeled.
- A non-Newtonian rheological description of the blood.

In the next chapter, this model is used to compute simple and advanced simulations.

Chapter 4

Basic experiments in simplified geometries

The only difference between
science and screwing around
is writing it down.

Adam Savage

Summary:

The objective of these basic simulations is to verify and test different single and coupled problems that are present in the heartbeat. Three different types of numerical experiments are proposed: simple electrical propagation cases, coupled electro-mechanical experiments, and fluid-structure interaction results. The first case is designed to validate the electrophysiology model. After that, the second set of experiments tests the solid mechanics conditions defined in the previous chapters. Finally, the fluid-structure interaction CIQN algorithm is tested and validated, leaving temporarily aside the electrophysiology modelling. The three sets of simple experiments presented in this chapter act as a prologue to the whole heart numerical experiments in next chapter.

4.1 Electrical propagation simulations

The goal of this section is to validate the electrophysiology model. For this reason, we reproduce the gold-standard test presented in [126].

4.1.1 Mesh convergence

The objectives of this case is to verify the electrophysiology model against benchmarking data, and to verify that the solution converges while the

computational mesh is refined. In order to achieve this, we replicate the test proposed in [126]. In the cited work, eleven simulation codes are used to solve a predefined problem and mesh convergence results are presented and compared between them. In this work we use the same geometry, boundary conditions and mesh but a different cell model.

Description For this experiment, we use the human cell model of O'hara-Rudy [29] instead of the [57] originally used in [126]. For the electrical diffusion, the parameters proposed in [26] were used. To create the meshes for the convergence test, a mesh division technique [127] is used to refine the slab in Figure 4.1. The element sizes chosen are 0.5, 0.25, 0.125 and $0.06125[mm]$, resulting in: 20k, 165k, 1.5M and 10M tetrahedra respectively.

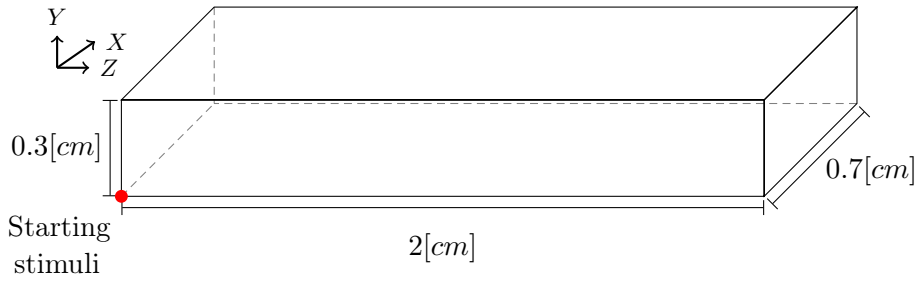

Figure 4.1: Electrophysiology set-up. Scheme of the geometry proposed by [126].

Velocity of the electrical depolarization is measured along the major diagonal of the slab, as described in [126]. If activation time is plotted against distance, the slope of the curve represents the inverse of the wave velocity.

Results Results are presented similarly as done in [126]. In Figure 4.2 we plot the activation time, as a function of the length for the different meshes that have been tested. The slice shows the activation time for the geometry.

Results are comparable to those of [126]. As expected, at large element sizes, there is a slow wave velocity, a behavior has been previously shown in [128]. When the mesh is refined, conduction velocity converges ([33, 129]). Previous works ([30, 130, 126]), suggest that a spatial discretization of $200[\mu m]$ should be enough for simple propagation. However, in [27] the authors suggest that this may be too coarse to simulate chaotic behaviors like reentrance. If simulating complex electrophysiology conditions is not the main objective, a trade off solution can be achieved where the conductivity values are tuned until physiological activation times are obtained. This

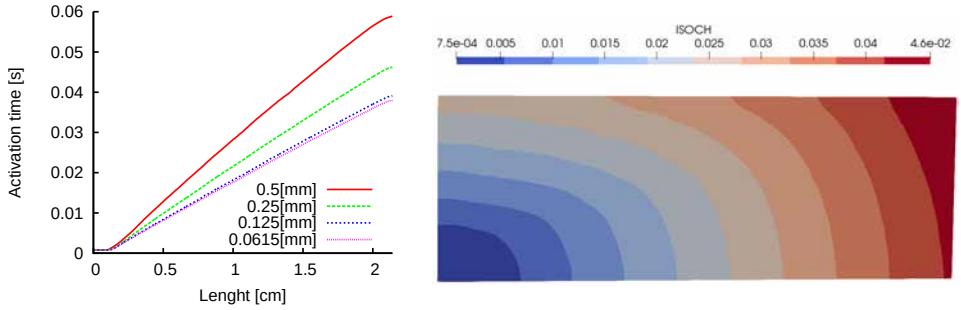

Figure 4.2: Electrophysiology set-up Left: mesh convergence for a given set of parameters. Right: activation time (isochrones) for a converged simulation.

technique has been used in the past by other authors such as [56]. We conclude that for the cases solved in this work, a mesh discretization under $200[\mu m]$ is enough.

4.2 Coupled electro-mechanical simulations

In this section, we couple the solid mechanics model to compute electro-mechanical simulations. Four sets of experiments are presented. First, we show results for a simple contracting hexahedron, originally presented in [56]. Then, using the bi-ventricular geometry, we compare the solution for the sliding pericardial boundary condition against two other options. Then, using the same bi-ventircular geometry, different fibre distributions are tested. Finally, we compute an electro-mechanical simulation of the whole heart geometry to compare results against the bi-ventricular geometry. The aim of this section is to evaluate the electro-mechanical module and to test the proposed boundary condition and the possible fibre fields.

4.2.1 Contracting hexahedron: a simple reproducible test

In [56] the authors show qualitative results for a simple contractible hexahedron. Here we repeat the experiment, but including quantitative comparable results. A secondary objective of this case is to propose quantitative results for the experiment, to ease comparison for other authors.

Description A $16 \times 12 \times 20\,[mm]$ hexahedron is used, discretized with a $0.25\,[mm]$ element size, resulting in a 1.5M elements mesh. The electrophysiology model is excited in a corner (the $(0.0, 0.0, 0.0)$ node). The solid is free to move in every direction except for the three faces of the cuboid that coincide in the starting stimulus point. In these boundaries (Γ_e, zero normal displacements (${}^{sld}d_i^{\Gamma_e} n_i = 0$) are imposed, while the tangential

direction is free to move. The fibres are aligned with the major axis (Z) of the geometry, representing a slab of cardiac tissue with homogeneous fibres. Displacements are measured in the corner opposite to the starting stimulus vertex. See Figure 4.3 for a geometry description.

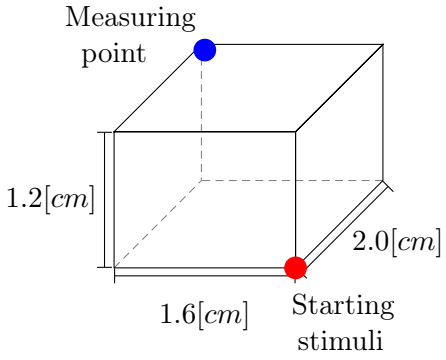

Figure 4.3: Electro-mechanical simulations. Scheme for the geometry (proposed in [56]). Starting stimulus point and measuring points are marked.

Results Left side of Figure 4.5 show the simulation results analogously as done in [56]. A similar contraction of the cuboid is obtained. In order to complement the study, we plot displacement increments (ΔX,ΔY, ΔZ) for a measuring point. To measure the electrical activity, the total charge in the domain is integrated and normalized from 0 to 1, a measure called "normalized electrical depolarization". In the left side of Figure 4.5 we show the normalized depolarization and (ΔX,ΔY, ΔZ) displacements. In the right side, there is a sequence of images for the simulation.

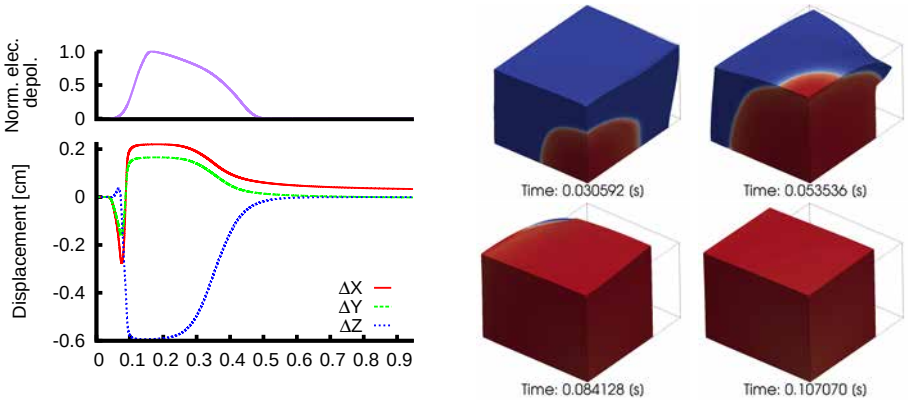

Figure 4.5: Electro-mechanical simulations. Left: normalized electrical depolarization and displacement increments (ΔX,ΔY and ΔZ) for the measuring point. Right: simulation snapshots.

The results obtained in this section are comparable to the qualitative results shown in [56]. Considering the nodal measurement presented in this thesis, the stretch rate can be computed as $(L_{ini} - \Delta Z_{max})/L_{ini}$, where L_{ini} and ΔZ_{max} are the original length of the slab and the maximum deformation in the contracting direction respectively. The resulting maximum stretch rate is 70%, a value comparable with the 75% measured in [131] for an experimental setup.

4.2.2 Sliding pericardium boundary condition

In this numerical experiment, we perform a study to show the importance of considering physiological boundary conditions in cardiac modelling. As explained in Section 1.2.4, the movement of the heart is modulated by the action of the surrounding tissues. As it has been shown by the new imaging techniques (see Section 1.2.4), cardiac long-axis contraction causes the base to move down rather than the apex to move up. Particularly, the pericardium acts as a sort of sliding surface, avoiding normal displacements of the epicardium, but leaving the tangential direction almost free to move. To prove this, we compare results for three different solid mechanics boundary conditions against experimental results.

Description We use the bi-ventricular geometry described in Section 3.2.3. To analyze and compare the results between the different numerical experiments, the geometry is divided using the 32 segments partition described in [132]. This segmentation of the ventricles also includes the 17-segment American Heart Association (AHA) classification (see Figure 4.6).

In order to compare numerical against experimental results, we compute the longitudinal strain ($L_{\%}$) for each segment. A similar measurement is also given by speckle-tracking echocardiography [133]. To obtain this value, we compute a weight-averaged integration of the Green-Lagrange strain tensor E_{ij} for each segment. The normal deformation along the unit apex-base vector abv_i (see Figure 4.6) is calculated and divided by the volume of each segment:

$$L_{\%} = \frac{\left(\int_{\Omega_{seg}} E_{ij}\ abv_j\ dV_{\Omega_{seg}}\right)\ abv_i}{\int_{\Omega_{seg}}\ dV_{\Omega_{seg}}}. \tag{4.1}$$

The assessment is done by running three cases: no boundary condition for displacements (labelled as “Free” or “F”), fixing only the ventricular base displacements (labelled as “Fixed top” or “T”) and using a sliding pericardial boundary condition (labelled as “Sliding pericardium” or “SP”, see Section 3.5.4).

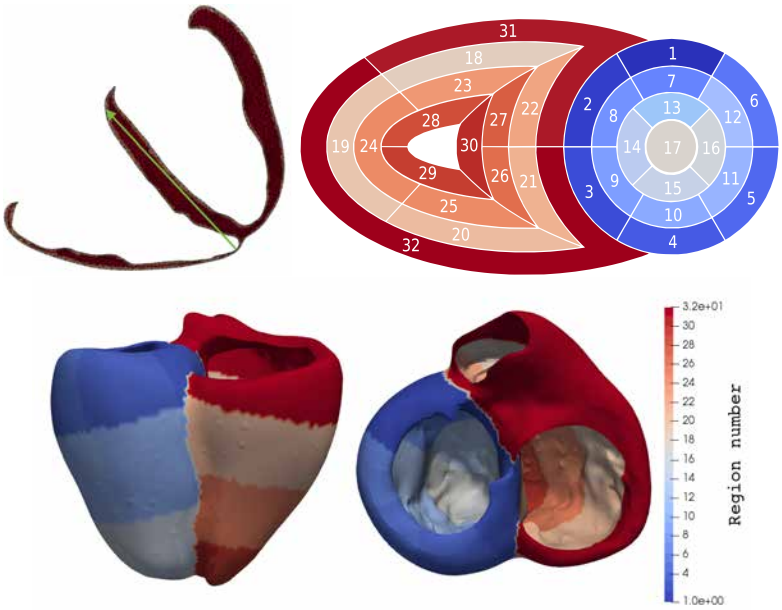

Figure 4.6: Pericardial boundary condition. The top left figure shows a slice of the geometry and the apex-base unitary vector (abv_i = (−0.75, 0.57, −0.327) for the original Zygote coordinates). The other figures show a scheme of the 32 segment representation [132] and the correspondent mapping in a frontal and top view of the ventricles.

Results The results for the three boundary conditions (F,T and SP) are shown in Figure 4.7. Plot Figure 4.7.A shows normalized electrical depolarization as a reference. The following three plots (Figure 4.7.B, Figure 4.7.C and Figure 4.7.D) show overall, basal and apical longitudinal strain, respectively. Then, snapshots for the three boundary conditions are shown in Figure 4.7.E . From left to right: Free (F), Base fixed (T), and sliding pericardium (SP). Finally, the longitudinal strain is shown in the AHA plot segment-wise for each case in Figure 4.7.F.

The sliding pericardium boundary condition shows a reduced overall longitudinal strain $L_{\%}$ if compared against the other two cases. Despite this, the apical and basal deformations follow a more physiological dynamic. Due to the sliding pericardium, apical deformation is restricted to move. For the same reason, the base moves down. The bottom part of Figure 4.7 shows three geometries with their respective 32-segments plot, compared at $t = 120[ms]$, reinforcing the stated above. Note that in the case of the "free" condition the ventricles contracts in a relatively uniform way. In the "fixed top" condition, the ventricles largely contract upwards and inwards. Finally, in the "sliding pericardium" condition, ventricles retain their pericardium perimeter, while moving down the base and, consequently, thickening the

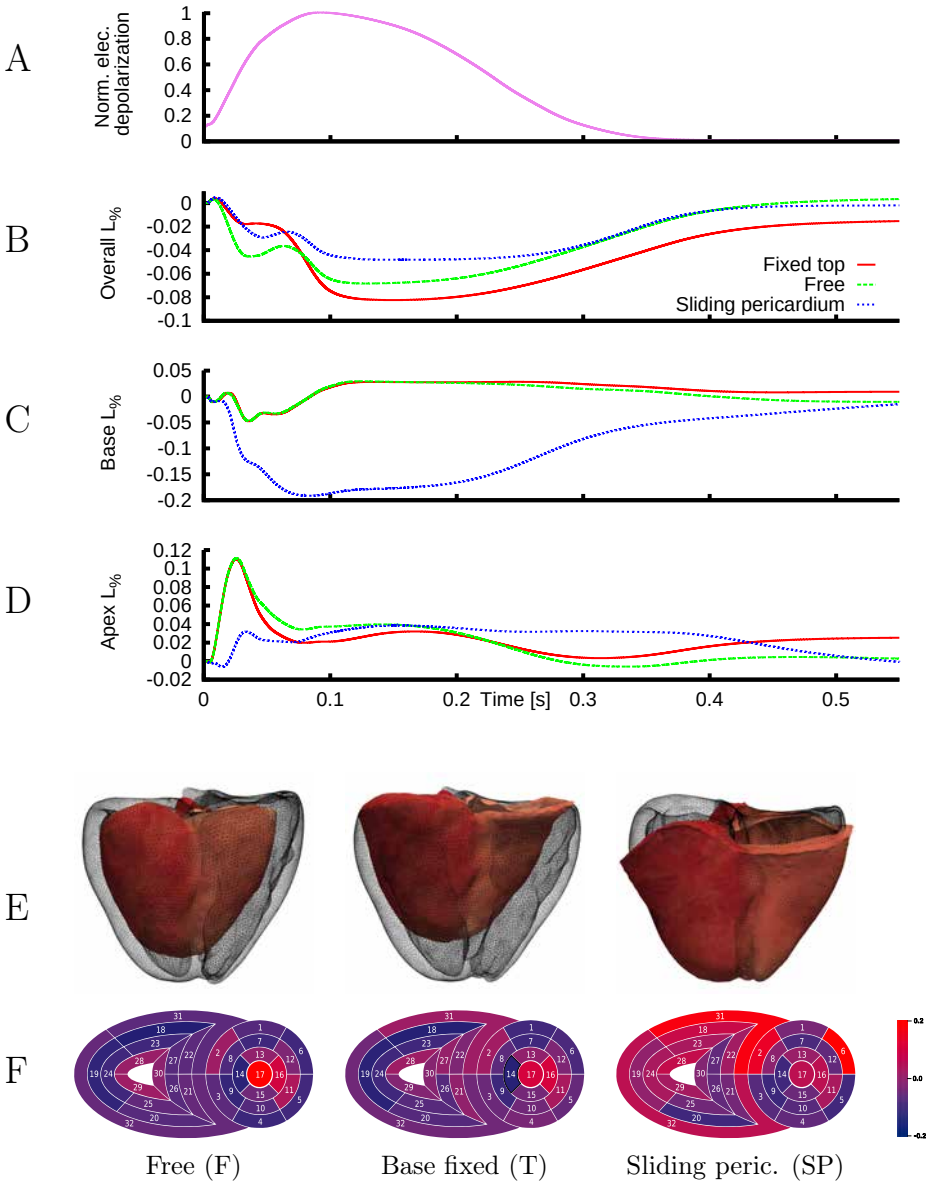

Figure 4.7: Effect of pericardium boundary condition in a bi-ventricular geometry. Normalized electrical depolarization is shown as a reference for the reader (A). The following three plots show overall (B), basal (C) and apical (D) longitudinal strain, respectively. Then (E), snapshots at maximum contraction ($t = 120\,[ms]$) for the three boundary conditions are shown. From left to right: Free (F), Base fixed (T), and sliding pericardium (SP). Finally (F), the longitudinal strain is shown in the AHA plot segment-wise for each case.

ventricle walls (recall that the upper pericardium is left free to move, as seen in the figure). It is observed that the sliding pericardium condition highly reduces apex lift-up while allowing a maximum of 20% average base move-down.

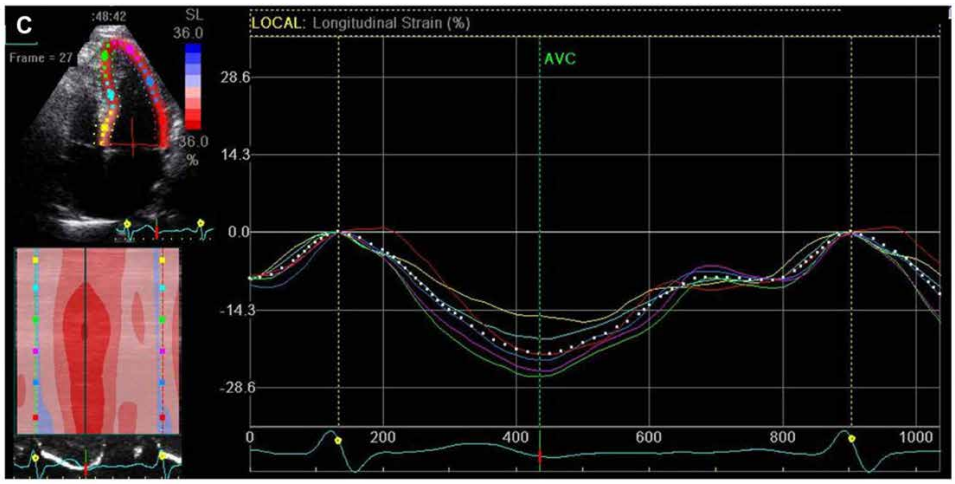

Figure 4.8: Effect of sliding pericardium in myocardial dynamics. Longitudinal strain measurements captured using speckle tracking echocardiography for a healthy heartbeat. Image taken from [19].

It is worth to mention that the curves for the proposed condition also match those obtained experimentally using speckle tracking techniques, like it is observed in Figure 4.8 (taken from [19]). There are appreciable similarities between the $L_{\%}$ curves in Figure 4.8 and the overall and basal $L_{\%}$ curves in Figure 4.7 for the SP condition. On the contrary, the base $L_{\%}$ for the T and F cases remains relatively flat for thorough all the contraction, and cannot be assimilated to any curve in Figure 4.8. Using the proposed sliding pericardial boundary condition (SP), the epicardium surface stays in place, but allows tangential displacements. With this condition the base of the heart contracts in the apical direction. On the contrary, by fixing vertical displacements at the base (T), it is obtained a non-physiological myocardial deformation. In the same way, leaving the heart free to deform everywhere (F), also gives a non-physiological deformation, with excessive apex displacements. The fact that this measure allows us to compare numerical and experimental results, suggest that the described measuring technique may be a valid way to validate electro-mechanical cardiac models.

In this way, the sliding pericardial boundary condition (SP) is used in the whole heart model, except specified otherwise. This boundary condition provides a physiological displacement of the base towards the apex, as explained in Section 1.2.4. This also induces a thickening of the myocardium that help to reduce the ventricular cavities and therefore eject the containing

blood.

4.2.3 Effect of the angle variation in the rule-based model of fibre distribution

In this experiment, we test the impact in myocardium deformation produced by two different versions of fibre fields. The rule-based method used in this thesis (Streeter method, described in Section 3.2.2) allows to generate linear and cubic fibres for the myocardium. The difference between them is that the angle varies from the endocardium to the epicardium, with a linear or a cubic function (see Figure 3.7 for a graphical reference). The main goal of this experiment is to quantify the deformation of both cases and choose the version (linear or cubic) that better resembles the experimental measurements.

Description Linear an cubic fiber configurations (see Figure 3.7) computed by Streeter rule-based method in the bi-ventricular geometry are tested. In both cases, the test are run using the same simulation conditions, including the sliding pericardium condition studied before.

Results Results are shown in Figures 4.9 and 4.10. In Figure 4.9, the surface represents results for the linear fibre distribution and the outline, for the cubic distribution. In both figures, minimal differences can be appreciated.

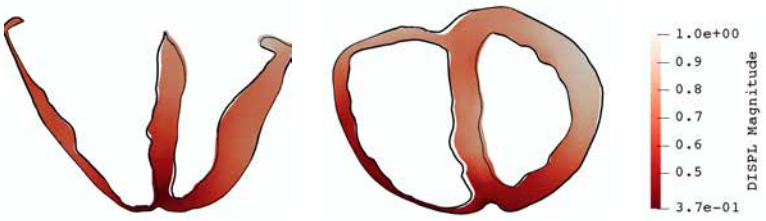

Long axis Short axis

Figure 4.9: Effect of the fiber distribution in the bi-ventricular study. The surface plot shows the linear fiber distribution, and the outline shows the cubic fiber distribution. Long and short axis slices are shown for both configurations at $t = 120[ms]$.

In Figure 4.10.A, normalized electric depolarization is shown, together with longitudinal strain for the base (Figure 4.10.B) and the apex (Figure 4.10.C). Both sets of fibers are compared. In the same figure, long

and short axis slices of the ventricles are shown. The overall second invariant (Figure 4.10.D), used to show cutting stresses, is also shown.

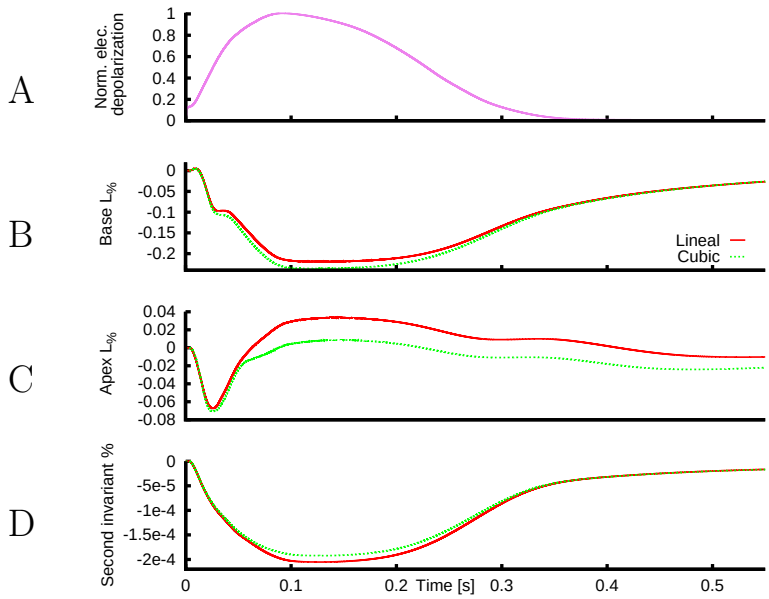

Figure 4.10: Effect of the fiber distribution in the bi-ventricular study. Cubic and linear distributions are compared. Similar basal and apex longitudinal strains are observed, with a appreciable difference in the apical deformation. The overall second invariant, showing the cutting stresses, is also shown.

Results in Figures 4.9 and 4.10 show small differences between both types of fibres. As expected, the fibre angle interpolation function does not drastically modify the overall deformation of the ventricles. Despite this, there is a sensible reduction ($\sim 30\%$) in the apex longitudinal strain, when cubic fibers are used. In the literature [8, 134, 135, 136], a dominant mass of circumferential fibers in the myocardium is described. Due to this histological fact and supported by the reduced apex deformation, we suggest to use a cubic interpolation to build the fibers instead of a linear function.

4.2.4 Mechanical effect of the atrium

Traditionally, cardiac simulation papers focus on geometries with isolated ventricles (one or both). But, anatomically speaking, and specially if electro-mechanical or fluid-electro-mechanical models are used, atria presence strongly conditions the overall movement. In this section, we show the importance of this effect.

Description In this case, we use the whole heart geometrical model shown in Figure 3.4, where the atrio-ventricular plane is closed, filling inner cavity of the atrium with an isolineal soft material (see a complete description in Section 3.2.1). With this configuration, the atria offers a small resistance to stresses but inertially behaves like blood due to its density. This condition is also reasonable when studying ventricular systole because, when ventricles contract pumping out blood through the aortic and pulmonary valves, the atria remains almost entirely filled with the atrio-ventricular valves tightly closed. The advantage of this set-up is that we are able to simulate a whole heart in ventricular systole without modelling the Fluid-Structure Interaction (FSI) problem in the atrium or the atrioventricular valves. We compare results of the whole-heart with a more traditional bi-ventricular geomety. In both geometries, cubic fibres and the sliding pericardium boundary condition are used.

Results Figure 4.11 shows a slice for the whole heart and the bi-ventricular geometries at at the maximum contraction point. These results are complemented with Figure 4.12, where basal and apical longitudinal strains are shown.

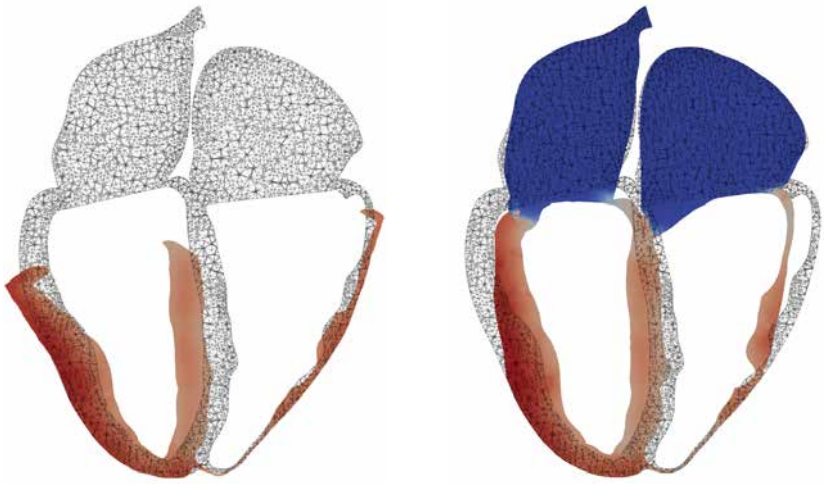

Bi-ventricular Whole heart

Figure 4.11: Mechanical effect of the atria presence. Left side compared a bi-ventricular simulation against the whole-heart undeformed mesh. Right side shows the whole heart simulation against the original mesh.

As it can bee seen in Figures 4.11 and 4.12, the atrium have a critical effect in the ventricular dynamics due to the associated mass of these structures. Basal longitudinal displacement is reduced, due to the inertial

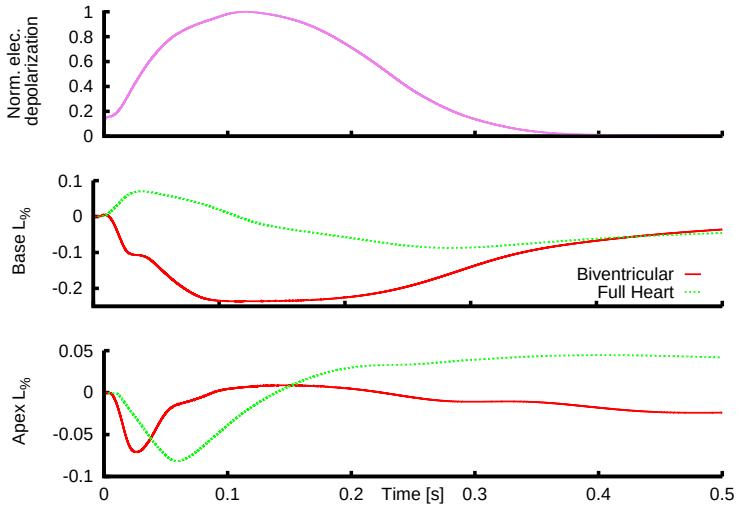

Figure 4.12: Mechanical effect of the atria presence. Normalized electrical depolarization is shown for reference, together with base and apex longitudinal strain. The effect of the atria presence can be seen not only in the base, restraining its deformation due to the mass of the added structures but also, with a smaller impact, in the apex.

effect produced by the directly connected structure. Deformation of the apex is also affected, but not as drastically as the apical deformation. If the orthogonal plane is analyzed, the atria act as constraining structures, reducing the basal area while it contracts. This effect also induces a non-physiological stretch in the valvular plane, produced by the rather rigid material used in this artificial closure. Ventricular deformation is clearly different when both atria are included in the geometry.

Despite some non-physiological effect is seen in the artificial closure plane, using th atria allows us to have a watertight intraventricular space, including also the sliding pericardium boundary condition. Although great advances have been achieved using ventricle-only geometries, including atria in the simulations is recommendable even for ventricular mechanics due to the intimate relation between these two sets of chambers.

4.3 Bidirectional fluid-structure interaction test simulations

In this section, we validate and test the novel Compact interface quasi-Newton (CIQN) algorithm proposed in this thesis with pure FSI problems (without solving electrophysiology). Two experiments are presented. The first case, is a validation simulation. The main goal of this first case, is

to show that the numerical technique developed to solve the FSI problem faithfully reproduces the physics. The second case is specially designed to test all the features required for heart simulations. In this complex case, the goal is to prove that the CIQN technique can deal with added mass instability and with multiple coupled surfaces.

4.3.1 Algorithm validation

The main objective of this case is to validate the CIQN algorithm presented in Section 3.5 with the "Turek" benchmark [137].

Description In this test, a flexible bar hold by a rigid circumferential body oscillates due to a laminar flow. These oscillations produce vortices in the fluid, closing the bidirectional loop. Amplitude of displacement and frequency are measured in the tip of the rod and are used to check the results. Such problem is extensively described in section *4.3* of [137]. With this experimentally and numerically reproducible case, the CIQN coupling algorithm can be validated.

Results A snapshot of the simulation is shown in Figure 4.13.

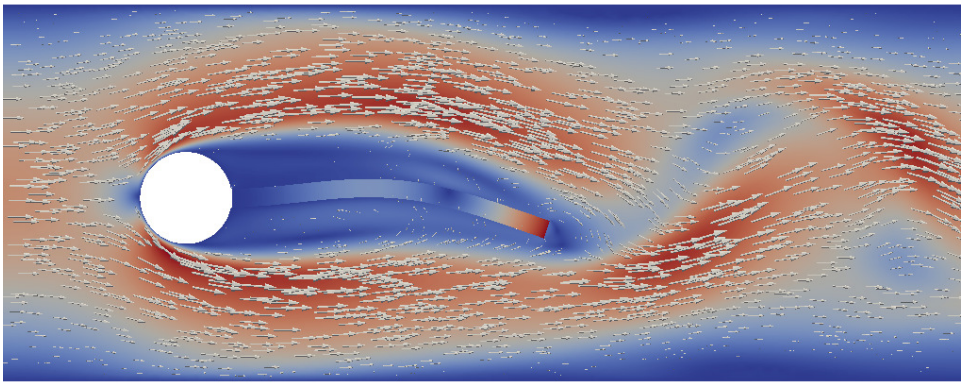

Figure 4.13: Method Validation. Part of the domain proposed by [137] in time $t = 3\,[s]$. Deformation is represented on the bar and velocity field in the fluid domain.

The obtained amplitude and frequency on the quasi-periodic period are $A_x = -2.60 \times 10^{-3} \pm 2.40 \times 10^{-3}\,[f = 10.8]$ and $A_y = 2.3 \times 10^{-3} \pm 33.7 \times 10^{-3}\,[f = 5.4]$, agreeing with the $A_x = -2.69 \times 10^{-3} \pm 2.53 \times 10^{-3} [f = 10.9]$ and $A_y = 1.48 \times 10^{-3} \pm 34.38 \times 10^{-3}\,[f = 5.3]$ obtained in the original experiment[1]. In [137] the numerical experiment is validated against a physical experiment. With this, we can say that our algorithm faithfully

[1]The results are presented as in the original experiment: mean $\pm$amplitude$[freq]$.

validates the involved physics in the FSI problem. It is worth to remark that the same validation test and with similar results is also presented in [81], using Alya as a solver, but with a different coupling strategy.

4.3.2 A biomedically inspired problem: a 3D 2-field case

This numerical experiment is designed to test the performance of the CIQN algorithm against two other relaxation schemes widely used: Broyden [109] and Aitken [108] methods. To do this comparison, we propose a biomechanically inspired case: a filled flexible tube is lying in a flexible surface which is in contact with a big volume of another fluid. The reader can think about this academic example as a coronary artery close to the endocardium, that is in contact with the blood inside the ventricle.

Description A scheme of the geometry used is shown in Figure 4.14. A

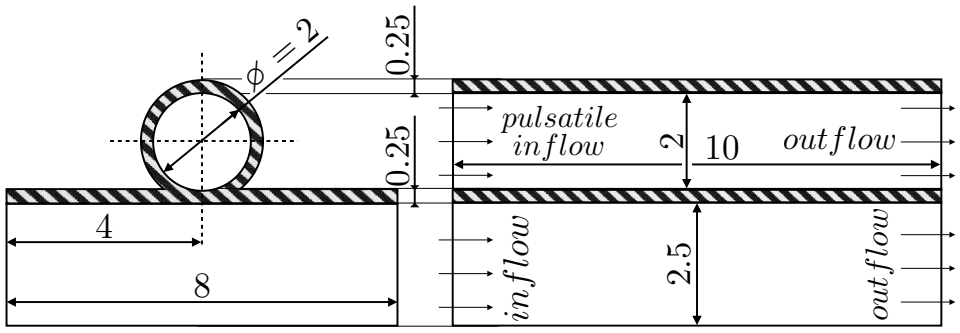

Figure 4.14: Biomedically inspired FSI case. Geometry, showing dimensions and fluid direction.

constant velocity is imposed in the bigger fluid domain and an oscillating velocity in the distensible tube. The fluid mesh has 10187 elements and the solid mesh 76280. Time step is $\Delta t = 0.1[s]$. Bulk properties for the fluid are: $\rho_f = 1[g/cm^3]$ and $\mu = 0.03[Poise]$. Bulk properties for the solid are $\rho_s = 1[g/cm^3]$, $E = 1.5E4[Baryes]$ and $\nu = 0.3[-]$. The inflow velocity profile is $\mathbf{v} = (0, 0, 1.0/sin(2\pi t))[cm/s]$. The geometry and physical properties are prone to induce added mass instability ($\rho_s/\rho_f = 1$) and a complex interface problem (with two wet surfaces to couple with different dynamics).

Continuity of displacements and stresses are imposed in the contact boundary (see Section 2.5.2). No-slip condition ($\mathbf{v} = \mathbf{0}$) is imposed everywhere in the fluid except for the output and the input. The outflow boundary condition is stress equal to zero weakly imposed. For the solid domain, the geometry is fixed everywhere except for the contact boundaries. The tolerances for the non-linear solvers and the coupling where set to 1E-6.

Results The CIQN algorithm is compared against the Aitken (atk) and a Broyden (brd) relaxation schemes. Coupling convergence for the different schemes is shown on Figure 4.15.

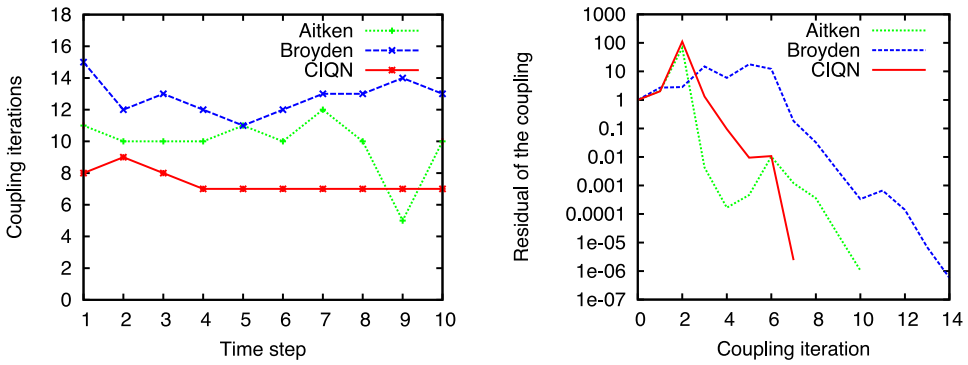

Figure 4.15: Typical convergence for the coupling. Left: number of coupling iterations for the first 10 time steps. Right: residue of the coupling for the first time step.

The algorithms are used to relax force and displacement separately, so there are two variations for each coupling scheme. Also two different numbers of saved iterations are tested for the CIQN algorithm. 100 time steps were computed with all the possible relaxation combinations. A first glance on the results is presented in Figure 4.16 were we show a snapshot of the solution and a plot of the accumulated[2] solver iterations.

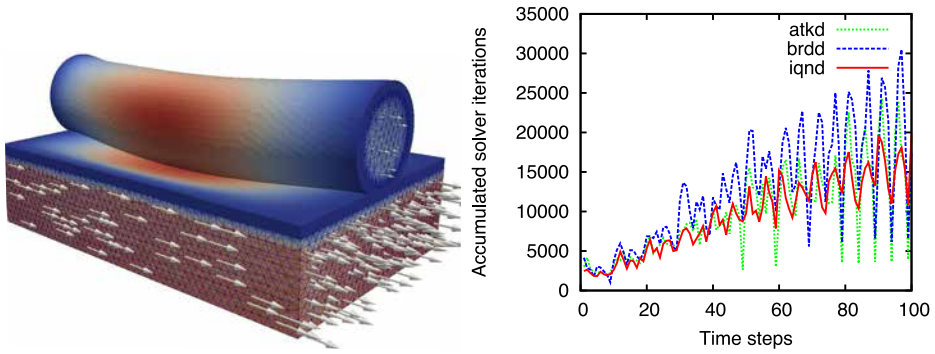

Figure 4.16: Biomedically inspired FSI case. Left: snapshot of the simulation at $t = 0.4$ $[s]$ for the biomechanical inspired case. Right: Accumulated solver iterations in each time step for the best variant in each algorithm family. The different acronyms stand for: atkd, Aitken relaxed in displacement; brdd, Broyden relaxed in displacement; iqnd, CIQN relaxed in displacement.

[2]Solid mechanics solver and fluid dynamics solver for momentum and continuity accumulated for each time step.

Table 4.1 summarizes the results for all the possible combinations: Aitken, Broyden and CIQN, relaxed in displacement and force (atkd, atkf, brdd, brdf, ciqnd, ciqnf). For CIQN we also show the effect in increasing the number of past iterations used (rank 5 and rank 20). For each coupling strategy we show the average coupling iterations, the computing time per time iteration (in [s]), the average subiterations per time step for the fluid (momentum and continuity) and the solid mechanics problems, and the average solver iteration per time step.

coup. strate.	coup. iter.	time x iter.	CFD subit	CFD sol ite	CSM subit	CSM sol ite
atk displ	9.36	16.70	18.70	2064.76/989.36	6.51	2513.36
atk force	9.52	16.27	20.88	2340.99/1078.36	5.99	2353.96
brd displ	12.16	16.31	18.50	2586.81/1271.28	6.53	3150.89
brd force	17.65	16.05	20.30	3565.25/1670.89	5.98	4488.76
iqnd r5	8.64	17.24	20.84	2040.46/961.70	6.72	2347.26
iqnd r20	8.66	17.37	20.81	2022.46/961.63	6.71	2375.82
iqnf r5	10.54	17.25	22.04	2715.19/1246.88	6.22	2724.44
iqnf r20	14.39	16.33	20.17	3605.16/1784.84	6.33	3496.33

Table 4.1: Biomedically inspired FSI case. Summary of the experiment. The different acronyms stand for: atk, Aitken family; brd, Broyden family; iqn, CIQN family. If the family name is followed by "displ" it is relaxing the Dirichlet variable; if it is followed by "force", it is relaxing the Neumann variable. In the iqn family, the number of past saved variables can be modified. In this case, five (r5) and twenty (r20) iterations were tested.

The four graphs in Figure 4.17 refine the information in the table. The iterations for all the tested schemes are detailed, aggregating the results by coupling scheme. Finally, a candle plot shows the distribution for the coupling iterations detailing the median and the interquartile range.

All the coupling schemes are capable to solve the system, with differences in the performance. For the best set up in each family, the CIQN algorithm required 8.5% less iterations compared with the Aitken algorithm and 30% less iterations if compared against the Broyden scheme. Regarding the processing time, CIQN performs 9% and 6% faster compared to Aitken and Broyden respectively.

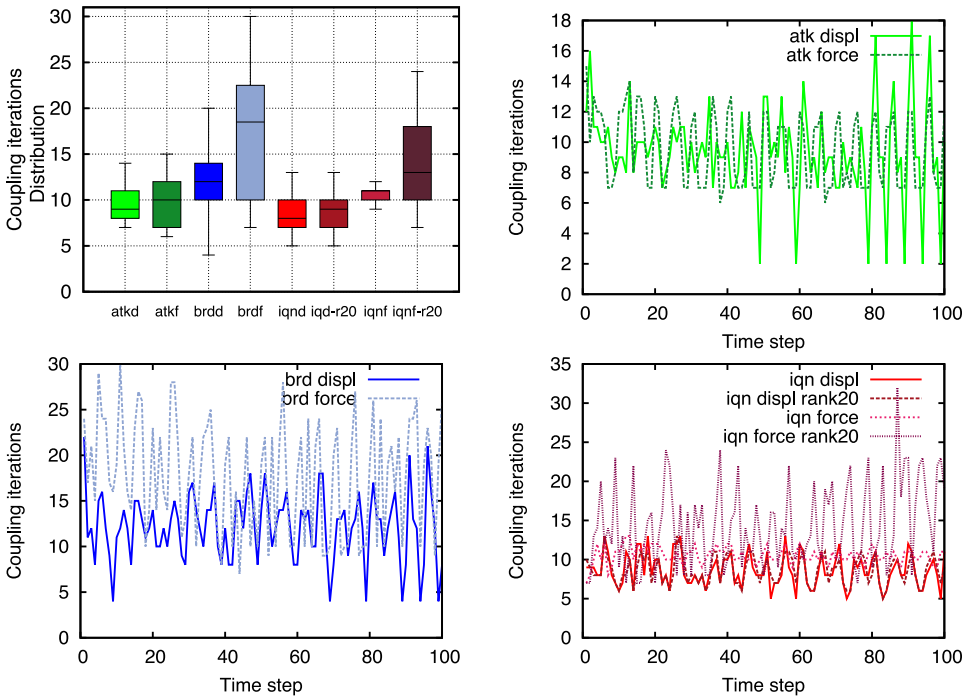

Figure 4.17: Biomedically inspired FSI case. Top left: coupling iteration distribution. For each candle the middle line represents the median, and the upper and lower lines the 25% and 75% percentiles. Top right: convergence for the Aitken family. Bottom left: convergence for the Broyden family. Bottom right: convergence for the CIQN family.

4.4 Parallel performance for the fluid-electro-mechanical model

As the developed model is designed to run in high performance computing (HPC) machines, is a requirement for our work to test the parallel performance of the coupled problem. The main reasons are:

- the high complexity of the models exposed in Sections 2.2 to 2.4.
- the complex numerical treatment required for the FSI problem shown in Section 3.5
- the fine mesh required to capture the details of the geometry described in Section 3.2 including the mandatory mesh requirements to truly capture the features of the O'Hara-Rudy model (fact proven in Section 4.1)

It is clear that such a problem cannot be solved without supercomputer resources, ranging from a few hundred to few thousand cores, depending on

the problem. As said in Section 2.1 all the models are programed in Alya and implemented in the way explained in Chapter 3. In this section we prove the high scalability of this code, a feature that even goes beyond the requirements of the problems presented in this thesis.

To test the parallel performance of the code, the geometry presented in Section 3.2 was uniformly refined using the algorithm described in [127]. Obtaining a ~ 70 and ~ 40 million elements for the solid and fluid domain respectively. All the cases have run in Marenostrum IV supercomputer. In a first stage, the parallel performance of each solver running independently (not coupled) is tested. Results are shown in Table 4.2 and Figure 4.18.

Core	CFD			CSM		
count	elem./core	S-U	eff.	elem./core	S-U	eff.
192	210k	192.00	1.00	365k	192.00	1.00
384	104k	384.00	1.00	182k	384.00	1.00
480	83k	480.00	1.00	146k	480.00	1.00
768	52k	768.00	1.00	91k	768.00	1.00
1536	26k	1489.92	0.97	46k	1520.64	0.99
1968	20k	1896.61	0.95	36k	1908.96	0.97
2400	16k	2256.02	0.94	30k	2315.28	0.96
2880	15k	2563.21	0.89	25k	2771.46	0.96
3840	11k	3275.13	0.85	18k	3615.74	0.94
4320	9k	3411.64	0.79	16k	3992.47	0.92
4800	8k	3713.68	0.77	14k	4426.08	0.92

Table 4.2: Massively parallel performance. Speed up and efficiency for the fluid dynamics computational fluid dynamics (CFD) and solid mechanics computational solid mechanics (CSM) solvers running separately.

Efficiencies about 80% and 90% were obtained for fluid mechanics and solid mechanics running up to 4800 cores for each one. The obtained curves separates form the ideal when the elements/core ratio falls under a certain value. This phenomenon occurs because the time invested in the communication between Message Passing Interface (MPI) threads becomes comparable to the computing time. As the communication process is slow, if it is compared against the computation time in each core, the scalability drops.

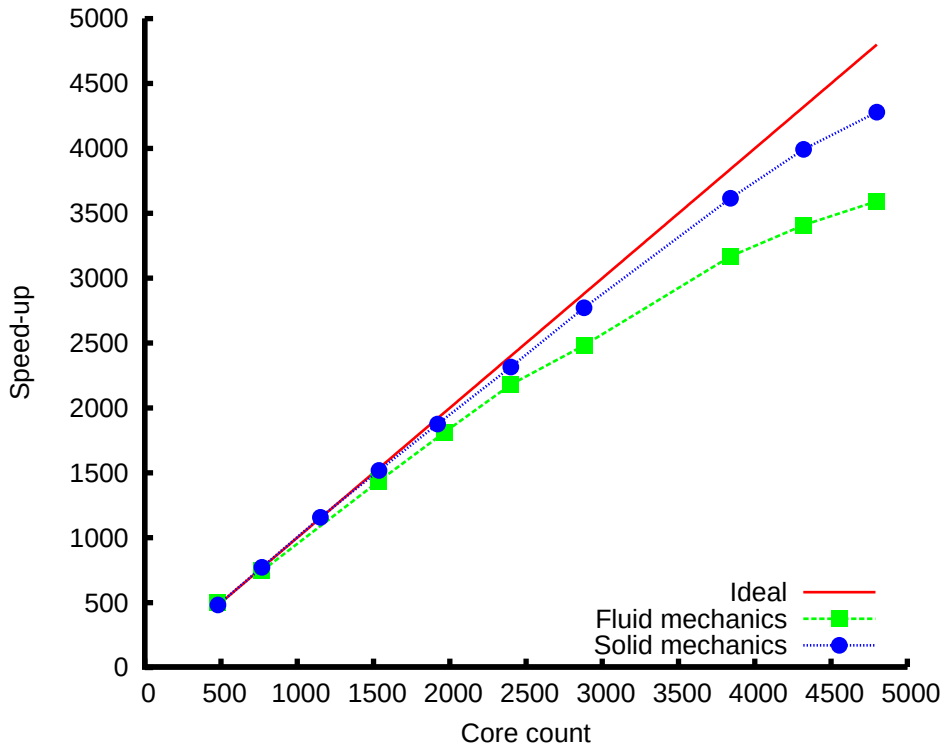

Figure 4.18: Massively parallel performance. Speed up and efficiency for the CFD and CSM solvers running separately.

In this thesis, the FSI coupling is solved using the Gauss-Seidel approach, where each parallel solver (fluid and structure) run in a block manner, one after the other (see left side of Algorithm 1). This causes one of the threads to wait while the other is computing. For better understanding refer to the schematic trace in Figure 3.9, or to the experimental trace in figure Figure 4.19. In Figure 4.19, p_s and p_f are the number of cores for the solid and fluid problems respectively; Ini is the initialization process; S_{solve} and F_{solve} are the solving time for the solid and fluid mechanics; S_{wait} and F_{wait} the waiting time for the solid and fluid mechanics respectively and Cou the coupling iterations.

The execution in Figure 4.19 uses the same number of cores for each problem ($p_f = p_s = 48$), resulting in a very inefficient run, as the cores computing the fluid have to wait for the solid solver results. In multi-code executions, the $p_f - p_s$ core assignation have to be tuned to optimize the execution efficiency. To obtain this optimum point, a core allocation swipe is done. To do so, we fix the number of cores for one problem (In this case p_s), and then swipe the number of cores in the other problem (p_f). If efficiency is computed for each execution, the optimal point $p_f - p_s$ can be found.

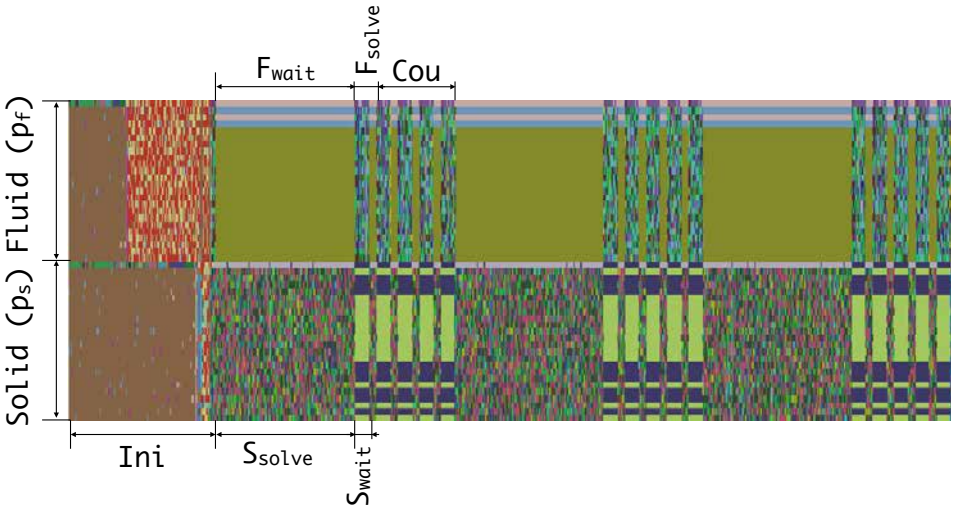

Figure 4.19: Massively parallel performance. Trace for three iterations of a coupled problem. The same number of cores (p_f and p_s) were assigned the parallel solvers. First, there is an initialization stage (Ini). The solid solver executes (S_{solve}) while the fluid solver waits for the results (F_{wait}), then the fluid portion is computed (F_{solve}) while the solid thread waits (S_{wait}). Once solved both, the coupling iterations (Cou) start to converge the wet surface. Three complete time steps are shown.

Figure 4.20 shows speed-up and efficiency for four fixed values in the fluid solver core count p_f. In each case the core count for the solid mechanic solver p_s is ranged between 64 and 2048, with increments in power of two. These processes is performed for a core count of 256, 512, 1024, and 2048 in the fluid solver. For each speed-up curve, a maximum in the efficiency can be achieved. These maximum values of efficiency indicate the number of cores that should be assigned in order to attain an optimum execution time for a specific configuration of the Gauss-Seidel scheme.

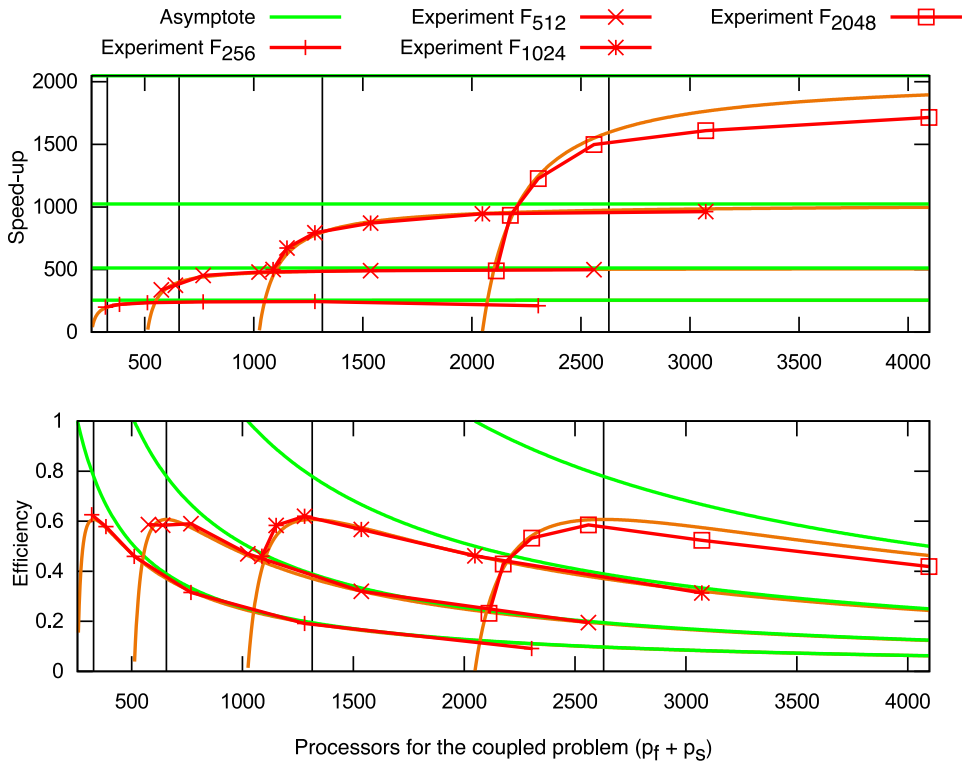

Figure 4.20: Parallel performance analysis. Speed-up and Efficiency for a core allocation of $p = p_f + p_s$, where $p_f = \{256, 512, 1024, 2048\}$ in the core count for the fluid, and $p_s = \{64, 128, 256, 512, 1024, 2048\}$ for the solid. An optimal allocation p_{opt} which allows to achieve the maximum efficiency E_{p_f} of the coupled system can be found for each curve S_{p_f}.

Chapter 5

Fluid-electro-mechanical simulations in a whole-heart geometry

Marenostrum happens to be one of the finest 'modelling' computers on earth, specializing in complex simulations, its most famous being 'Alya Red' –a fully functioning, virtual human heart that is accurate down to the cellular level.

Winston to Prof. Robert Langdon
Extracted from Origin,
a novel by Dan Brown

Summary:

In this chapter, the whole heart human geometry is used to simulate all the physics involved in the heartbeat: electrophysiology, solid mechanics and fluid dynamics. First, the model is used to simulate a healthy heart systole. These results are deeply analyzed and compared against experimental measurements taken from the bibliography. This healthy heart simulation also works as a baseline for the following experiments, where the computational heart is diseased. In the first pathologic situation, a left bundle branch block is modeled in the computational heart. After that, it is treated with cardiac resynchronization therapy. In the second pathologic case, a third degree atrioventricular block is modeled in the computational heart. To treat the disease, an intracavitary leadless pacemaker is implanted and the interaction between the device and the surrounding tissues is modelled. Finally, In the last pages of this chapter, we present a scalability test for the three-physics coupled model.

5.1 Computational scenario

In this chapter, all the simulations are run with the fluid-electro-mechanical model in the whole heart geometrical description. As a reminder, the human cell model of O'hara-Rudy [29] is used for electrophysiology (see Section 3.3.1), with the parameters proposed in [26]. The solid mechanics have been modelled with the Holtzapfel-Ogden [39] formulation and parameters, bidirectionally coupled with electrophysiology by the Hunter-McCulloch [76] scheme (refer to Section 3.3.2). Fluid dynamics have been solved using the Navier-Stokes equations with an arbitrary Lagrangian-Eulerian (ALE) framework, previously described in Section 3.4.1. The Fluid-Structure Interaction (FSI) problem is solved using the Compact interface quasi-Newton (CIQN) technique developed in Section 3.5.

The whole-heart geometry used, is presented in Section 3.2.1. It is composed by ventricles, atrium and great vessels. The ventricles are the only contractile structure, while the rest of the tissue is passively deformed. Cubic fibres are created with the Streeter rule-based method. For the electrical depolarization, both endocardium surfaces are depolarized at the same time, except specified otherwise. In the computational solid mechanics (CSM), the sliding pericardium boundary condition is used in the ventricles, and the force computed by the computational fluid dynamics (CFD) is imposed in the endocardium surface. CFD is solved with the ALE formulation. No slip boundary condition is imposed everywhere except for the outputs, where the stabilized outflow condition Equation (3.44) is used.

The simulation starts with the depolarization of the endocardium, with the aortic and pulmonar valves open, and finishes when the net ventricular outflow drops to zero. The Wiggers diagram in Figure 5.1 shows the simulation time frame.

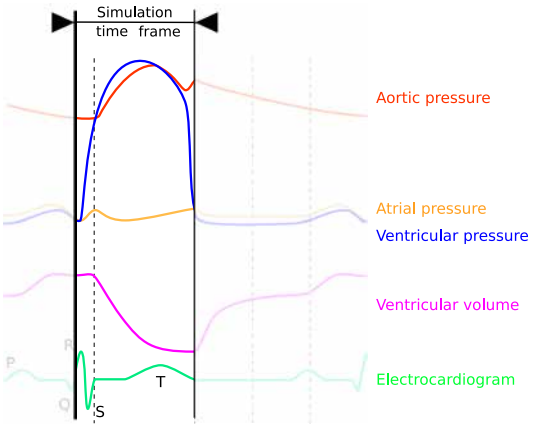

Figure 5.1: Computational scenario. Wiggers diagram (see Section 1.2.3) for a healthy heart systole showing the simulation time frame.

As only systole for one heartbeat is simulated, we may be visualizing transient state results. To obtain a steady state solution, hundred of complete (systole-diastole) heartbeats should be computed. Despite this, the cases proposed aim to analyse instantaneous depolarization voltages, deformations and velocities. Long term (minutes) effects produced by flow or pressure, or closed circuit volume balance are out of the scope of this thesis.

The problem is computed using the multi-code strategy described in Section 3.1.2. One Alya instance computes electrophysiology and CSM and the other Alya instance solves CFD with the ALE formulation. The solid domain mesh has $2M$ tetrahedra and $500k$ nodes. The fluid domain mesh has $1.2M$ tetrahedra and $300k$ nodes. All the cases run in Marenostrum IV supercomputing using 5 nodes composed by 48 cores each, giving a total of 240 cores. 192 cores are used for the electrophysiology and CSM and 48 cores for the CFD problem (load balance is discussed in Section 4.4). Each run takes a mean time of $\sim$ 10 hours, with a slight variability depending each case.

5.2 Analysis of a healthy systole

In this section, we model a healthy systole. By "healthy" we mean that all the framework previously described is used and no pathological condition is purposely introduced. This first heart simulation is deeply analyzed and used as a baseline comparison for the experiments in other sections this chapter.

5.2.1 Description

The three physics fluid-electro-mechanical model is solved in the whole heart geometry presented in Section 3.2. Also, all the models and boundary conditions previously tested are used. This includes the sliding pericardium boundary condition and a cubic fibre distribution. Also, the electrophysiology model is stimulated by depolarizing both endocardial surfaces synchronously.

5.2.2 Results

In the following images a detailed analysis of the fluid-electro-mechanical simulation in the whole heart geometry is shown. Results are presented in the following way. First, we give an overall view in the healthy heart dynamics. Then, we separate the results for the analysis, first the CSM and after the CFD. In Figure 5.2 we show image sequence including myocardium contraction and the ventricles interior fluid dynamics, where an overall view of the simulation is depicted.

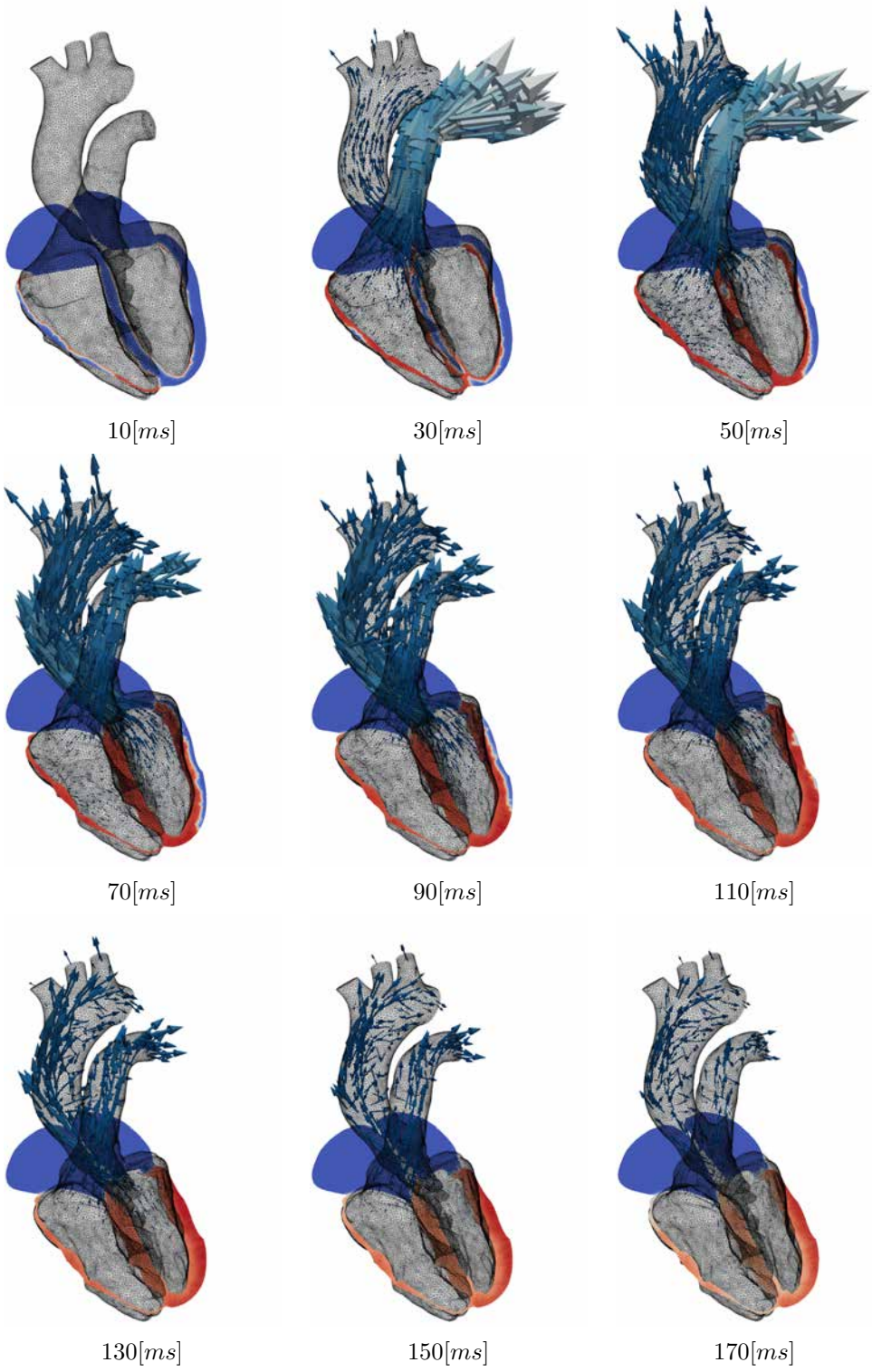

Figure 5.2: Analysis of an healthy systole. Simulation snapshots. The deforming slice in the myocardium shows a long axis view, coloured by electrical depolarization. The arrows in the fluid domain shows the velocity field.

In Figure 5.2 the overall behavior of the simulation is shown. The slice represents the four chamber view, where the myocardium depolarization can be observed. The electrical stimulus starts in the endocardial surface, and propagates mainly to the epicardium. In the fluid domain, velocities and pressure are computed for every time step. The arrows represent the velocity and are scaled with the module. It can be seen that the main fluid features occur in the outflow vessels rather than in the intracavitary space. Despite the relatively large endocardial displacements, there are small intraventricular velocities due to the relatively large size of the cavities. On the contrary, the smaller transversal area in the outflow vessels induces higher velocity profiles. Results for fluid dynamics are further analyzed below.

Myocardium behavior Figure 5.3 shows deformation for basal, medial and apical slices.

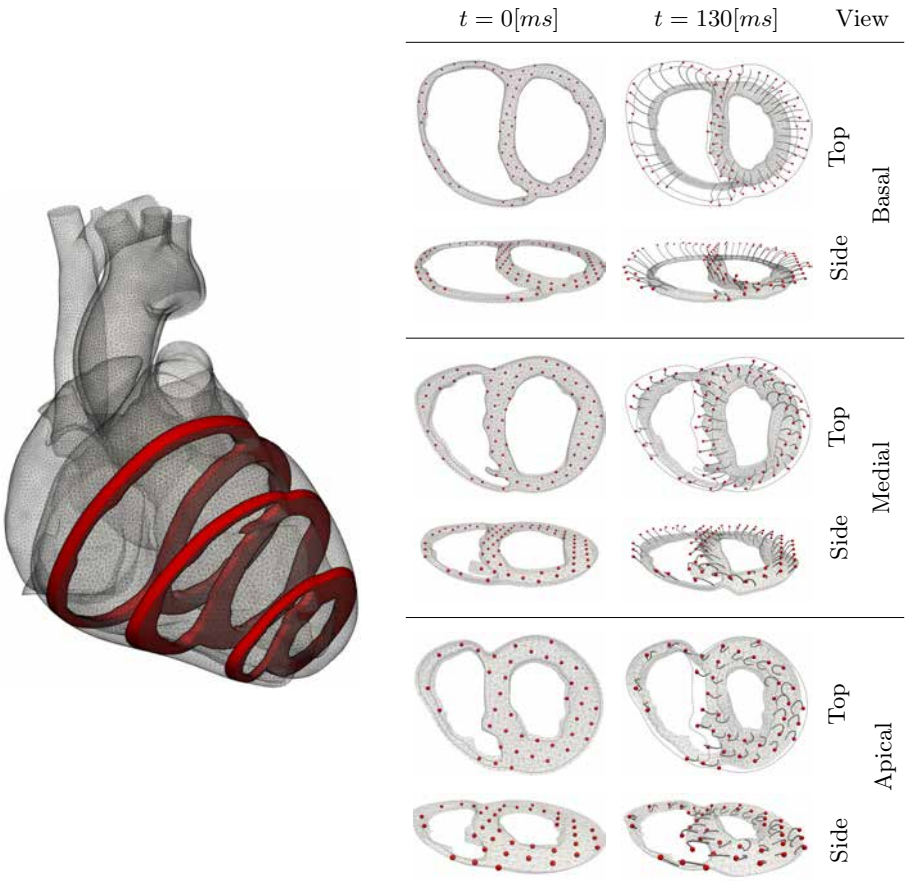

Figure 5.3: Simulation of a healthy systole. Material point tracking in the myocardium. The left side shows the position for the basal, medial and apical slices. In the right, top and side views for the slices.

The slices of the myocardium are shown together with material points in this domain, and the temporal pathlines for this particles. This way of tracking the myocardium movement is similar to tagged Magnetic Resonance Imaging (MRI) or speckle tracking echocardiography. Left side of Figure 5.3 shows the positions of the slices. In the right side, the slices and the material points are shown at $t = 0[ms]$ and $t = 130[ms]$. The red dots indicate the original position ($t = 0[ms]$) of the material points. The pathlines show the trajectory for each point during the time interval. If the apex-base direction is analyzed, we observe that the base moves in the base-apex direction, while the apex has barely no longitudinal displacement. The pathlines in the orthogonal plane show rotation of the apical region. These observations were seen in the numerical experiments in Section 4.2.2, and are experimentally confirmed by speckle tracking techniques [19, 138, 133] and by tagged MRI [139, 140].

Fluid dynamics domain behavior Figure 5.4 shows the deformation of the mesh in both ventricles, together with a plot of the ventricular volume.

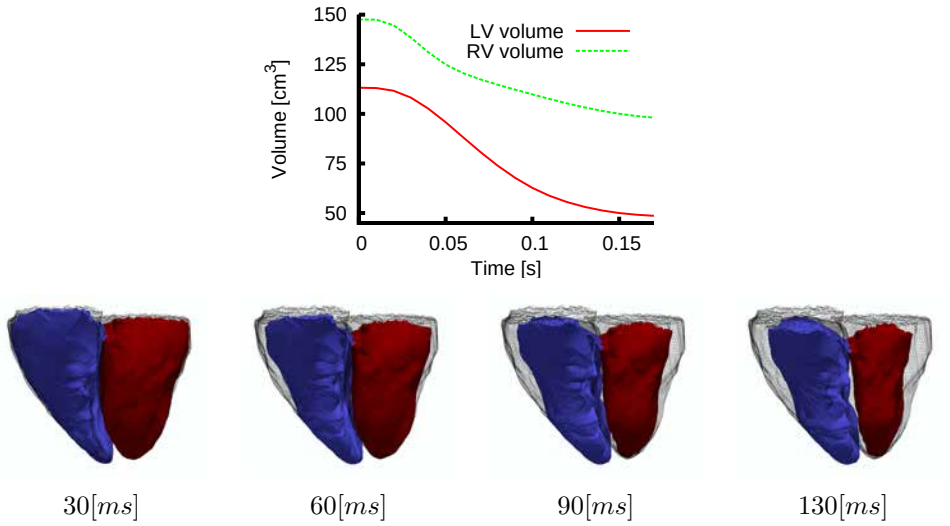

Figure 5.4: Simulation of a healthy systole. Ventricular volumes. Top plot shows the ventricular volume as a function of time. The image sequence shows the deformation of the ventricles.

After taking measures, the end diastolic volumes (EDVs) [1], end systolic volumes (ESVs) [2] and ejection fraction (EF) for the left ventricle (LV) and right ventricle (RV) are shown in Table 5.1. Although these values are slightly deviated from statistical measurements (EDV $\sim 150[cm^3]$ for each

[1] Volumes of the cavities in diastole, measured at $t = 0[s]$.
[2] Volumes of the cavities at maximum contraction, measured at $t = 130[s]$.

ventricle [141, 49, 142]), we attribute the error to the modifications done in the original geometry (see Section 3.2).

	EDV $[cm^3]$	ESV $[cm^3]$	EF
LV	113.16	49.12	56 %
RV	147.58	97.43	35%

Table 5.1: EDVs, ESVs and EF for the LV and RV for the healthy heart simulation.

In Figure 5.5 outflow curves for the RV and LV in the simulation are compared against experimental measurements flows [143]. In the cited work, from MRI images the authors measure LV output and then compute CFD simulations from ventricular deformation.

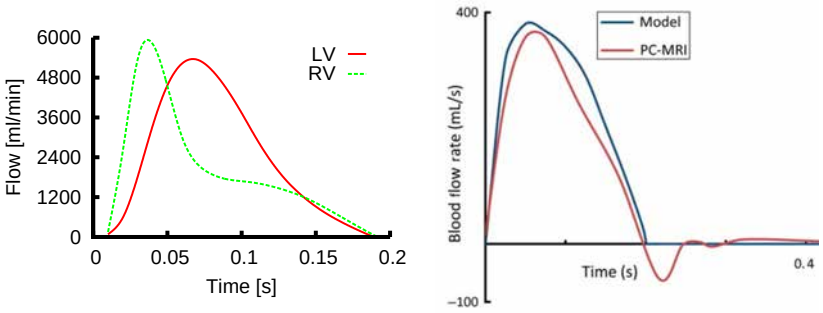

Figure 5.5: Analysis of a healthy systole. Left: Simulation results for the LV and RV outflows. Right: experimental/modelling curves taken from [143]. the PC-MRI curve is the experimental measurement taken using MRI. The model curve is the numerical result obtained by the cited authors.

Due to the synchronous depolarization of both endocardial surfaces, the thin wall of the RV, and the orthotropic conduction speed, the RV is fully depolarized before the LV. This disparity, induces a $5[ms]$ difference between the peak of the LV and RV outflows. This effect can be tackled if an activation protocol as the proposed in [66] is used, where the RV is depolarized with a 25[ms] delay. Despite this, results are qualitatively comparable with human measurements [144, 143]).

In Figures 5.6 and 5.7 we analyze the intracavitary fluid dynamics through Q-criterion[145, 146] isosurfaces (at 5000 and 50 $[s^2]$ respectively). The deformable slice in the solid domain represent a long axis view of the myocardium. The colour in that represents the electrical depolarization. Q-criterion isosurfaces in the fluid domain are coloured by velocity magnitude.

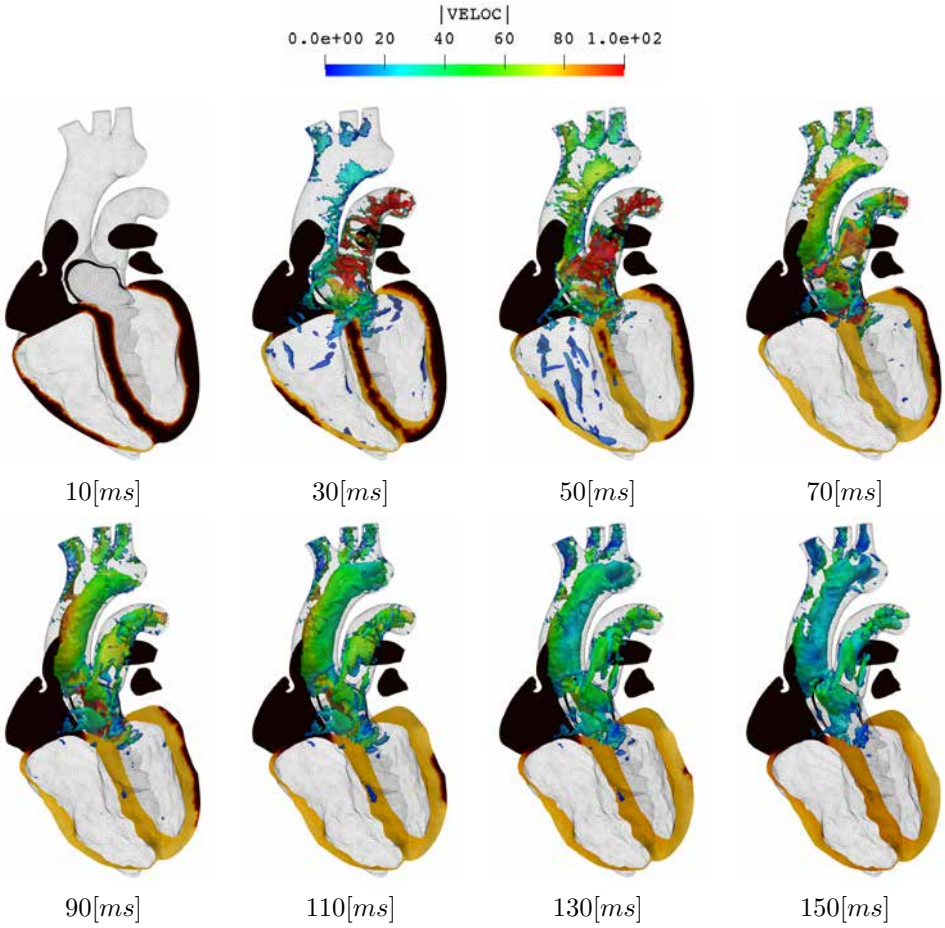

Figure 5.6: Analysis of a healthy systole. Image sequence showing a four-chamber slice in the myocardium and Q-criterion isosurfaces (value of $5000[s^{-2}]$) for the fluid dynamics domain. The isosurfaces are colored by velocity module.

Figures 5.6 and 5.7 show a slice of the myocardium, The isosurfaces are coloured by velocity module. Q-criterion allows to visualize vortex formation. The difference between Figure 5.6 and Figure 5.7 is the threshold value for the Q-criterion isosurfaces. When the whole-heart window is used (isosurfaces at 5000 $[s^{-2}]$) we are able to see vortex with higher speeds. When the ventricular window is used for the Q-criterion (isosurfaces at 50 $[s^{-2}]$), we are able to see smaller vortices. As expected, the main features in the flow occur in the outflow vessels rather than in the ventricular space as a consequence of the higher speeds. Despite this, there is more complex vortex structure in the ventricular region, even though they have smaller velocities.

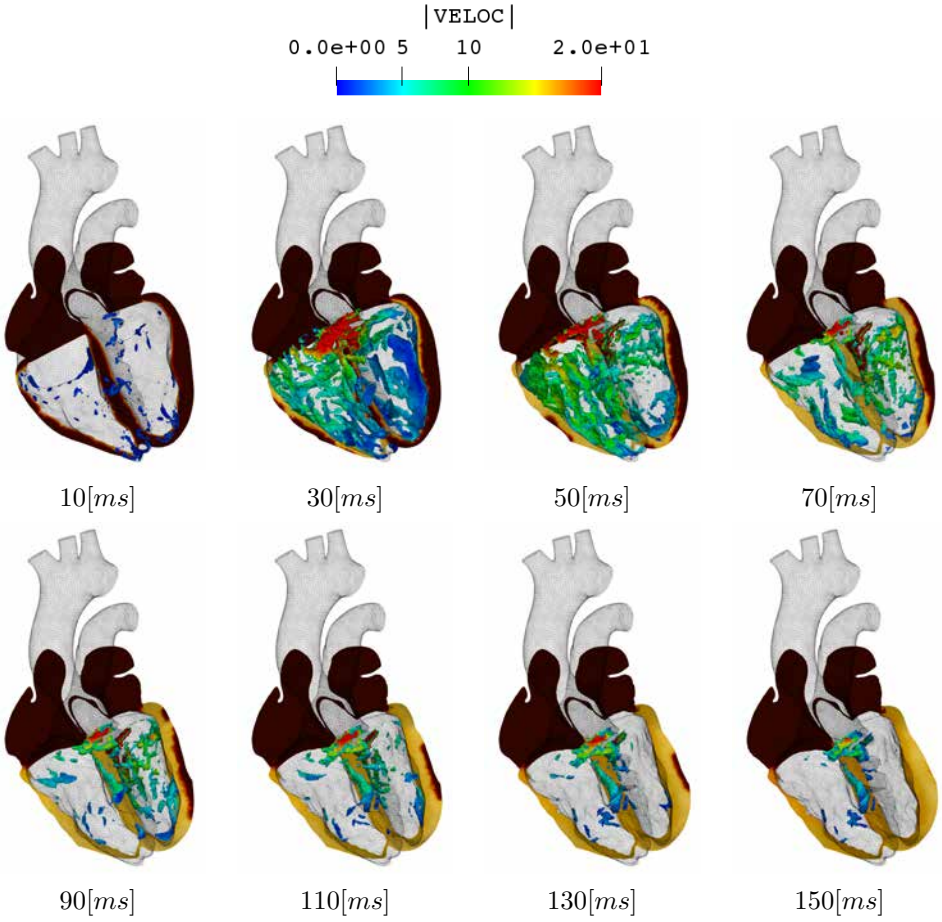

Figure 5.7: Analysis of a healthy systole. Image sequence similar to Figure 5.6 but using Q-criterion isosurfaces at $50[s^{-2}]$. Please that the scale of the velocity module goes up to $20[cm/s]$.

For better understanding of the intraventricular fluid dynamics features, in Figure 5.8 we show a view for the ventricular depolarization, displacements and intracavitary fluid dynamics. Figure 5.8 shows a slight desynchronization between the right and left side, feature also seen in Figure 5.5. In the slices of the solid domain, it can be seen how the endocardium is depolarized and this wave front travels mainly to the epicardial region. As the right ventricle is considerably thiner than the left ventricle, it is depolarized earlier. However, there is a net outwards flow condition in the ventricular region. In Figures 5.9 and 5.10 we focus in the apex and the aortic root respectively. The glyphs in this figures are scaled to the maximum velocity in the studied domain. The flow patterns in the apical regions show velocities in the apex-base direction. In the early stage some flow occurs from base to apex due to the basal displacement.

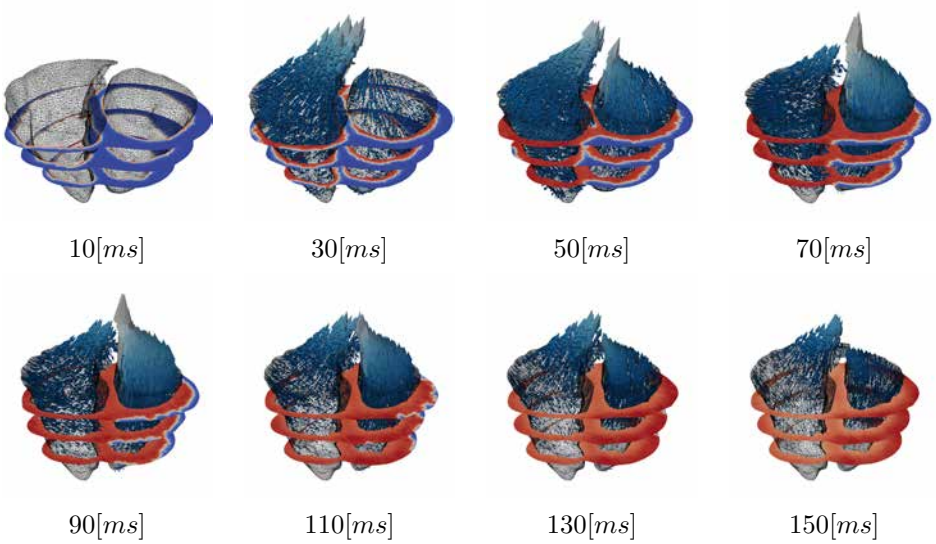

Figure 5.8: Analysis of a healthy systole. Detail of the ventricular electrical depolarization, deformation and fluid dynamics.

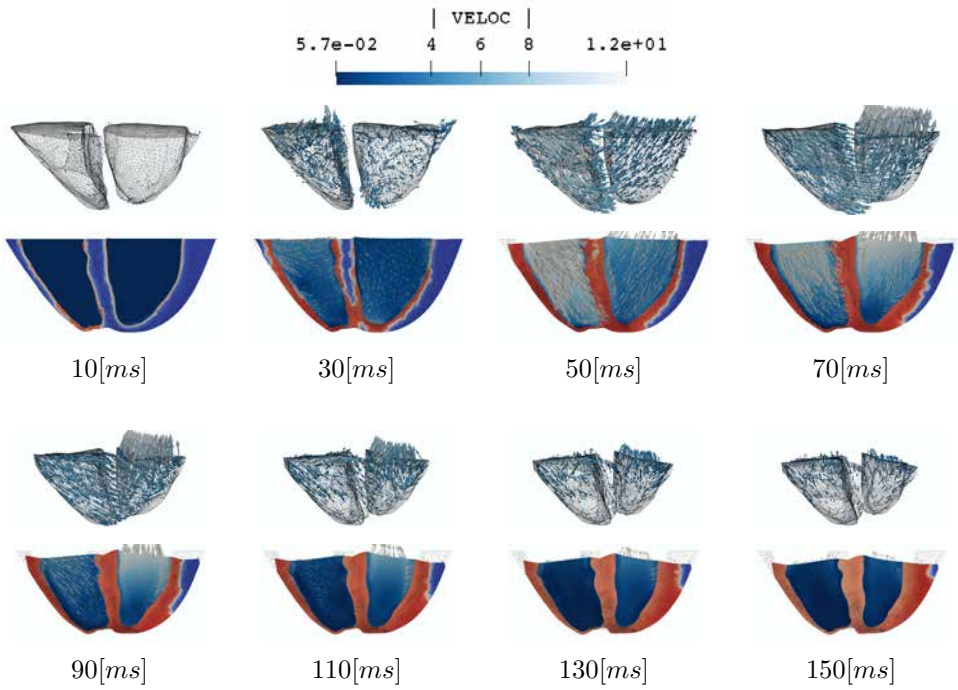

Figure 5.9: Simulation of a healthy heart. Detail of the apical region. The upper row shows the fluid mesh, and velocity arrows. The lower row shows a slice of the geometry, plotting electrical field in the solid domain and velocity in the fluid domain.

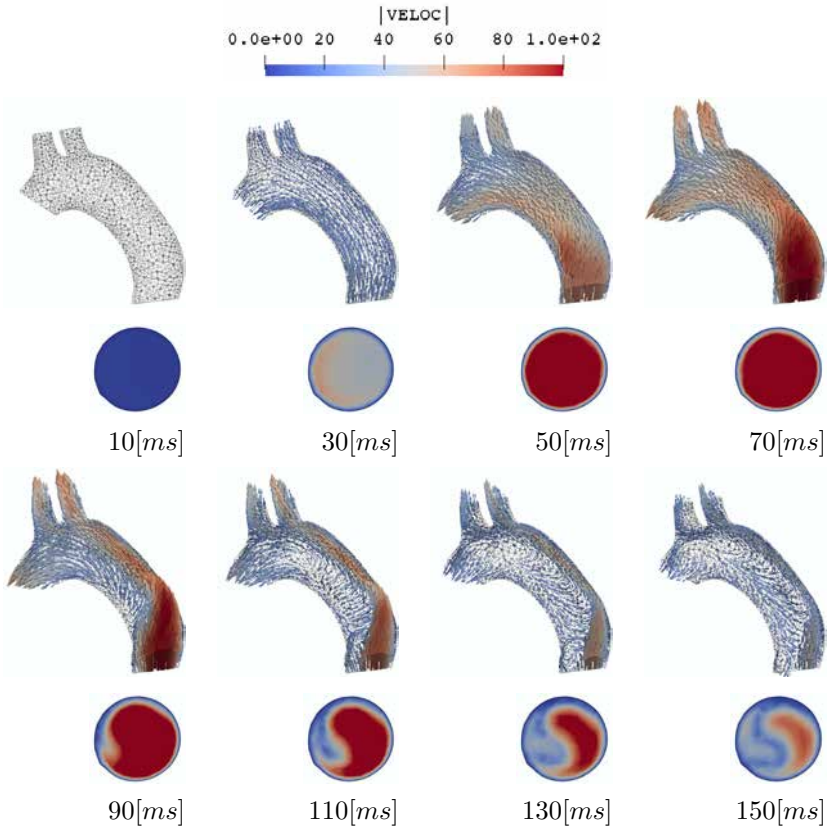

Figure 5.10: Analysis of a healthy systole. Image sequence for the aorta showing the co-planar aortic arch output, the brachiocephalic output and the left common carotid artery output. Arrows and colors represents velocity. A short axis view for the aortic root is also shown. In this last view the helical pattern in the aortic root is clearly seen.

The ventricular fluid dynamics (in Figures 5.8 and 5.9) features a fairly uniform and laminar flow, with maximum velocities of $9.8[cm/s]$. On the contrary, flow in Figure 5.10 features a more active pattern, with maximum punctual speeds above $80[cm/s]$ (comparable with the $\sim 100[cm/s]$ obtained with MRI measurements by [147]), with larger transversal gradients, and a slight backflow despite the net outflow condition. The aortic root section in Figure 5.10 shows an non-symetric flow, with a velocity pattern diverted to the lateral part of the aortic root. This flow pattern is also seen in experimental measurements [148, 149]. A similar study for the aortic root, comparing different imaging techniques with simulation results can be found in [150]. To finish the analysis for the healthy systole, in Figure 5.11 we compare a 4D flow MRI image [151] taken from [152] with the simulation results. Both figures show velocity pathlines, despite the chosen color scales are different. A high qualitative resemblance can be seen.

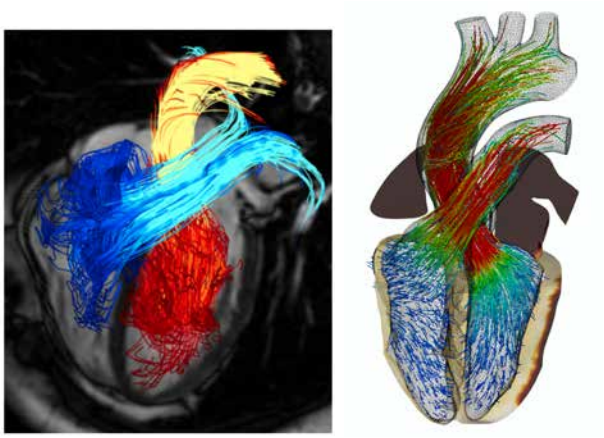

Figure 5.11: Simulation of a healthy systole. Left: MRI 4D flow image taken from [152]. Right: simulation results with the whole heart model.

To conclude, in this section we show that the results for the whole-heart fluid-electro-mechanical simulation model under normal conditions, at least for the systole, are similar to the experimental measurements, with a physiological behavior in most regions. This detailed analysis of the results also define a baseline for the following numerical experiments, where pathological conditions are modelled.

5.3 Clinical application I: left bundle branch block

In this section we induce a pathological condition in the heart model presented in the previous section. First, a left bundle branch block (LBBB) [153, 154] is simulated. In this pathology, a faulty conduction system produces dyssynchronous contraction of the ventricles. After, we treat the diseased heart with cardiac resynchronization therapy (CRT) [155, 156, 157, 158, 159, 160].

We choose left bundle branch block (LBBB) as the first test case for our healthy heart because it is a well known pathology and it is often used as an example by the simulation community [5, 161, 162, 53, 163, 164]. However, it is worth to remark that, this pathology and the cardiac resynchronization therapy (CRT) treatment are being simulated for the first time in a fluid-electro-mechanical model in this work. The main goal of this simulation is to prove that the computational model of the heart, can be used to model a LBBB and a CRT, with results that resemble the physiological behavior. This goal, can be decomposed in two:

- Confirm that the clinical signs observed in patients affected by LBBB are also reflected in our simulation.

- Confirm that the CRT restores the cardiac function in the computational heart affected with LBBB.

5.3.1 Background and description

Pathology description LBBB, can be induced by a wide range of etiologies like drug overdose, myocardial infarction [165, 166, 167], degenerative diseases or infectious causes [168] among others. In this pathology, there is faulty conduction from the atrioventricular (AV) node (see Section 1.2.1 for a reference) to the LV. Despite this, the RV is normally depolarized. The depolarization of the LV is induced by the wave front originated in the RV. This condition produces a dyssynchronous beating of the heart and a dramatical reduction of the EF.

Treating the pathology This condition can be treated by CRT [169]. In this technique, a pacemaker is used to resynchronize the depolarization of the heart. To do so, the electrical activity is measured in the right side, and the LV is activated after a delay from the first measure. In the classical approach, a pacemaker lead is guided through the great vessels, up to the aortic sinus. After, the tip of the lead is positioned in an specific spot in the LV epicardium. The final location of the lead depends on the coronary branches of the patient being treated, and the decision of the interventionist. After the lead is positioned, the stimuli has to be synchronized to obtain the mutual depolarization of both ventricles. To do so, the pacemaker measures electrical activity in the right side and delays the LV stimuli from that measure as temporal reference.

Modelling the case In this section we model a LBBB and then we treat it with CRT. The same setup for the healthy heart experiment is used here, except for the electrical depolarization sequence. To model LBBB, we eliminate the initial stimuli in the left endocardium, "blocking" the left branch of the conduction system. As a consequence, the LV is only depolarized due to the electrical wave coming from the right side of the heart. When LBBB is treated by CRT, the pacemaker lead's tip is guided through the coronary arteries and placed as close as possible to the optimal spot in the epicardium. In this experiment we choose the mid anterolateral region as a generic pacing spot. The LV depolarization is triggered a Δt_d time after the RV electrical activity. Cardiac output is evaluated an analysis in the CFD domain.

5.3.2 Results

In this section we show the results for the experiment. First the LBBB case is shown. Then, we show results for the diseased heart treated with CRT.

Base pathology: LBBB Figure 5.12 shows snapshots for the LBBB case.

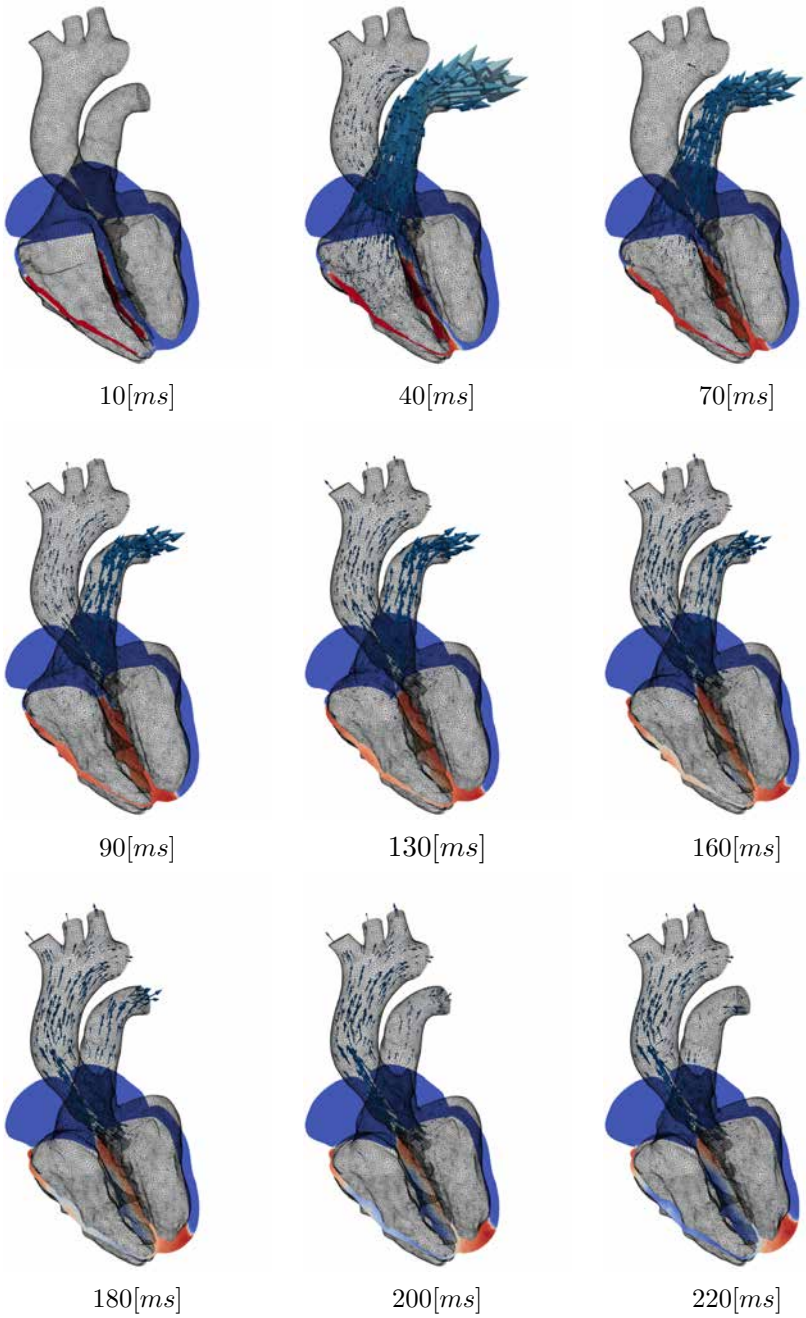

Figure 5.12: LBBB. The slice in the myocardium shows that the RV is depolarized first, and the LV is depolarized due to the wave coming from the RV. This dyssynchrony reduces the cardiac output.

In order to ease comparison, the plots for the healthy case, the pathologic condition and the CRT simulations are shown ahead in Figure 5.14.

As there is no depolarization of the LV by the left Purkinje network, this is depolarized by the wave coming from the RV, inducing a severe dyssynchronization in the depolarization and contraction of both ventricles. Consequently the depolarization time is doubled, and a reduction in the outflow of both ventricles. The delay in the depolarization of the ventricles is a clinical sign also reflected in the Electrocardiography (ECG) of patients with such condition [153]. The present pathology diminishes the ventricular outflow a $\sim 60\%$ for the LV and $\sim 30\%$ for the RV. Despite the impact of LBBB is very patient dependent [155, 156], it is accepted that the LBBB not only affects the LV function, but also the RV function. Figure 5.13 shows a basal slice with material points tracking. Note that if this figure is compared

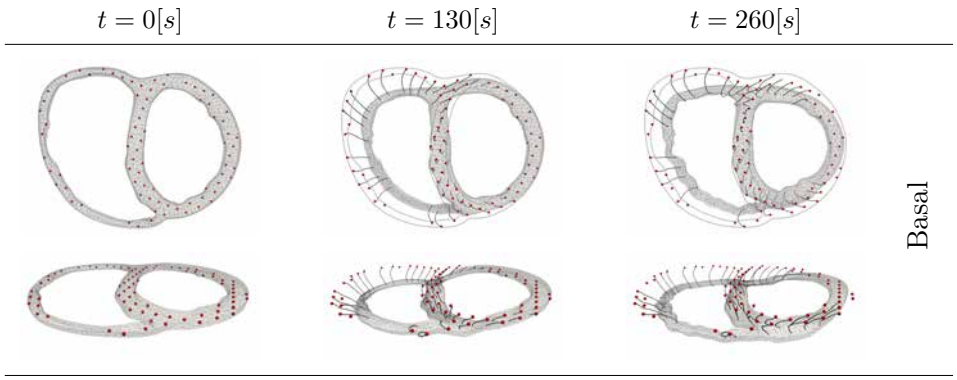

Figure 5.13: LBBB. Basal slice with material points and pathlines. The figure shows the dyssynchrony of the RV and LV.

against the healthy heart (see Figure 5.3), a great delay in the LV can be seen.

Treating LBBB with CRT CRT is modeled depolarizing the left ventricle in the mid-anterolateral region at $\Delta t_d = (-10, -40, -80)[ms]$ before the RV depolarization [170]. In Figure 5.14.A we show total normalized depolarization for the healthy heart, the LBBB heart, and for the different synchronization timings for the CRT. In Figure 5.14.B RV and LV outflows are shown for the same experiments. In order to ease comparison, all plots and image sequences are shown synchronizing the depolarization of the RV. Figure 5.14.C shows electrophysiology only results for the LBBB and the different CRT simulations.

Figure 5.14.A shows a severely delayed total depolarization for the LBBB case, compared against the healthy case. Figure 5.14.B shows that the modeled pathology affects both LV and RV outflows, with a higher impact

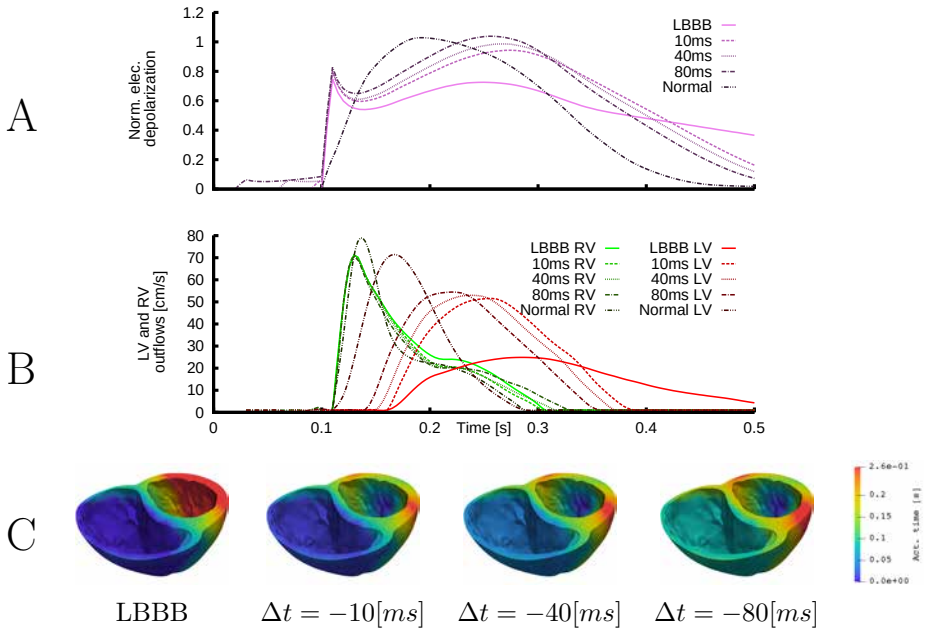

Figure 5.14: CRT for LBBB. The normalized electrical depolarization (plot A) and ventricular outflow (plot B) is shown for the healthy heartbeat, the LBBB case and the different CRT timings. Outflows for both chambers are also shown. snapshots in plot C shows electrical activation times for the pathological case (LBBB) and the three resynchronization cases.

in the latter. The treated cases are also shown in Figure 5.14. Once the heart is treated with CRT, a significant improvement can be seen, even with a suboptimal timing for the pacing. Even for the worst case scenario simulated ($\Delta t_d = 10[ms]$), there is a considerable improvement in the LV outflow that rises from $\sim$ 30% to $\sim$ 70% of the normal values. Table 5.2 summarizes the results for the CRT applied to the LBBB case. The healthy and the pathological values are also transcribed to ease comparison.

Case	depol. time	LV-EF	LV-ESV	RV-EF	RV-ESV
Healthy	120 [ms]	56 %	49 $[cm^3]$	35 %	103 $[cm^3]$
LBBB	400 [ms]	19 %	91 $[cm^3]$	30 %	103 $[cm^3]$
CRT10	250 [ms]	40 %	67 $[cm^3]$	30 %	103 $[cm^3]$
CRT40	230 [ms]	42 %	65 $[cm^3]$	30 %	103 $[cm^3]$
CRT80	230 [ms]	44 %	63 $[cm^3]$	30 %	103 $[cm^3]$

Table 5.2: CRT for LBBB. Depolarization time, EF for the LV and RV and ESV for both ventricles is shown.

In this table is easy to see the effect of the CRT. The depolarization time is not only reduced, but the EF is increased almost to the reference values. Also reverse remodeling is seen, as the ESV decrease with the application of CRT.

The classical approach of studying CRT using electrophysiology only simulations, is shown in Figure 5.14.C. Despite this approach reflects the severe dyssynchrony produced by the LBBB and how CRT resynchronizes the heart, it fails in reflecting how the treatment improves cardiac output.

To conclude, with this experiment we show that the heart model presented is able to model a pathological condition such as a LBBB reflecting clinical signs also seen in practice. In the same way, treating the diseased heart with CRT improved cardiac output. This improvement is obtained even with suboptimal timing in the stimulation. The electrophysiological curves or the electrical activation patterns shown in Figure 5.14 would also allow us to study LBBB and CRT. Despite this, adding the mechanical deformation and the FSI formulation not only makes the problem more physiologically accurate, but also allows to quantify changes in the heart performance.

It is important to remark that both catheter position [171, 172, 173] and timing optimization [174, 175] have a great impact in CRT to achieve normalization of the ventricular parameters. In this thesis we fix the catheter position while measuring the treatment sensitivity to the pacemaker timing, leaving for a future work a more thorough sensitivity analysis.

5.4 Clinical application II: leadless pacemaker

In this section, we treat a third degree AV block modelled in the computational heart. In this pathology, none of the impulses produced upstream are conducted to the ventricles. The diseased heart is treated with a leadless pacemaker implanted in the RV apical region. This device acts as a foreign body interacting with the surrounding tissues. Due to this, the interaction with the muscle and the blood have to be solved. The main objective of this experiment is to show how the cardiac simulator presented can be used as a workbench for design and simulation of biomedical devices. To achieve this goal, specific objectives are proposed:

- Simulate the heart beating due to the leadless pacemaker.

- Analyze the interaction between the device, the cardiac muscle and the blood flow.

5.4.1 Background and description of the case

Pathology and treatment In a third grade AV block, none of the atrial impulses are conducted to the ventricles as a consequence of a disruption in the conducting system. Therefore, complete dissociation of the atrial and ventricular activity exists [176]. With this, the ventricles beat at the Purkinje network depolarization frequency, completely independent from the atrium depolarization. On ECG, AV block is represented by QRS complexes being conducted at their own rate and totally independent of the P waves (see Figure 1.3 for a graphical reference of a normal ECG). Patients with complete heart block are frequently hemodynamically unstable, and as a result, they may experience syncope, hypotension, cardiovascular collapse, or death. Pacemaker implantation together with pharmacologic therapy is indicated when there is an irreversible AV block. When single-chamber ventricular demand pacing (VVI[3]) is used, a novel type of minimally invasive device can be implanted, instead of the conventional leaded pacemaker. These leadless pacemakers [177] are inserted through femoral venous catheterization in the right ventricle endocardium, without any other type of incision.

Here, we use the heart model as a design guide for a leadless intracardiac pacing system, like the Medtronic Micra, or the St. Jude Nanostim (see Figure 5.15).

Medtronic micra St. Jude nanostim

Figure 5.15: Leadless pacemakers. Left: Medtronic's Micra and St. Jude's nanostim leadles pacemakers. Both devices are implanted in the RV using different anchoring strategies.

These novel type of pacemakers are gaining attention due to the reduced invasiveness during the implantation, if compared against a

[3]Treatment with pacemakers can be classified with three letters: P-S-E, where P and S are the chamber paced (P) and sensed (S) respectively, and E is the action taken. P and S, can be replaced by V (ventricle) , A (atrium) or D (dual). E can be replaced by O (no action taken), I (inhibited), T (triggered) or D (evaluation of auricular activity). In this case, VVI accounts for V- ventricle paced, V-ventricle sensed, I pacing is inhibited if beat is sensed.

leaded pacemaker. These devices fit the battery and electronics in a compact package that is implanted inside the ventricle. The pacemaker is anchored to the myocardium, being in direct contact with the intracavitary blood. These interactions induce stresses in the tissue and a disturbance in the intracavitary flow, phenomena yet not completely understood. Understanding them, will lead to improvements in device design and operation or the disease treatment.

Description The first step to simulate a leadless pacemaker inside a heart is to include the geometry of the device in the geometrical description of the heart. The device is included in the RV apical region of the whole heart geometry presented in Section 3.2. Figure 5.16 shows the modified geometry, detailing the implantation region. In order to model the third degree AV

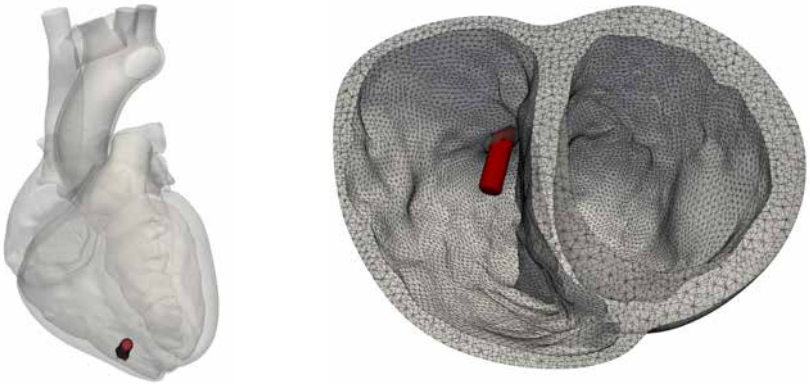

Figure 5.16: Clinical application II. Geometry of the heart including the implanted leadless pacemaker.

block, all the endocardial stimuli are suppressed. The electrophysiology model is excited in a single spot located in the device-tissue interface.

5.4.2 Results

Behavior of the treated heart To model the treatment, a single stimuli is applied in the device-muscle junction. In Figure 5.17 the whole heart model is shown beating as a consequence of the pacemaker. In this figure, the overall activity can be seen. Ahead in this chapter we present deeper analysis of the results for the CFD, the CSM for the whole heart and focusing on the apical region, where the device is implanted.

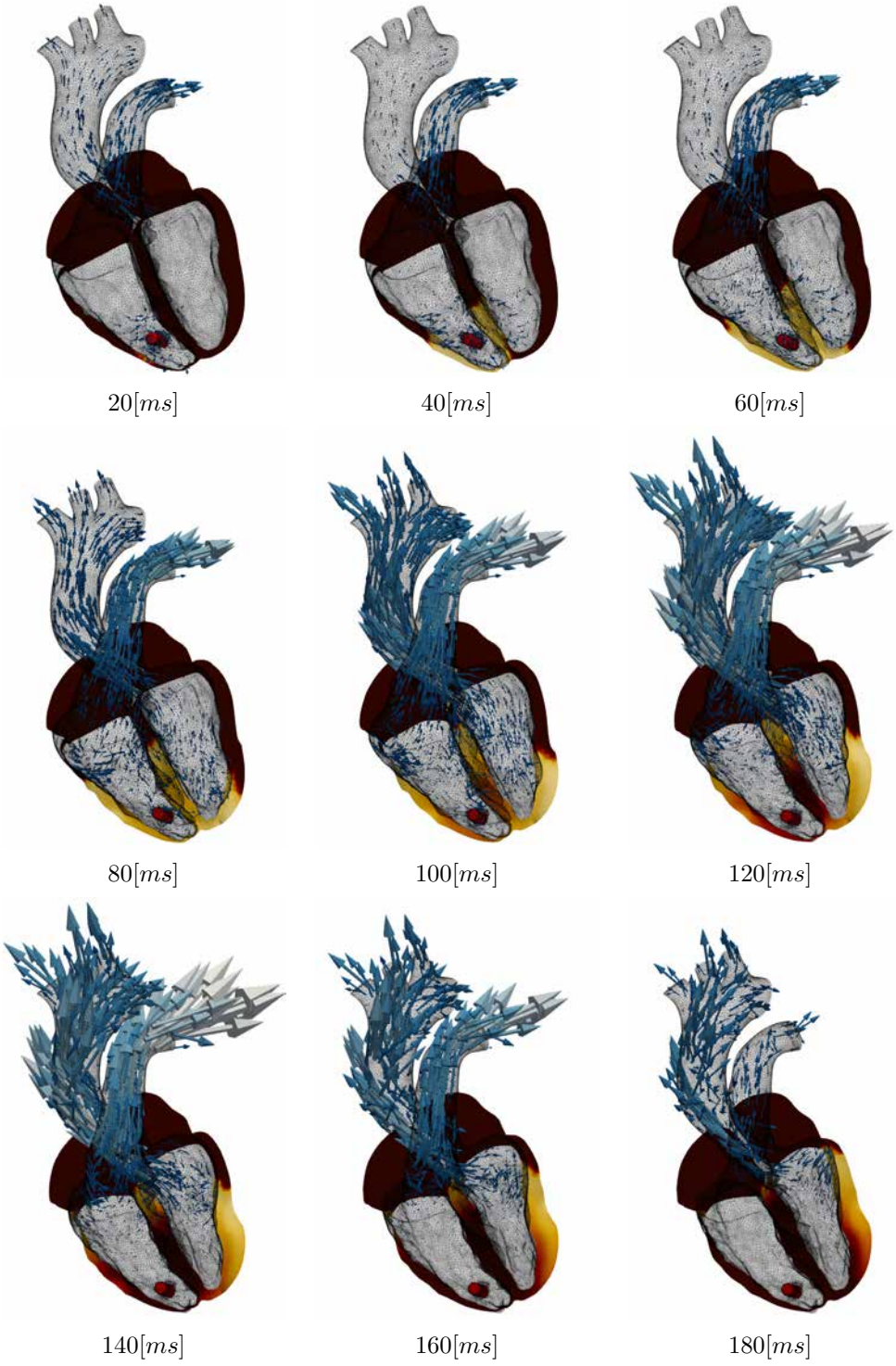

Figure 5.17: Clinical application II: A leadless pacemaker. The long axis slice shows muscle deformation and is coloured by electrical depolarization. The arrows in the fluid domain show the fluid velocity field.

If the results of the paced heart (Figure 5.17) are compared against the healthy ones (Figure 5.2), the base pathology can be seen. In the former, there is no depolarization of the whole endocardial surface. On the contrary, the ventricles only depolarizes as a consequence of the induced pacing stimulus. This punctual depolarization makes the heart to beat again. Figure 5.18 compares curves of ventricular depolarization and outflows for the healthy case and the paced 3rd degree AV block case. Showing the base pathology is futile as no depolarization or ventricular contraction would be seen [4].

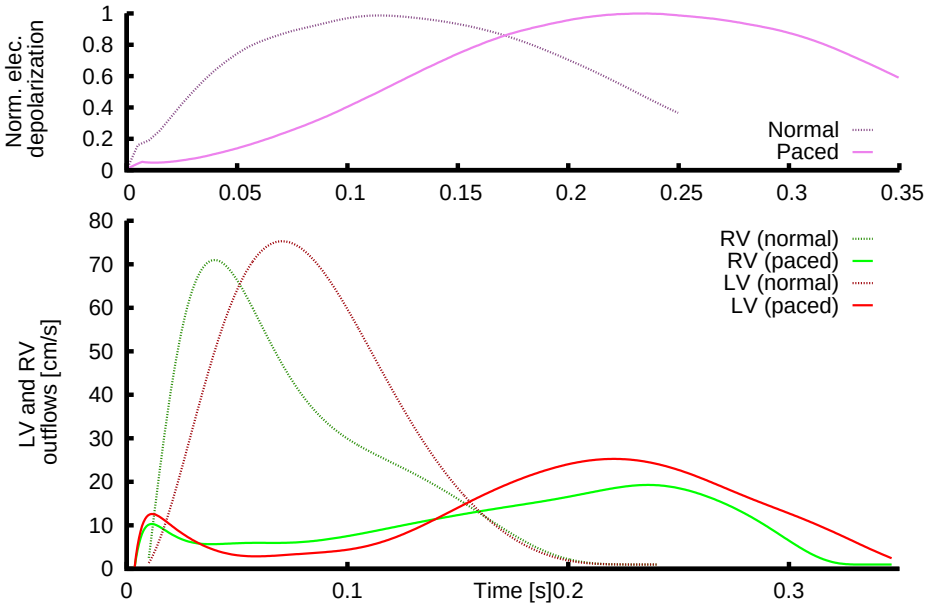

Figure 5.18: Clinical application II. Normalized electrical depolarization and ventricular outflow comparing a healthy case with the paced third grade ventricular block.

In the paced case, the small stimuli area creates a small wavefront [33], inducing a slow ventricular depolarization if compared against the healthy case. Despite this, the ventricular pumping function is partially restored, up to $\sim 50\%$ of the original output.

This model can also be used to analyze the blood flow differences in the ventricle when the device is implanted. Figures 5.19 and 5.20 shows the contraction due to the leadless pacemaker with the contours showing Q-criterion isosurfaces (5000 and 50 $[s^{-2}]$, respectively) coloured by velocity magnitude.

[4] Except for some eventual scape beat, not considered in our model.

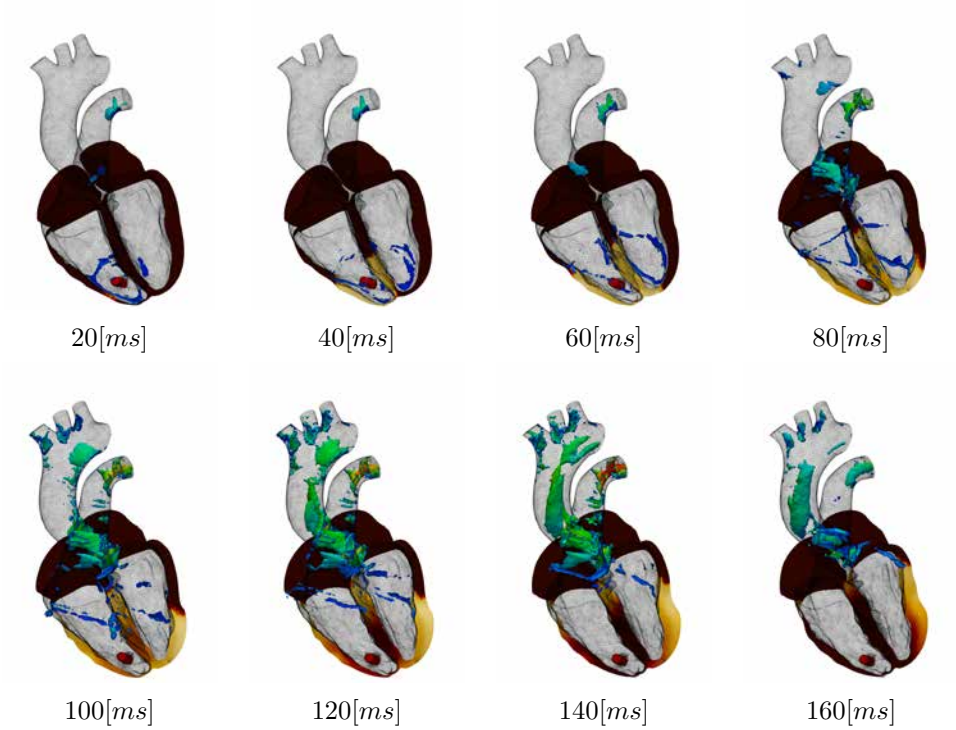

Figure 5.19: Clinical application II: A leadless pacemaker. The long axis myocardium slice shows electrical depolarization and muscle deformation. Q-criterion isosurfaces ($5000[s^{-2}]$) coloured by velocity are shown. The apical stimuli gives a distinctive ventricular vortex pattern. The scales are replicated from Figure 5.6 to ease comparison.

In Figures 5.19 and 5.20, scales are identical to Figures 5.6 and 5.7 to allow an easy comparison. In the healthy heartbeat, all the endocardial surface deforms synchronously to the interior of the cavities. With the punctual stimuli produced by the pacemaker, the electrical wave travels from apex to base, producing a sequential contraction in the same direction. This apex-to-base wave induces a small vortex that follows with the mechanical deformation, feature not present in the healthy systole. It is worth to remark that, although the largest flow speeds are within the arteries, flow patterns closer to the apex has much more complex vortical structures.

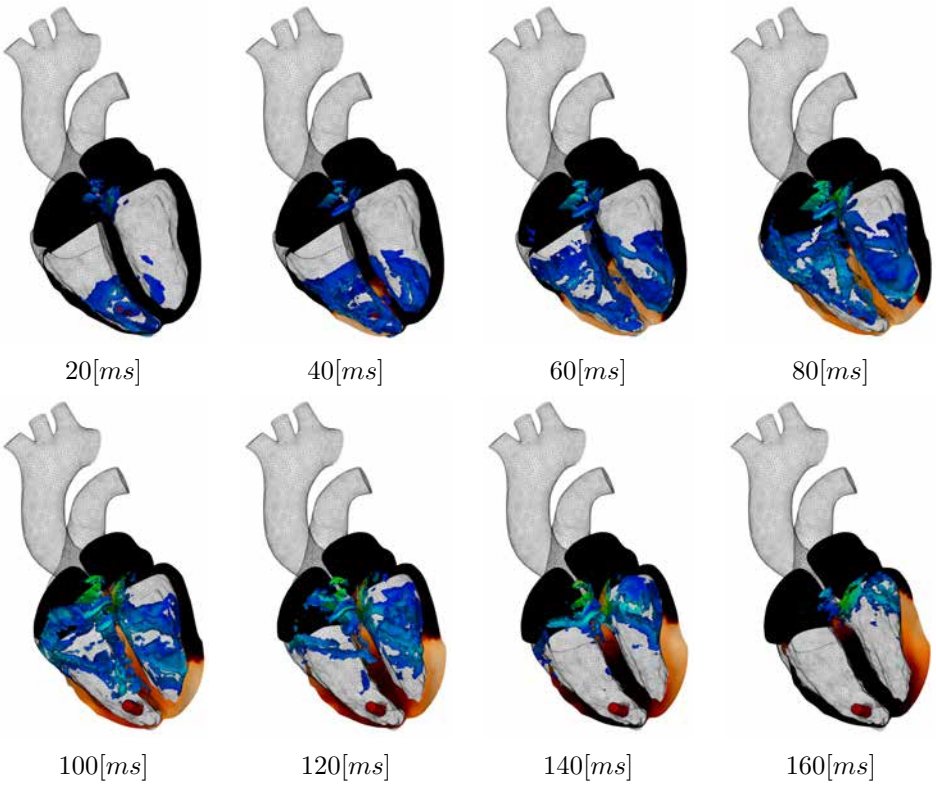

Figure 5.20: Clinical application II: A leadless pacemaker. This figure is presented similarly to Figure 5.19, except that Q-criterion isosurfaces are at $50[s^{-2}]$. This figure is directly comparable with Figure 5.7.

Interaction between the device and the surrounding tissues In this section, we analyze the interaction between the device and the cardiac tissue in the implantation region. Figure 5.21 shows the Von Mises stresses of the apical region including the pacemaker.

Figure 5.21: Clinical application II. Von Mises stresses at maximum contraction for the solid mechanics in the apical region, including the device.

Although there is a small stress concentration around the region where

the device is implanted, the obtained values are in the same order of magnitude as the rest of the tissue. Device insertion area is large if compared against the clinical insertion area (tines or spring, see Figure 5.15), so results may change when the specific anchoring structure is included in the simulation.

Figure 5.22 shows a detail of the apical region including the device, where the interaction of the leadless pacemaker with fluid can be seen. The figure is built so the reader can directly compare the results with the apical view of the healthy heart (Figure 5.9).

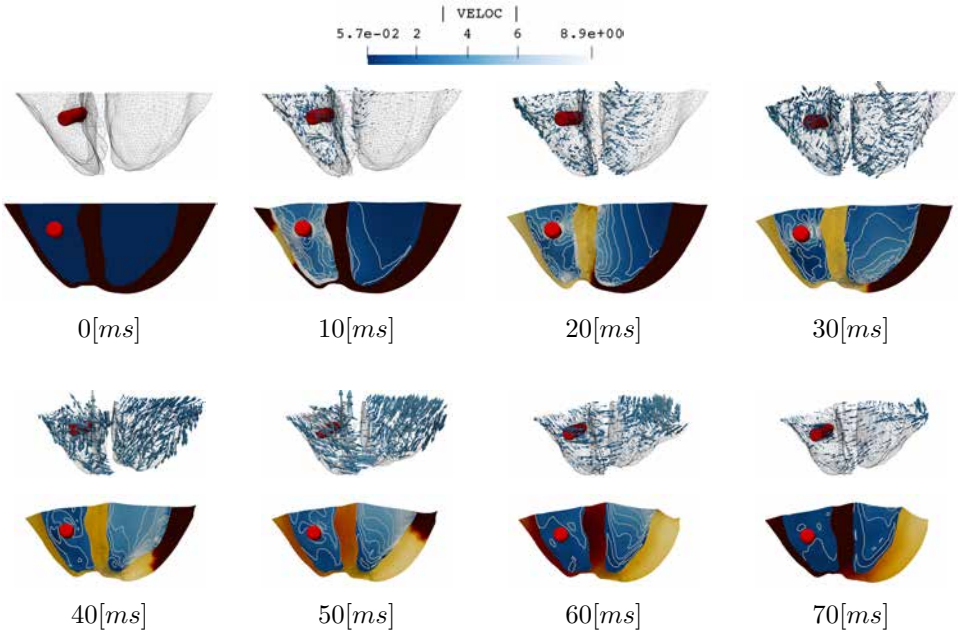

Figure 5.22: Clinical application II. Sequence of images showing a detail of the apical region and the interaction of the leadless pacemaker with the surrounding tissues.

In Figure 5.22 a remarkably different contraction of the apical region can be seen, when compared against the healthy case. As the electrical stimulus is localized in the apex, and not distributed along the endocardium, there is marked apex-base depolarization/contraction sequence. Despite this, the same overall CFD behavior can be seen, with a short initial base-apex component followed by the net apex-base flow. The main difference is the distortion produced in the flow due to the foreign body. *A priori*, a larger displacement of the pacemaker was expected due to the apex-base flow. We suspect that the small displacements obtained are a consequence of the reduced velocities inside the ventricles.

Despite the outflow produced by the paced heart does not reach healthy values (shown in Figure 5.18), the heart affected with III degree AV block,

beats again. Although heart function is restored, it can be improved. In this simulation, one of the functions of the fluid mechanics solvers is to measure the performance of the heart. Fluid mechanics is a consequence of solid mechanics, which is the result of the electrical activity. Analyzing the results, the main problem seems to be the extremely reduced stimulation area produced by the pacemaker. This small excitation area, produces a slow depolarization of the heart, and an anti-natural apex-base sequential contraction (seen on Figures 5.17 and 5.22, but mainly reflected in the fluid-dynamics activity in Figure 5.19).

The simulations presented here inspire alternatives for pacemakers design. For instance, if a more diffuse stimuli could be induced instead of an extremely localized one, a more natural depolarization of the endocardium could be obtained. One can fancy a sort of network-like pacemaker that, instead of depolarizing a focused spot in the myocardium, depolarizes a greater surface of the endocardium, as the Purkinje network does. To conclude, this case shows the potential of the presented fluid-electro-mechanical model not only for cardiac dysfunction and healing therapies but also for device operation and design. With it, overall effect of the device in the heart can be studied, but also the detail of the interaction between the device and the surrounding muscle and blood.

Left ventricular implantation Pacemakers are never implanted in the LV, for several reasons [178]:

- The LV endocardium is less trabeculated making the task of fixing the device more complicated.
- The LV pressures are higher, increasing risks in case of ventricular perforation.
- The LV is more arrhythmogenic.
- There is a higher risk of systemic embolization with endocardial LV pacing.
- Arterial catheterization to the LV involves more risks than venous catheterization to the RV.

Despite this, implanting a leadless pacemaker in the left ventricle may be interesting to cardiologist, as this chamber could be independently paced. In the computational model of the heart none of the disadvantages itemized before occurs, being easy to test different hypothetical situations. For this reason, we solve a case with a leadless pacemaker implanted in the LV. As this results lack of clinical interest nowadays, they are shown in the appendix. The plots presented replicate the views in this section.

Chapter 6

Expanding the model: coupling the computational heart with a 1D arterial network

Para Adán, el paraíso
era donde estaba Eva.

Mark Twain

Summary: In this chapter, a first glance in a fluid-electro-mechanical model of the cardiovascular system is presented. To do this, we couple our 3D fluid-electro-mechanical model of the human heart with a 1D Fluid-Structure interaction (FSI) model of the vasculature developed by the Laboratório Nacional de Computação Científica (LNCC) in Petropolis, Brasil. After describing the governing equations, two academic cases are presented. First a model of a pipe, half modelled with the 3D formulation and the other half with a 1D formulation, is used to validate the numerical scheme. With this example, the coupling variables and the relative error can be measured. After that, a case where single ventricle is connected with a simplified arterial network is presented. Despite that the geometry used in the simulation is not real, the outflow curves shows a physiological response.

6.1 Background

In this chapter we present the first results of a dimensionally heterogeneous model of the cardiovascular system. The model includes the heart and part of the vasculature. This coupled model was developed in a collaboration

between the Barcelona supercomputing center (BSC) and the Laboratório Nacional de Computação Científica (LNCC) in Petropolis Brasil. On the one hand BSC has a fluid-electro-mechanical model of the human heart, extensively described in the previous chapters. On the other hand, LNCC has developed the Anatomically Detailed Arterial Network (ADAN) model, a one-dimensional Fluid-Structure Interaction (FSI) formulation to solve the flow inside deformable pipes [179, 180].

Description of the arterial network ADAN was created from an anatomical database and takes into account more than 1500 arteries from an average human body, featuring a physiologically consistent systemic impedance at the aortic root, among other characteristics [181]. ADAN is build from the definition of the vascular topology, including most of the arteries which are acknowledged in the medical and anatomical literature. In this thesis we present some preliminary results using simplified models for both the arterial network and the heart. We use the ADAN55 model [181], that is a 55 artery version of the full ADAN model (see Figure 6.1).

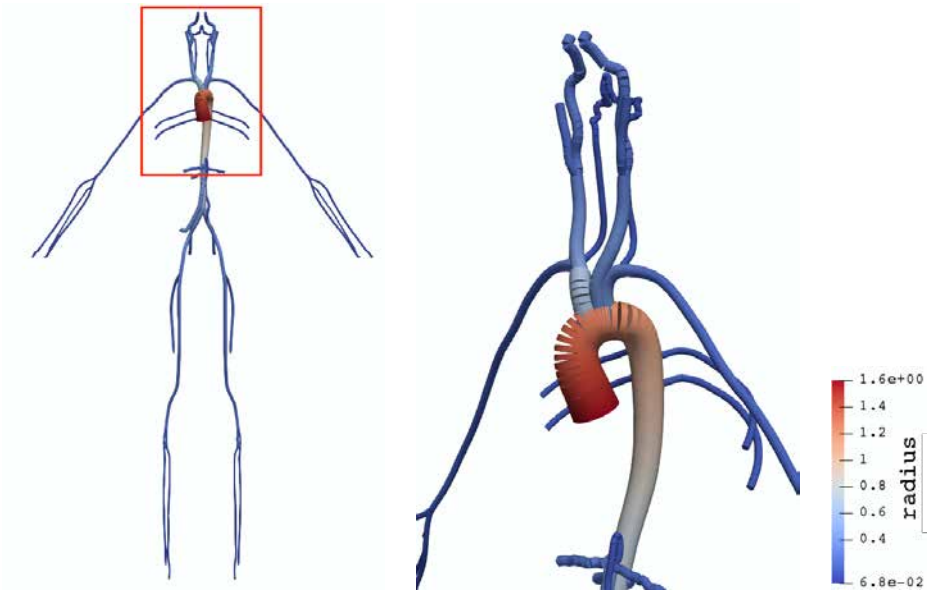

Figure 6.1: ADAN55 model. Left side: whole 1D model. The radius of the arteries are plotted as tubes, so the radius of the vessels can be observed. Right side: detail of the upper part of the model.

Coupling the codes Both codes are coupled by a black-box decomposition approach. On one side, a simplified heart model, which in spite of its geometrical simplicity it solves the fully coupled fluid-electro-

mechanical model described thus far. On the other side, the vascular model solves the condensed 1D Navier-Stokes formulation in compliant vessels (see Figure 6.2 for a scheme of all the problems solved). The codes are coupled by the inclusion of a third coupling software that using a Jacobian free solver, allows a strong iterative coupling strategy.

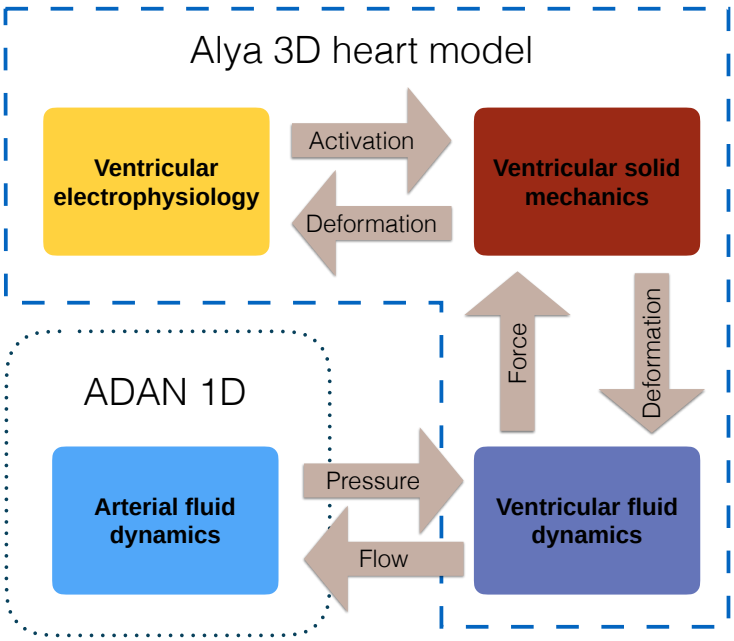

Figure 6.2: Scheme of the coupled problem. The electrophysiology model acts on the solid mechanic problem. The solid mechanics deforms the intracavitary space that pumps out the fluid. This fluid is sent to the arterial network model that returns back a pressure.

Both models are able to run standalone, each one with predefined boundary conditions. In the case of the heart model, a pressure function can be imposed on the outflow to model the resistance of the arterial network. For the ADAN model, a function of a generic aortic root flowrate can be imposed in the inlet, in order to mimic the cardiac function. When both models are coupled through the 3D-1D coupled model, the aortic root flowrate and the systemic impedance of the arterial network are computed for each time step. Then, the pressure imposed connecting outflow of the 3D heart model varies with the flowrate through that output. In the same way, the pressure computed by the ADAN model varies with the incoming blood. This bidirectional coupling model allows to have variable boundary conditions for both the heart and the vascular models. Using this bidirectional 3D-1D coupled model allows us to analyze the effect of one system over the other.

6.2 Governing equations

6.2.1 For the 3D heart model

For the 3D fluid-electro-mechanical model of the human heart, the governing equations and the computational solution strategy are presented above in Chapter 2 and Chapter 3.

6.2.2 For the 1D arterial network model

The governing equations and numerical techniques for the one dimensional arterial network, are extensively described in [179]. Blood flow in large arteries can be modeled using the condensed 1D Navier-Stokes equations in compliant vessels, which comprise momentum and mass conservation as follows:

$$\frac{\partial Q}{\partial t} + \frac{\partial}{\partial x}\left(\alpha_m \frac{Q^2}{A}\right) + \frac{A}{\rho}\frac{\partial P}{\partial x} + \frac{2\pi R}{\rho}\tau_o = 0 \tag{6.1}$$

$$\frac{\partial A}{\partial t} + \frac{\partial Q}{\partial x} = 0, \tag{6.2}$$

where A is the luminal area, R is the radius, Q is the flow rate, P is the mean pressure, ρ is the density and α_m is the momentum correction factor. The term τ_o accounts for the viscous effects since and it has the following form:

$$\tau_o = \frac{f_r \rho U |U|}{8}, \tag{6.3}$$

where U is the mean velocity ($U = A/Q$) and f_r is the Darcy friction factor corresponding to a fully parabolic velocity profile. Equations (6.1) and (6.2) are analogous to the 3D versions (Equations (2.7) and (2.8) respectively) where in 1D version we solve for Q and P and in 3D version for v and p.

The fluid dynamic equations presented are complemented with a constitutive relation for the arterial wall induced pressure:

$$P = P_0 + \frac{Eh}{R_0}\left(\sqrt{\frac{A}{A_0}} - 1\right) + \frac{Kh}{R_0}\frac{1}{2\sqrt{A_0 A}}\frac{\partial A}{\partial t} \tag{6.4}$$

where index 0 refers to reference values, h is the wall thickness and E and K are the material parameters that characterize the elastic and viscoelastic material response respectively.

6.2.3 Coupling strategy

Both codes are coupled by a black-box decomposition approach previously proposed in [179]. For 3D-1D interface, information is exchanged at every iteration of the FSI problem (see Figure 6.3). The 1D arterial network is only

directly coupled with the computational fluid dynamics (CFD) problem in the fluid-electro-mechanical model. This weakly coupled scheme is stable for relatively small time steps.

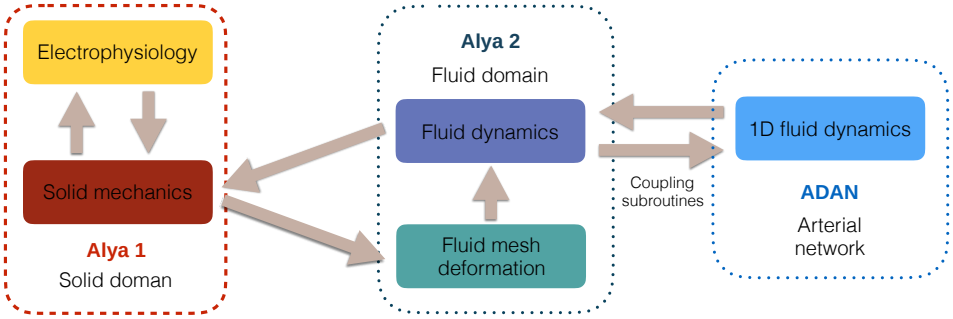

Figure 6.3: Dimensionally heterogeneous model of the cardiovascular system. The scheme shows how the 1D arterial network model is coupled with the fluid-electro mechanical model. In this black-box approach the arterial model is only connected with the CFD problem.

At each time step, the 3D heart FSI problem is solved, computing the velocity field in the connecting boundary. To obtain the flow rate in the interface for the 3D model, the momentum is integrated and then divided by the area A of the boundary:

$$Q_{3D} = \frac{1}{\int_\Gamma d\Gamma} \int_\Gamma \rho \boldsymbol{u} d\Gamma. \tag{6.5}$$

This flow computed in the 3D heart problem is imposed in the arterial network. The 1D formulation is solved, and a pressure is computed for the connecting node. The pressure computed in the arterial network is weakly imposed in the boundary Γ of the 3D model as a forcing term:

$$\boldsymbol{f}_P = \int_\Gamma P_i \boldsymbol{u} d\Gamma. \tag{6.6}$$

For the 1D model, pressure and flow are degrees of freedom in each node of the 1D mesh. Following this statement, four unknowns are defined in the each nodal interface: Q_1, Q_2, P_1 and P_2, using the subindex to identify each model. But continuity of flow and pressure are enforced, so we can say that in the interface i which connects the boxes 1 and 2:

$$Q_i = Q_1 = Q_2 \tag{6.7}$$

$$P_i = P_1 = P_2. \tag{6.8}$$

Additionally, not any combination of Q_i and P_i is possible for each side of the interface: fixing Q_i will automatically determine P_i in each one of the models. In this way, let be defined two equations that relates Q_i and P_i in each node: $F_1(Q_i, P_i) = 0$ and $F_2(Q_i, P_i) = 0$. In this way, flow rate and pressure at the interface i corresponds to a state of the problem [182].

6.2.4 Computational implementation

The Alya 3D heart model is solved using the multi-code approach explained in Section 3.1.1. In this way, the electromechanic problem is computed in one Alya instance. The intracavitary fluid dynamics is solved in another Alya instance. This two problems are bidirectionally coupled to compute the FSI for the simplified ventricle geometry.

The ADAN model of the arterial network is solved by the ADAN solver, that compute the condensed Navier-Stokes equations. This software communicates with Alya through subroutines specifically developed to that end.

6.3 Numerical experiments

6.3.1 A 3D-1D validation case

As a validation case, a 3D cylinder was coupled with a 1D pipe. The 3D cylinder plays the role of the ventricular fluid dynamics model, and the 1D pipe, plays the role of an arterial network. This academic example with an analytical solution eases the task of validating the coupling scheme. If the inflow imposed in the 3D model is measured at the 3D-1D interface, the coupling scheme is correctly implemented.

Description. In this case, a 3D cylinder solved with Alya is coupled with a 1D cylinder solved using ADAN. A diagram is shown in Figure 6.4.

Both cylinders are dimensionally and parametrically consistent: a diameter of $2[cm]$, a longitude of $5[cm]$, viscosity of $0.04[g/cm/s]$ and a density of $1.04[g/cm^3]$ for both sides. The input velocity was set in the Alya inlet as a Poiseullie flow variable on time with the function: $f(t) = 1 - cos(8t)$. The ADAN outlet has an open boundary, with normal stresses equal to zero: $\boldsymbol{n} \cdot \boldsymbol{T} \cdot \boldsymbol{n}$, where $\boldsymbol{T}$ represents the stress tensor. In the walls, non slip condition has been defined $\boldsymbol{u} \cdot \boldsymbol{n} = 0$. The 3D mesh have 7000 elements. The 1D mesh 750 elements and the time discretization has been set in $0.05[s]$. Flow and pressure in the coupling point and convergence for each unknown are shown in Figure 6.5. Convergence is measured with the relative error $\varepsilon(X)$ computed as $\varepsilon(X) = |X(n) - X(n-1)|/|X(n)|$, where X is the unknown.

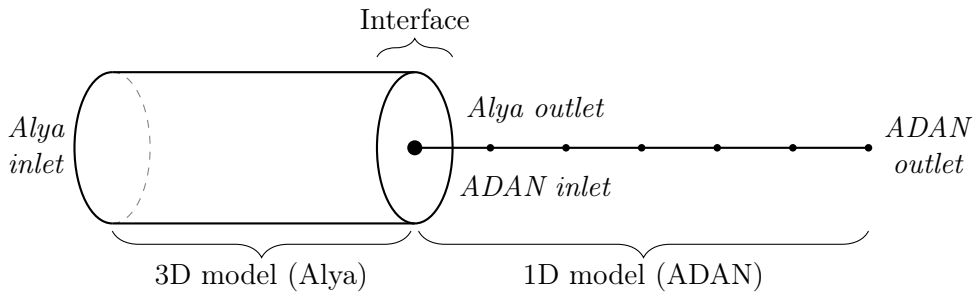

Figure 6.4: Scheme of the model used in the first numerical test. A 3D cylinder was solved with Alya and a 1D cylinder was solved with ADAN.

Results Figure 6.5 shows flow and pressure for the coupling point. The measured quantities replicate the imposed in the inlet. Convergence is also shown, for the coupling point. Relative error is measured for both degrees of freedom, achieving values under $1E-10$ and $1E-8$ for flow and pressure respectively.

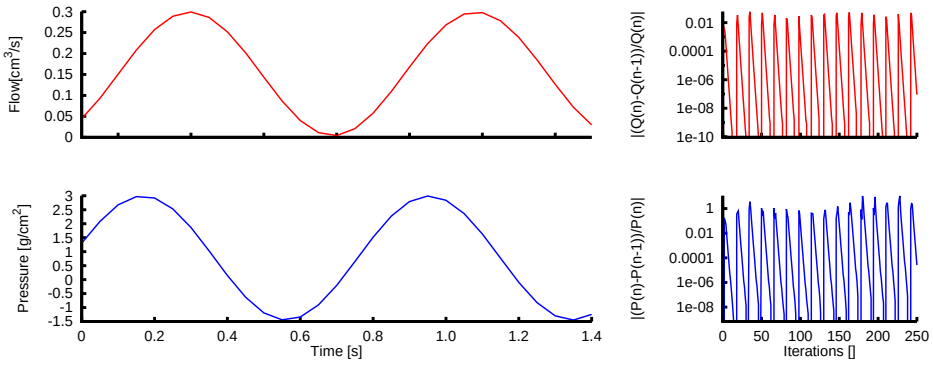

Figure 6.5: 3D-1D coupling, validation case. Flow and pressure in the coupling point, next to relative error.

6.3.2 Simplified ventricle coupled with ADAN55

After validating the numerical method used, we present a conceptual example where model a simplified ventricle connected with the ADAN55 model. The main goal of this case is to exemplify how the cardiovascular model can be used, using test geometries.

Description The geometry of the simplified ventricle is created using an ellipsoidal cavity made of an active cardiac tissue. The fibre field is created with the Streeter technique (see Section 3.2.2), varying linearly from $-60°$

to $-60°$. A short non-active tubular part plays the role of the aorta. The activation potential starts at the bottom. The fluid and the solid meshes combined have $\sim$ 7000 elements.

The arterial network mesh is the ADAN55 geometry, depicted in Figure 6.1. This mesh is built with $\sim$ 2000 1D elements arranged in the three dimensional space.

Results Figure 6.6 shows a snapshot of the cardiovascular coupled simulation. In this figure the mesh of the ventricle is shown with the

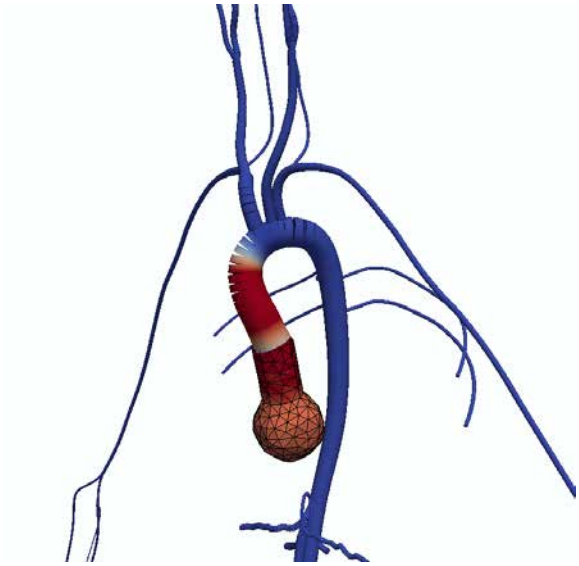

Figure 6.6: Detail of the results for the coupled cardiovascular model. The ventricle shows depolarization of the myocardium and the 1D model the flow wave.

myocardial depolarization. The 1D arterial network shows the flow wave. It is worthy to note that, as it is a distensible pipe, flow and pressure travel in waves. A slice of the simplified ventricle together with the intracavitary fluid dynamics are shown on the image sequence in Figure 6.7. The depolarization is followed by the contraction and the blood ejection. Systole happens in a short period of time ($50[ms]$) as the dimensions and the diffusion parameters are not tuned to obtain physiological measurements. Despite that, this academical example fulfills its purpose. Flow, pressure, and the error in the convergence are shown in Figure 6.8. Due to the small intracavitary volume on the artificial ventricular geometry, the outflow does not achieve physiological values. Despite this, the shape of the flow in Figure 6.8 reminds to the Wiggers diagram presented in Figure 1.3. Flow and pressure show a notch during the first moments of the ejection. This phenomenon is also seen in experimental measurements and is due to the reflection of the wave

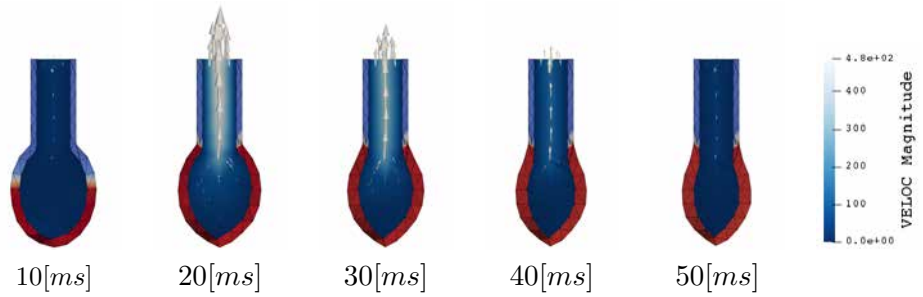

Figure 6.7: Simplified ventricle. This figure shows an image sequence of the simplified ventricle that is coupled with the arterial network model.

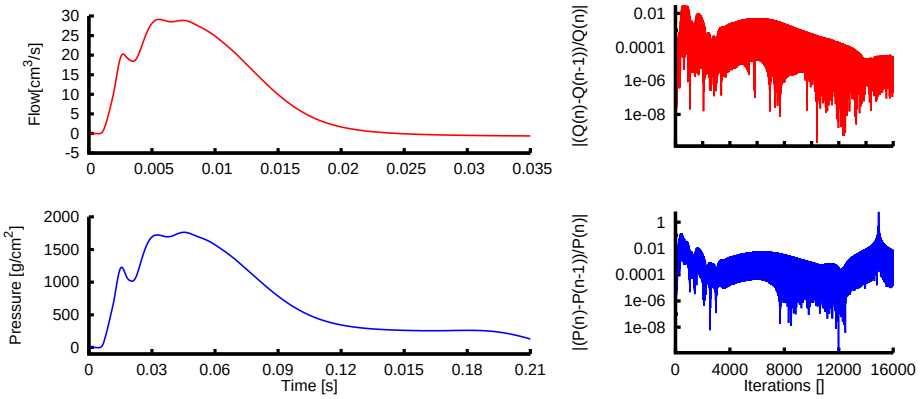

Figure 6.8: Coupled cardiovascular model. Flow and pressure in the coupling point, next to the relative error for each unknown.

in the bifurcations in the arterial network.

To conclude, with this academical example, we show a simplified version of the cardiovascular system. Despite geometries are far from real, the pressure and flow measurements have a behavior that resembles the physiological response. The message is that the computational heart model has all the potential of being connected with arterial and venous network, becoming the "heart" of a full cardiovascular system simulation.

Chapter 7

Conclusions and future lines

Ce que nous connaissons
est peu de chose,
ce que nous ignorons
est immense.

Pierre-Simon Laplace

Summary:

This chapter firstly recapitulates the main features, contributions and accomplishments of this thesis. Then, we discuss new applications for the current model and improvements to widen the application range.

7.1 Summary

In this thesis a fluid-electro-mechanical model of the human heart have been presented. We start analyzing the anatomy and function of the organ under study, decomposing the heartbeat problem in the three building blocks. The tight relation between the different structures and physics involved is always present along the discussion, understanding the heartbeat as a fluid-electro-mechanical system. Each one of the independent physics is, by itself, computationally demanding. Even more, when these problems are coupled, the computational cost is greater than the sum of their components and the supercomputing resources becomes mandatory. This is why, we propose a new fluid-electro-mechanical model of the human heart for supercomputers.

7.1.1 Discussion of this thesis chapter by chapter

1. **Foreword.** The first chapter starts with a brief description of the heart physiology and introducing concepts required ahead in the document.

A review on the state-of-the-art for each independent problem is done, but focusing in current fluid-electro-mechanical models. The importance of having the three physics coupled is stated, and this multi-physics approach is used as a motivation to implement the models with supercomputing resources. Despite this, the three-physics model is not always mandatory but dependent on the hypothesis done and the purpose of the study.

2. **Governing equations.** The heartbeat problem is decomposed in the three coupled physics using an engineer point of view. Electrophysiology is modelled with the human cell ionic current model of O'Hara-Rudy. As the hypothesis and purpose of this thesis does not require a complex cell model, using such formulation may result arguable. Despite this, solving the nodal ordinary differential equation (ODE) of the chosen cell model does not represent a considerable increment in the computational cost in this case, as the solver is parallel and implemented using a semi-implicit approach. Solid mechanics is modelled with the Holzapfel-Ogden energy form for ventricles. Despite it is not a viscoelastic material model, is widely accepted by the simulation community. The problem is solved dynamically and the oscillations damped using Rayleigh damping. Fluid dynamics is solved using the Newtonian incompressible Navier-Stokes equations. This approach is completely valid at the velocities and pressures seen in the intracavitary space. Fluid-Structure Interaction (FSI) is described with a Dirichlet-Neumann approach. On the one hand, force is applied against the solid. On the other hand, displacements are imposed in the deformable fluid domain.

3. **Computational implementation.** A multi-code approach is used to solve the problem. In one domain (the structure domain) electrophysiology (EP) and computational solid mechanics (CSM) are solved. In the other (fluid domain) the computational fluid dynamics (CFD) equations in an arbitrary Lagrangian-Eulerian (ALE) are computed. Solving EP and CSM under the same mesh is not the typical approach in the bibliography as, generally, EP requires a finer mesh compared with CSM. We chose to solve them under the same mesh for two reasons: *1.* Interpolations are not required; *2.* The CSM solver has a good scalability. Using a multi-code ALE method to solve the FSI problem with large deformations is not the classical approach. The main problem of using the ALE method is that the fluid domain elements may get flatten or inverted, producing the divergence of the solution. In order to be able to compute the final result, the preprocessing meshing step requires lots of effort. Using the immersed boundary (IB) technique would save this energy, as the fluid dynamics problem is solved in a fixed mesh. The disadvantage of the IB method is that it lacks spatial precision due to the interpolations required. To mitigate the instabilities

produced by the partitioned approach a novel high performance coupling strategy is developed, the so called Compact interface quasi-Newton (CIQN). A whole heart is used as a solving domain, including boundary conditions based on medical observations.

4. **Basic experiments in simplified geometries.** The first set of experiments are designed to verify the model implementation and to test the proposed hypothesis. First, some classical experiments are reproduced. Then, the boundary conditions and whole heart geometry are tested. Using the sliding pericardial boundary condition shows a higher physiological consistency, compared against other classical approaches. Also, we show that the whole heart geometrical model is recommended as even affects ventricular dynamics.

5. **Fluid-electro-mechanical simulations in a whole-heart model.** First, a healthy systole is analyzed to set a reference point for the following numerical experiments. Myocardium deformation shows consistency with physiological observations with a base-apex displacement of the base, and a twisting of the apex. CFD also shows physiological features, with smaller velocities in the ventricular space and higher velocities in the aortic root. Despite this difference on the velocities, the vortical structures present in the ventricles are more complex than the ones present in the vessels. This is to say, the flow in the output vessels is faster but simpler. As a first clinical case, a left bundle branch block (LBBB), is modelled in the computational heart. There is a marked dyssynchrony between the right ventricle (RV) and the left ventricle (LV), something already stated in the published bibliography. In this work, we also analyse the heart performance through a CFD study. A massive drop in the ejection fraction (EF) is seen in both ventricles accompanied with a marked dyssynchrony in their ejection. This diseased heart is posteriorly treated with cardiac resynchronization therapy (CRT). The treatment applied produced remodeling of the affected organ, reducing the end systolic volume (ESV) and therefore increasing the EF. The second clinical case modelled, is the operation of an implanted leadless pacemaker in a heart affected by a III degree atrioventricular (AV) block. In the overall analysis, even though the heart beats again, the outflow values does not reach the reference values obtained in the healthy case. The reason for this is, probably, the high locality of the applied stimuli. The main interest of this case is the device-tissue interaction. Stresses are accumulated around the device-myocardium interface, but in the same scale as the rest of the heart. Apical flow is disturbed due to the presence of the device, but not in a severe manner due to the reduced apical velocities.

6. Expanding the model: coupling the heart with an arterial network. In this chapter the fluid-electro-mechanical model is expanded coupling an arterial network model. With it, both computational models have a feedback for their respective outflow/inflow. The model is tested with a simplified geometry for the ventricle and a simplified geometry for the arterial network.

7.1.2 Accomplishments of this thesis

During the development of this thesis, the proposed goals have been achieved. The scientific contributions are:

a. **A robust HPC-based FSI algorithm for biomechanics.** As explained in the first part of this thesis, the FSI problem is specially problematic in biomechanics. There are multiple interfaces to solve, and the added mass instability is generally present as a consequence of the similar densities between the blood and the tissue. We have developed the CIQN algorithm capable of dealing with such problems. The algorithm is validated and tested in the numerical examples section. Thanks to an HPC-based design and implementation, the algorithm is highly efficient to solve large-scale problems.

b. **A set up for a fluid-electro-mechanical model of the human heart.** To build the three physics heart model, the governing equations and the numerical methods have to be explained. Particularly for electrophysiology, the human cell model of O'Hara-Rudy is used. The solid mechanics have been modelled with the Holtzapfel-Ogden formulation, bidirectionally coupled with electrophysiology by the Hunter-McCulloch scheme. Fluid dynamics have been solved using the Navier-Stokes equations with an arbitrary Lagrangian-Eulerian formulation. The FSI problem has been solved using the CIQN technique. These models have been solved in a whole heart geometry. This simulation scenario includes ventricles, atrium, great vessels and a fibre/cell field created with Streeter's rule-based method. Finally, detailed boundary conditions have been proposed, based on medical image analysis.

c. **A simulation and analysis of a healthy heartbeat.** Using the fluid-electro-mechanical whole-heart model, we firstly simulate a healthy heartbeat, focusing on systole. All the framework developed have been used, without any pathological condition purposely induced. This first case is deeply analyzed and compared against experimental measurements and medical images whenever possible. Also, this simulation is used as a reference point for the pathologic cases presented afterwards.

d. **A simulation and analysis of an LBBB heart and a CRT.** In the first pathological case a LBBB has been modelled and studied. The behavior seen in the results agrees with physiological observations. After, a CRT has been performed to the LBBB model, restoring the cardiac function.

e. **A simulation of an intracardiac pacemaker.** In the second clinical case, a leadless pacemaker has been implanted to a heart suffering of a third degree AV block. The main objective of the case is to see the interaction between the device and the surrounding tissues. Due to this, we focus the study in the apical region, where the device is implanted.

f. **A coupled cardiovascular model.** As a first step to expand the model, a simplified version of a ventricle has been coupled with a one dimensional arterial network. In order to do this, a 3D-1D coupling strategy has been developed and implemented in the involved codes. The model is firstly validated with an academic example, and then tested with simplified geometries.

7.1.3 Uses for the proposed model: a computational cardiac workbench

The hypotheses proposed to solve the heart allow us to move forward in computational heart modeling. Despite the results presented in this thesis resemble to experimental measurements, there is still a long way to obtain a fully validated heart model. We never have to forget that, in numerical experimentation, we are studying the behavior of a *model* of the human heart. Under this assumption, the model can be extensively applied to clinical problems. The extreme detail in the ionic currents of the O'hara-Rudy model opens the door for pharmaceutical industry. With this model, ejection fraction (EF) can be computed in a diseased heart and after treating with membrane permeability modifying drugs. The robust FSI algorithm proposed can be used to test virtually all the structural pathologies of the heart, among them myocardial infarction, hypertrophic cardiomyopathy, patent ductus arteriosus, atrial septal defect or acute/chronic heart failure, to name a few. Biomedical technology industry can also find this model very useful. Virtually, all the biomedical devices can be tested in this heart dummy during the design process, in order to reduce the stratospheric research and development costs of biomedical devices industry and animal experiments.

7.2 Future work

It is out of question that computational medicine is gaining wider acceptance in the clinical community. The model developed in this thesis has numerous applications, but it can expanded to widen the fields of impact. On the one hand, we propose the use of this model in problems such as:

- Broaden the CRT study presented in Section 5.3. Mapping the optimal lead tip position in the epicardium and the synchronization time in order to optimize the EF would have a great impact in the medical community.
- Study congenital structural pathologies. Only by modifying the myocardium geometry, allows us to study structural problems and to test treatments.
- Study the effect of drugs in the overall behavior of the heart. The electrophysiology model can be easily tuned to behave as in presence of drugs. This can be used to analyze the impact in the EF.
- Simulate other intracardiac biomedical devices. This model can be used to design cardiac devices, not only leadless pacemakers, but also pacemaker tips or sutures.

On the other hand, the model can be improved to make the model more computationally efficient and widen the application range:

- Move from an explicit CSM formulation to an implicit one. Differences in Young modulus when solving biomedical devices reduces the critical time step in several orders of magnitude. This feature will improve simulation times.
- Implement the Jacobi scheme for the FSI coupling. Despite it has been proven that a Jacobi scheme is eventually less stable for scalar coupling schemes as the Aitken, it should be as stable as the Gauss-Seidel scheme for the quasi-Newton algorithm developed.
- Move from an ALE formulation to an IB formulation for the FSI problem. As the latter technique uses a Cartesian mesh in the fluid, the mesh generation is simplified. The IB technique is less accurate. Also it allows to model heart valves and simplify the overall scheme.
- Use more precise boundary conditions. The work done in Chapter 6 is an effort to improve outflow/inflow boundary conditions for both models. Coupling a 1D arterial network to the heart model improves the outflow pressure boundary condition. In the same way, using a

computational heart as an input for the arterial network, improves the inflow boundary condition for the 1D model.

- Move forward in patient specific geometries. The pathline from imaging acquisition to meshes for simulation is neither straightforward nor automatic. Being able to easily create a simulation mesh from an Magnetic Resonance Imaging (MRI) or computed tomography (CT) image is critical for simulations in computational medicine.

A computational model of an entire human, modelled from the molecular level to the organ structure, would help to understand pathologies and test novel drugs or surgical procedures. This thesis is a step towards the computational human. In a near future, models like this will change the way pathologies are understood and treated, and the way biomedical devices are designed.

7.3 Scientific publications

Now we present a list of the scientific work done this thesis [1]:

7.3.1 In peer-reviewed journals:

- Santiago, A., Aguado-Sierra, J., Arís, R., Casoni, E., Lopez-Yunta, M., Rivero, M., Sacco, F., Houzeaux, G., Vazquez, M. Clinical and Industrial applications with a fluid-electro-mechanical model of the human heart. (2017). Frontiers in physiology. (submitted).

- Santiago, A., Aguado-Sierra, J., Zavala, M., Doste-Beltran, R., Gomez, S., Arís, R., Vazquez, M. Fluid-electro-mechanical model of the human heart for supercomputers. (2017). International Journal for Numerical Methods in Biomedical Engineering (in review).

- Santiago, A., Zavala, M., Vazquez, M., Cajas, J. C., Houzeaux, G. HPC-Based Comptact Interface Quasi-Newton Algorithm for Fluid-Structure Interaction. (2017) SIAM Journal on Scientific Computing, (in review).

- Vázquez, M., Arís, R., Aguado-Sierra, J., Houzeaux, G., Santiago, A., López, M., Cajas, J. C. Alya Red CCM: HPC-Based Cardiac Computational Modelling. (2015). Selected Topics of Computational and Experimental Fluid Mechanics, 189. DOI: 10.1007/978-3-319-11487-3 11

[1] For an updated list of publications and work experience, please refer to orcid.org/0000-0002-9374-1275, scholar.google.com/citations?user=eS1VzE0AAAAJ and researchgate.net/profile/Alfonso_Santiago3.

7.3.2 In conferences, seminars and workshops:

- **2017**
  - Compact Interface quasi - Newton algorithms for HPC applications. Alfonso Santiago, Miguel Zavala-Aké, Mariano Vázquez, Juan Cajas-García and Guillaume Houzeaux. VII International Conference on Coupled Problems in Science and Engineering. Rodhes, Grece, 2017.
  - Transcatheter Pacing Systems: Coupled Fluid - Electro - Mechanical Cardiac Computational Model. Alfonso Santiago, Jazmin Aguado-Sierra, Eva Casoni, Ruth Aris, Juan Carlos Cajas Garcia, Guillaume Houzeaux, Mariano Vázquez. 5^{th} International conference on Computational and Mathematical Biomedical Engineering. Pittsburgh, United States. 10-12 April 2017.
- **2015**
  - From imaging to simulation: a framework applied to simulate the blood flow in the carotids. Ruth Aris, Venkatesh Mani, Hadrien A Dyvorne, M Jowkar, A Santiago, G Houzeaux, Zahi Fayad, Mariano Vazquez. 2nd BSC doctoral symposium.
  - A dimensionally heterogeneous coupled cardiac-vascular model. A. Santiago, M. Vázquez, P. J. Blanco, G. Houzeaux, J. Aguado-Sierra, S. Watanabe, M. Lopez Yunta, M. Rivero. "4th International Conference on Computational and Mathematical Biomedical Engineering (CMBE)", Cachan, France. 2014.
  - A 3D-1D cardiac-vascular computational feedbacked model. A. Santiago, M. Vázquez, P. J. Blanco, G. Houzeaux, J. Aguado-Sierra, S. Watanabe, M. Lopez Yunta, M. Rivero. "BSC 2nd International Doctoral Symposium 2015".
  - Fluid-structure simulations in carotid arterial plaque. R. Arís, V. Mani, H. Dyvorne, M. Jowkar. A. Santiago, Z. Fayad, M. Vázquez. "1st Pan-American Congress on Computational Mechanics".
  - A dimensionally heterogeneous coupled HPC cardiac-vascular model using a black box decomposition approach. A. Santiago, M. Vázquez, P. J. Blanco, G. Houzeaux, J. Aguado-Sierra, S. Watanabe, M. Lopez Yunta, M. Rivero. "1st Pan-American Congress on Computational Mechanics".
  - A 3D-1D cardiac-vascular computational feedbacked model. A. Santiago, M. Vázquez, P. J. Blanco, G. Houzeaux, J. Aguado-Sierra, S. Watanabe, M. Lopez Yunta, M. Rivero. "2nd

International Workshop on Latest Advances in Cardiac Modeling LACM 2015".

- **2014**
  - Fully-Coupled Electromechanical Simulations of the LV Dog Anatomy Using HPC: Model Testing and Verification. Aguado-Sierra, J., Santiago, A., Rivero, M.I., López-Yunta, M., Soto-Iglesias, D., Dux-Santoy, L., Camara, O., Vazquez, M. (2014). Statistical Atlases and Computational Models of the Heart - Imaging and Modelling Challenges. STACOM 2014. Lecture Notes in Computer Science, vol 8896. Springer. DOI: 10.1007/978-3-319-14678-2 12

Chapter 8

Appendix

Mistakes are not a problem.
Not learning from them, is.

Anonymous

8.1 Appendix I: Results for a left ventricular implanted leadless pacemaker

8.1.1 Behavior of the treated heart

Figure 8.1 shows electrical depolarization and outflow for the LV and the RV as shown in Figure 5.18 but for a left heart implantation. Figure 8.2 shows an overall systole for the paced heart.

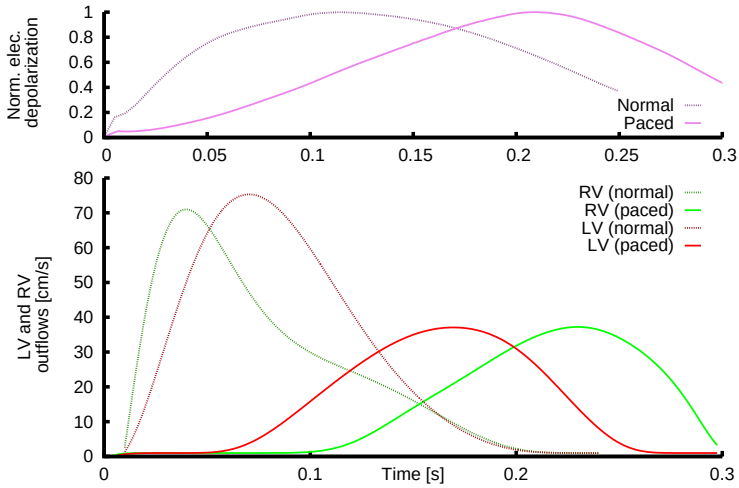

Figure 8.1: Leadless pacemaker in the left ventricle. Normalized electrical depolarization and ventricular outflow for the healthy and the pathologic case.

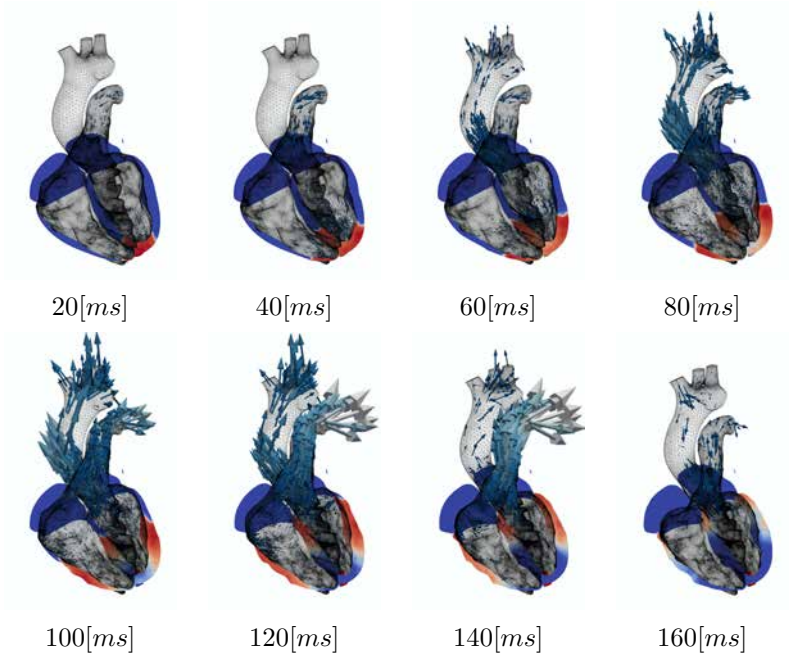

Figure 8.2: Leadless pacemaker in the left ventricle.Depolarization, contraction and fluid velocities for the paced heart.

Figure 8.3 shows the contraction due to the leadless pacemaker with the contours showing Q-criteria isosurfaces coloured by velocity magnitude, as

done in Figure 5.19, but for a LV implantation.

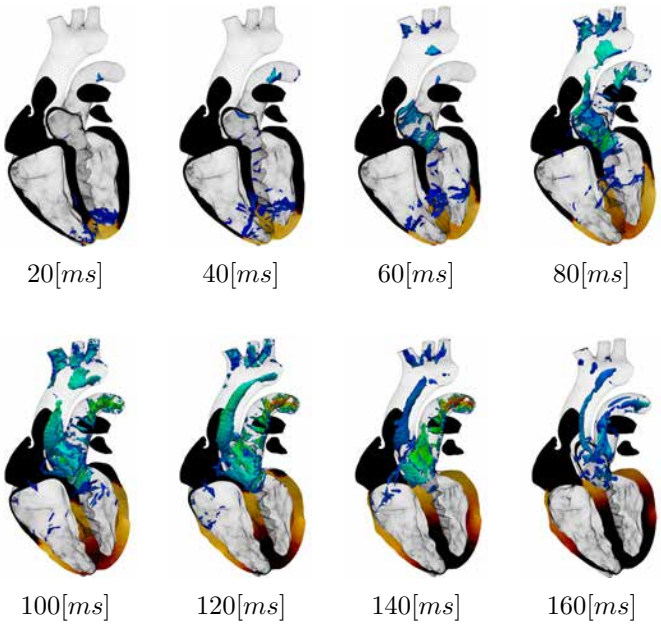

Figure 8.3: Leadless pacemaker in the left ventricle. The contours show the Q-criteria ($5000[s^{-2}]$), and are colored by velocity magnitude.

8.1.2 Analysis of the device-tissues interaction

As the device is located in the apical area, the views in this section will focus in that specific region. Figure 8.4 shows a detail of the apex including the device, where the interaction of the leadless pacemaker with the surrounding tissues can be seen.

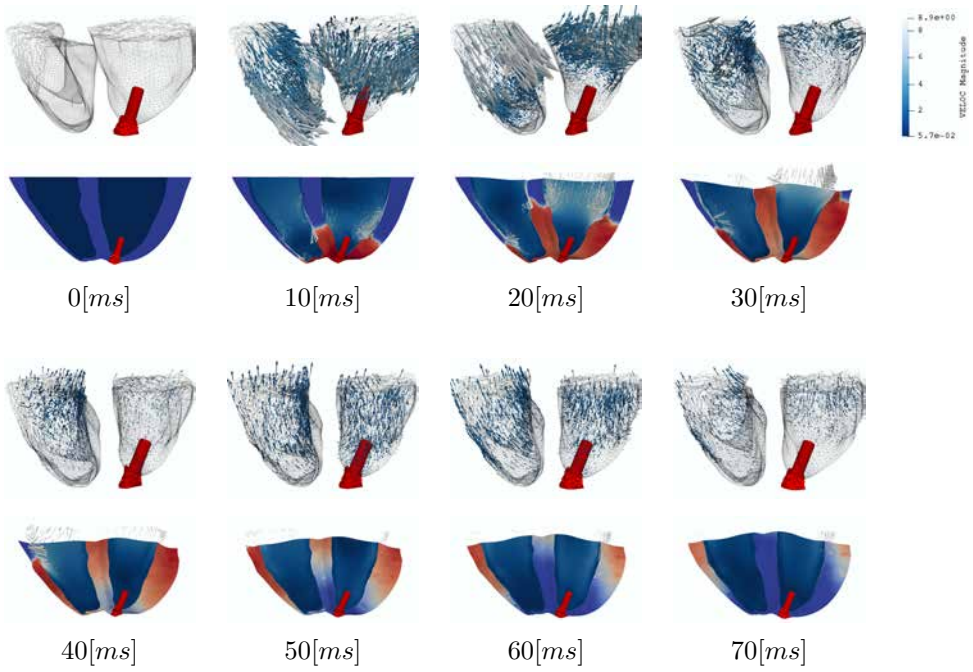

Figure 8.4: Leadless pacemaker in the left ventricle. Detail of the apical region and the interaction of the leadless pacemaker with the surrounding tissues.

Bibliography

Y así, del mucho leer y del poco dormir,
se le secó el celebro de manera que vino
a perder el juicio.

Miguel de Cervantes Saavedra

[1] Emelia J. Benjamin, Michael J. Blaha, and Al. Et. *Heart Disease and Stroke Statistics - 2017 Update: A Report From the American Heart Association*. American Heart Asociation, 2017.

[2] Alan M Turing. On computable numbers with an application to the AlanTuringproblem. *Proceedings of the London Mathematical Society*, 25(2):181–203, 1937.

[3] J.D. Humphrey. Continuum biomechanics of soft biological tissues. *Proc. R. Soc. Lond.*, 459:3–46, 2002.

[4] OpenStax. *Anatomy and physiology*. OpenStax CNX, Huston, TX, on-line edition, 2013.

[5] Edward J Vigmond, Clyde Clements, David M. McQueen, and Charles S Peskin. Effect of bundle branch block on cardiac output: A whole heart simulation study. *Progress in Biophysics and Molecular Biology*, 97(2-3):520–542, 2008.

[6] Blausen.com. Medical gallery of Blausen Medical 2014, 2014.

[7] Daniel D. Streeter and David L. Bassett. An engineering analysis of myocardial fiber orientation in pig's left ventricle in systole. *The Anatomical Record*, 155(4):503–511, 1966.

[8] D D Streeter, Henry M Spotnitz, Dali P Patel, J Ross, and Edmund H Sonnenblick. Fiber orientation in the canine left ventricle during diastole and systole. *Circulation research*, 24(3):339–347, 1969.

[9] C. Antzelevitch and J. Fish. Electrical heterogeneity within the ventricular wall. *Basic Research in Cardiology*, 96(6):517–527, 2001.

[10] C Antzelevitch, W Shimizu, G X Yan, S Sicouri, J Weissenburger, V V Nesterenko, A Burashnikov, J Di Diego, J Saffitz, and G P Thomas. The M cell: its contribution to the ECG and to normal and abnormal electrical function of the heart. *Journal of Cardiovascular Electrophysiology*, 10(8):1124–52, 1999.

[11] C Antzelevitch, S Sicouri, S H Litovsky, a Lukas, S C Krishnan, J M Di Diego, G a Gintant, and D W Liu. Heterogeneity within the ventricular wall. Electrophysiology and pharmacology of epicardial, endocardial, and M cells. *Circulation research*, 69(6):1427–1449, 1991.

[12] Serge Sicouri, Jeffrey Fish, and Charles Antzelevitch. Distribution of M cells in the canine ventricle. *Journal of Cardiovascular Electrophysiology*, 5(10):824–837, 1994.

[13] Siew Yen Ho, Robert H. Anderson, and Damián Sánchez-Quintana. Atrial structure and fibres: Morphologic bases of atrial conduction. *Cardiovascular Research*, 54(2):325–336, 2002.

[14] Serdar Göktepe, Oscar John Abilez, Kevin Kit Parker, and Ellen Kuhl. A multiscale model for eccentric and concentric cardiac growth through sarcomerogenesis. *Journal of theoretical biology*, 265(3):433–42, aug 2010.

[15] Henry Gray. *Anatomy of the Human Body*. Philadelphia, 20th edition, 1918.

[16] Toshinari Onishi, Samir K Saha, Antonia Delgado-montero, Daniel R Ludwig, Tetsuari Onishi, Erik B Schelbert, and David Schwartzman. Global Longitudinal Strain and Global Circumferential Strain by Speckle-Tracking Echocardiography and Feature-Tracking Cardiac Magnetic Resonance Imaging : Comparison with Left Ventricular Ejection Fraction. *Journal of the American Society of Echocardiography*, pages 1–10, 2015.

[17] A. Prakosa, P. Malamas, S. Zhang, F. Pashakhanloo, H. Arevalo, D. A. Herzka, A. Lardo, H. Halperin, E. McVeigh, N. Trayanova, and F. Vadakkumpadan. Methodology for image-based reconstruction of ventricular geometry for patient-specific modeling of cardiac electrophysiology. *Progress in Biophysics and Molecular Biology*, 115(2-3):226–234, 2014.

[18] L Geerts, P Bovendeerd, K Nicolay, and T Arts. Characterization of the normal cardiac myofiber field in goat measured with MR-diffusion tensor imaging. *Am J Physiol Heart Circ Physiol*, 283(1):H139–145, 2002.

[19] Manish Bansal and Ravi R Kasliwal. How do I do it ? Speckle-tracking echocardiography. *Indian Heart Journal*, 65(1):117–123, 2012.

[20] Gerald Buckberg, Julien I E Hoffman, Aman Mahajan, Saleh Saleh, and Cecil Coghlan. Cardiac mechanics revisited: the relationship of cardiac architecture to ventricular function. *Circulation*, 118(24):2571–87, 2008.

[21] Gianni Pedrizzetti and Federico Domenichini. Nature optimizes the swirling flow in the human left ventricle. *Physical Review Letters*, 95(10):1–4, 2005.

[22] H. Watanabe, S. Sugiura, and T. Hisada. The looped heart does not save energy by maintaining the momentum of blood flowing in the ventricle. *AJP: Heart and Circulatory Physiology*, 294(5):H2191–H2196, 2008.

[23] A. L. Hodgkin and A. F. Huxley. A quantitative descritpion of membrane current and its application to conduction and excitation in the nerve. *Journal of Physiology*, 117(117):500–544, 1952.

[24] Richard FitzHugh. Impulses and physiological states in theoretical models of nerve membrane. *Biophysical journal*, (1948), 1961.

[25] Flavio H Fenton and Alain Karma. Vortex dynamics in three-dimensional continuous myocardium with fiber rotation: Filament instability and fibrillation. *Chaos (Woodbury, N.Y.)*, 8(4):879, dec 1998.

[26] Alfonso Bueno-Orovio, Elizabeth M. Cherry, and Flavio H. Fenton. Minimal model for human ventricular action potentials in tissue. *Journal of Theoretical Biology*, 253(3):544–560, 2008.

[27] Flavio H. Fenton, Elizabeth M. Cherry, Harold M. Hastings, and Steven J. Evans. Multiple mechanisms of spiral wave breakup in a model of cardiac electrical activity. *Chaos*, 12(3):852–892, 2002.

[28] K.H.W.J. ten Tusscher, D Noble, P J Noble, and A V Panfilov. A model for human ventricular tissue. *AJP - Heart and Circulatory Physiology*, 286(4):H1573–H1589, 2004.

[29] Thomas O'Hara, László Virág, András Varró, and Yoram Rudy. Simulation of the undiseased human cardiac ventricular action potential: Model formulation and experimental validation. *PLoS Computational Biology*, 7(5), 2011.

[30] Blanca Rodríguez, James C Eason, and Natalia Trayanova. Differences between left and right ventricular anatomy determine the types of

reentrant circuits induced by an external electric shock. A rabbit heart simulation study. *Progress in biophysics and molecular biology*, 90(1-3):399–413, 2006.

[31] Martyn P. Nash and Alexander V. Panfilov. Electromechanical model of excitable tissue to study reentrant cardiac arrhythmias. *Progress in Biophysics and Molecular Biology*, 85(2-3):501–522, 2004.

[32] E J Vigmond, R Ruckdeschel, and Natalia Trayanova. Reentry in a morphologically realistic atrial model. *Journal of cardiovascular electrophysiology*, 12(9):1046–54, sep 2001.

[33] R H Clayton, O Bernus, E M Cherry, H Dierckx, Flavio H Fenton, L Mirabella, Alexander V. Panfilov, F B Sachse, Gunnar Seemann, and H Zhang. Models of cardiac tissue electrophysiology: progress, challenges and open questions. *Progress in biophysics and molecular biology*, 104(1-3):22–48, jan 2011.

[34] Charles Roy. The elastic properties of the arterial wall. *Journal of Physiology*, (3):125–159, 1881.

[35] Clifford Truesdell and Walter Noll. *The non-linear field theories of mechanics*. 1965.

[36] A. E. Green, J. E. Adkins, and R. S. Rivlin. Large Elastic Deformations. *Physics Today*, 24:57, 1971.

[37] Y. C. Fung. Elasticity of soft tissues in simple elongation. *The American journal of physiology*, 213(6):1532–1544, 1967.

[38] I. Mirsky. Ventricular and Arterial Wall Stresses Based on Large Deformation Analyses. *Biophysical Journal*, 13(11):1141–1159, 1973.

[39] Gerhard a Holzapfel and Ray W Ogden. Constitutive modelling of passive myocardium: a structurally based framework for material characterization. *Philosophical transactions. Series A, Mathematical, physical, and engineering sciences*, 367(1902):3445–75, 2009.

[40] Julius M. Guccione, Andrew D. McCulloch, and L K Waldman. Passive material properties of intact ventricular myocardium determined from a cylindrical model. *Journal of biomechanical engineering*, 113(February):42–55, 1991.

[41] FC Yin. Ventricular wall stress. *Circulation Research: An official Journal of the American Heart Association*, 49, 1981.

[42] P.J. Hunter and B.H. Smaill. The analysis of cardiac function: A continuum approach. *Progress in Biophysics and Molecular Biology*, 52(2):101–164, 1988.

[43] YC Fung. *Biomechanics: motion, flow, stress and growth*. New York, US, 1990.

[44] AD McCulloch. Cardiac Biomechanics. *The Biomedical Engineering Handbook*, pages 1–28, 1995.

[45] Stuart G Campbell, Elliot Howard, Jazmin Aguado-Sierra, Benjamin a Coppola, Jeffrey H. Omens, Lawrence J Mulligan, Andrew D McCulloch, and Roy C P Kerckhoffs. Effect of transmurally heterogeneous myocyte excitation-contraction coupling on canine left ventricular electromechanics. *Experimental physiology*, 94(5):541–552, 2009.

[46] C. Cherubini, S. Filippi, P. Nardinocchi, and L. Teresi. An electromechanical model of cardiac tissue: Constitutive issues and electrophysiological effects. *Progress in Biophysics and Molecular Biology*, 97(2-3):562–573, 2008.

[47] Sander Land, Steven A. Niederer, and Nicolas P. Smith. Efficient computational methods for strongly coupled cardiac electromechanics. *IEEE Transactions on Biomedical Engineering*, 59(5):1219–1228, 2012.

[48] Steven A. Niederer and Nicolas P. Smith. An improved numerical method for strong coupling of excitation and contraction models in the heart. *Progress in Biophysics and Molecular Biology*, 96(1-3):90–111, 2008.

[49] D Sung, R W Mills, J Schettler, S M Narayan, J H Omens, and A D McCulloch. Ventricular filling slows epicardial conduction and increases action potential duration in an optical mapping study of the isolated rabbit heart. *J Cardiovasc Electrophysiol*, 14(7):739–749, 2003.

[50] John Jeremy Rice, Fei Wang, Donald M Bers, and Pieter P de Tombe. Approximate model of cooperative activation and crossbridge cycling in cardiac muscle using ordinary differential equations. *Biophysical journal*, 95(5):2368–90, 2008.

[51] Sander Land, So-jin Holohan, Nicolas P. Smith, Cristobal G. dos Remedios, Jonathan C Kentish, and Steven A Niederer. A model of cardiac contraction based on novel measurements of tension developement in human cardiomyocites. *Journal of Molecular and Cellular Cardiology*, 2017.

[52] Hiroshi Watanabe, Toshiaki Hisada, Seiryo Sugiura, Jun-ichi Okada, and Hiroshi Fukunari. Computer Simulation of Blood Flow, Left Ventricular Wall Motion and Their Interrelationship by Fluid-Structure Interaction Finite Element Method. *JSME International Journal Series C*, 45(4):1003–1012, 2002.

[53] Young Joon Choi, Jason Constantino, Vijay Vedula, Natalia Trayanova, and Rajat Mittal. A new MRI-based model of heart function with coupled hemodynamics and application to normal and diseased canine left ventricles. *Frontiers in Bioengineering and Biotechnology*, 3(September), 2015.

[54] Hiroshi Watanabe, Seiryo Sugiura, Hidenobu Kafuku, and Toshiaki Hisada. Multiphysics simulation of left ventricular filling dynamics using fluid-structure interaction finite element method. *Biophysical journal*, 87(3):2074–2085, 2004.

[55] Yubing Shi, Yuhui Shi, and Theodosios Korakianitis. Physiological control of an in-series connected pulsatile VAD: numerical simulation study. *Computer Methods in Biomechanics and Biomedical Engineering*, 14(11):995–1007, 2011.

[56] Alfio Quarteroni, Toni Lassila, Simone Rossi, and Ricardo Ruiz-baier. Integrated Heart : Coupling multiscale and multiphysics models for the simulation of the cardiac function. *Computational methods in applied mechanics and Engineering*, 1, 2017.

[57] K H W J Ten Tusscher and A V Panfilov. Cell model for efficient simulation of wave propagation in human ventricular tissue under normal and pathological conditions. *Physics in Medicine and Biology*, 51(23):6141–56, 2006.

[58] A Hosoi, T Washio, and J Okada. A multi-scale heart simulation on massively parallel computers. *International Conference for High Performance Computing*, 2010.

[59] Seiryo Sugiura, Takumi Washio, Asuka Hatano, Junichi Okada, Hiroshi Watanabe, and Toshiaki Hisada. Multi-scale simulations of cardiac electrophysiology and mechanics using the University of Tokyo heart simulator. *Progress in Biophysics and Molecular Biology*, 110(2-3):380–389, 2012.

[60] Martin J. Bishop, Gernot Plank, Rebecca a B Burton, Jürgen E. Schneider, David J. Gavaghan, Vicente Grau, and Peter Kohl. Development of an anatomically detailed MRI-derived rabbit ventricular model and assessment of its impact on simulations of electrophysiological function. *AJP: Heart and Circulatory Physiology*, 298(2):H699–H718, 2010.

[61] William B. Kannel and Robert D. Abbott. A prognostic comparison of asymptomatic left ventricular hypertrophy and unrecognized myocardial infarction : The Framingham study. *American Heart Journal*, 111(2):391–397, 1986.

[62] Jack Lee, Steven Niederer, David Nordsletten, Ian Le Grice, Bruce Smail, David Kay, and Nicolas Smith. Coupling contraction, excitation, ventricular and coronary blood flow across scale and physics in the heart. *Philosophical transactions. Series A, Mathematical, physical, and engineering sciences*, 367(1896):2311–31, jun 2009.

[63] Steven Niederer, Lawrence Mitchell, Nicolas Smith, and Gernot Plank. Simulating human cardiac electrophysiology on clinical time-scales. *Frontiers in Physiology*, APR(April), 2011.

[64] Sara Dutta, Ana Mincholé, Ernesto Zacur, T. Alexander Quinn, Peter Taggart, and Blanca Rodriguez. Early afterdepolarizations promote transmural reentry in ischemic human ventricles with reduced repolarization reserve. *Progress in Biophysics and Molecular Biology*, 120(1-3):236–248, 2016.

[65] Andre Kleber and Yoram Rudy. Basic Mechanisms of Cardiac Impulse Propagation and Associated Arrhythmias. *Physiological Reviews*, 84(2):431–488, 2004.

[66] Dirk Durrer, R. T. Van Dam, G. E. Freud, M. J. Janse, F. L. Meijler, and R. C. Arzbaecher. Total Excitation of the Isolated Human Heart. *Circulation*, 41(6):899–912, 1970.

[67] G Beeler and H Reutert. Reconstruction of the action potential of ventricular myocardial fibres. *Journal of Physiology*, (268):177–210, 1977.

[68] Jeffrey J Fox, Jennifer L McHarg, and Robert F Gilmour. Ionic mechanism of electrical alternans. *American journal of physiology. Heart and circulatory physiology*, 282(2):H516–H530, 2002.

[69] C. H. Luo and Y. Rudy. Original Contributions A Model of the Ventricular Cardiac Action Potential. *Circulation Research*, 68(6):1501–1526, 1991.

[70] T. R. Shannon, F. Wang, J. Puglisi, C. Weber, and D. M. Bers. Erratum: A mathematical treatment of integrated Ca dynamics within the ventricular myocyte (Biophysical Journal (2004) 87 (3351-3371)). *Biophysical Journal*, 102(8):1996–2001, 2012.

[71] Gregory M. Faber and Yoram Rudy. Action Potential and Contractility Changes in [Na+]i Overloaded Cardiac Myocytes: A Simulation Study. *Biophysical Journal*, 78(5):2392–2404, 2000.

[72] B. N. Roberts, P.-C. Yang, S. B. Behrens, J. D. Moreno, and C. E. Clancy. Computational approaches to understand cardiac

electrophysiology and arrhythmias. *AJP: Heart and Circulatory Physiology*, 303(7):H766–H783, 2012.

[73] Jose Vicente, Lars Johannesen, Loriano Galeotti, and David G. Strauss. Mechanisms of sex and age differences in ventricular repolarization in humans. *American Heart Journal*, 168(5):749–756.e3, 2014.

[74] Philip T. Sager, Gary Gintant, J. Rick Turner, Syril Pettit, and Norman Stockbridge. Rechanneling the cardiac proarrhythmia safety paradigm: A meeting report from the Cardiac Safety Research Consortium. *American Heart Journal*, 167(3):292–300, 2014.

[75] Ramon Calderer and Arif Masud. A multiscale stabilized ALE formulation for incompressible flows with moving boundaries. *Computational Mechanics*, 46(1):185–197, 2010.

[76] P.J. Hunter, a.D. McCulloch, and H.E.D.J. ter Keurs. Modelling the mechanical properties of cardiac muscle. *Progress in Biophysics and Molecular Biology*, 69(2-3):289–331, mar 1998.

[77] Guillaume Houzeaux, Mariano Vázquez, R Aubry, and José M Cela. A massively parallel fractional step solver for incompressible flows. *Journal of Computational Physics*, 228(17):6316–6332, 2009.

[78] Mariano Vázquez, Ruth Arís, Guillaume Houzeaux, R Aubry, and P Villar. A massively parallel computational electrophysiology model of the heart. *International journal for numerical methods in biomedical engineering*, 2011.

[79] Mariano Vazquez, Guillaume Houzeaux, Seid Koric, Antoni Artigues, Jazmin Aguado-Sierra, Ruth Aris, Daniel Mira, Hadrien Calmet, Fernando Cucchietti, Herbert Owen, Ahmed Taha, and Jose Maria Cela. Alya: Towards Exascale for Engineering Simulation Codes. pages 1–20, 2014.

[80] E. Casoni, a. Jérusalem, C. Samaniego, B. Eguzkitza, P. Lafortune, D. D. Tjahjanto, X. Sáez, G. Houzeaux, and M. Vázquez. Alya: Computational Solid Mechanics for Supercomputers. *Archives of Computational Methods in Engineering*, 2014.

[81] Benjamin Uekermann, Juan Carlos Cajas, Bernhard Gatzhammer, Guillaume Houzeaux, Miriam Mehl, and Mariano Vazquez. Towards Partitioned Fluid-Structure Interaction on Massively Parallel Systems. *11th World Congress on Computational Mechanics (WCCM XI)*, (Wccm Xi):1–12, 2014.

[82] George Karypis and Vipin Kumar. A Fast and High Quality Multilevel Scheme for Partitioning Irregular Graphs. *SIAM Journal on Scientific Computing*, 20(1):359–392, 1998.

[83] Zygote Media Group Inc. Zygote Solid 3D heart Generation II Developement Report. Technical report, 2014.

[84] M. W. Gee, Ch. Foster, and Wolfgang A. Wall. A computational strategy for prestressing patient-specific biomechanical problems under finite deformation. *International Journal for Numerical Methods in Biomedical Engineering*, 26(1):807–827, 2010.

[85] Hannah Weisbecker, David M Pierce, and Gerhard a Holzapfel. A generalized prestressing algorithm for finite element simulations of preloaded geometries with application to the aorta. *International journal for numerical methods in biomedical engineering*, 30(9):857–72, sep 2014.

[86] Taras Usyk and Andrew D Mcculloch. Relationship Between Regional Shortening and Asynchronous Electrical Activation in a Three-Dimensional Model of Ventricular Electromechanics. *Journal of Cardiovascular Electrophysiology*, 14(s10):S196–S202, 2003.

[87] Roy C. P. Kerckhoffs, Owen P. Faris, Peter H. M. Bovendeerd, Frits W. Prinzen, Karel Smits, Elliot McVeigh, and Theo Arts. Timing of Depolarization and Contraction in the Paced Canine Left Ventricle:. Model and Experiment. *Journal of Cardiovascular Electrophysiology*, 14(s10):S188–S195, 2003.

[88] Ling Xia, Meimei Huo, Qing Wei, Feng Liu, and Stuart Crozier. Analysis of cardiac ventricular wall motion based on a three-dimensional electromechanical biventricular model. *Physics in Medicine and Biology*, 50(8):1901–1917, 2005.

[89] Irvin Teh, Rebecca A.B. Burton, Darryl McClymont, Rebecca A. Capel, Daniel Aston, Peter Kohl, and Jürgen E. Schneider. Mapping cardiac microstructure of rabbit heart in different mechanical states by high resolution diffusion tensor imaging: A proof-of-principle study. *Progress in Biophysics and Molecular Biology*, 121(2):85–96, 2016.

[90] Jason D. Bayer, Robert C. Blake, Gernot Plank, and Natalia A. Trayanova. A novel rule-based algorithm for assigning myocardial fiber orientation to computational heart models. *Annals of Biomedical Engineering*, 40(10):2243–2254, 2012.

[91] Sergey F Pravdin, Vitaly I Berdyshev, Alexander V Panfilov, Leonid B Katsnelson, Olga Solovyova, and Vladimir S Markhasin. Mathematical

model of the anatomy and fibre orientation field of the left ventricle of the heart. *BioMedical Engineering OnLine*, 12(1):54, 2013.

[92] Jonathan Wong and Ellen Kuhl. Generating fibre orientation maps in human heart models using Poisson interpolation. *Computer Methods in Biomechanics and Biomedical Engineering*, 17(11):1217–1226, 2014.

[93] Rubén Doste, David Soto-Iglesias, Gabriel Bernardino, Rafael Sebastian, Sophie Giffard-Roisin, Rocio Cabrera-Lozoya, Maxime Sermesant, Antonio Berruezo, Damián Sánchez-Quintana, and Oscar Camara. A rule-based method to model myocardial fiber orientation for simulating ventricular outflow tract arrhythmias. In *International Conference on Functional Imaging and Modeling of the Heart*, pages 344–353. Springer, 2017.

[94] Mark Potse, Bruno Dubé, and Alain Vinet. A comparison of monodomain and bidomain propagation models for the human heart. *Annual International Conference of the IEEE Engineering in Medicine and Biology - Proceedings*, 53(12):3895–3898, 2006.

[95] Frederick J Vetter, Stephen B Simons, Sergey Mironov, Christopher J Hyatt, and Arkady M Pertsov. Epicardial fiber organization in swine right ventricle and its impact on propagation. *Circulation research*, 96(2):244–251, 2005.

[96] Simon Labarthe, Jason Bayer, Yves Coudière, Jacques Henry, Hubert Cochet, Pierre Jaïs, and Edward Vigmond. A bilayer model of human atria: mathematical background, construction, and assessment. *Europace*, 16(suppl_4):iv21–iv29, 2014.

[97] Pierre Lafortune, Ruth Arís, Mariano Vázquez, and Guillaume Houzeaux. Coupled electromechanical model of the heart : Parallel finite element formulation. *International journal for numerical methods in biomedical engineering*, 28:72–86, 2012.

[98] G. Houzeaux and J. Principe. A variational subgrid scale model for transient incompressible flows. *International Journal of Computational Fluid Dynamics*, 22(3):135–152, 2008.

[99] Guillaume Houzeaux, R Aubry, and Mariano Vázquez. Extension of fractional step techniques for incompressible flows : The preconditioned Orthomin (1) for the pressure Schur complement. *Computers and Fluids*, 44(1):297–313, 2011.

[100] Rainald Lohner, Fernando Mut, Juan Raul Cebral, R Aubry, and Guillaume Houzeaux. Deflated preconditioned conjugate gradient solvers for the pressure-Poisson equation: Extensions and

improvements Rainald. *International journal for numerical methods in Engineering*, (June), 2010.

[101] Alfonso Santiago, M. Zavala, Mariano Vazquez, Juan Carlos Cajas, and Guillaume Houzeaux. HPC-Based Comptact Interface Quasi-Newton Algorithm for Fluid-Structure Interaction. *SIAM Journal on Scientific Computing*, ((submitted)), 2017.

[102] Yuri
Bazilevs, Kenji Takizawa, and Tayfun E. Tezduyar. *Computational Fluid-Structure Interaction*. 2013.

[103] Simone Deparis, Marco Discacciati, and Alfio Quarteroni. A domain decomposition framework for fluid-structure interaction problems. *Computational Fluid Dynamics 2004*, pages 41–58, 2006.

[104] Miriam Mehl, Benjamin Uekermann, Hester Bijl, David Blom, Bernhard Gatzhammer, and Alexander Van Zuijlen. Parallel coupling numerics for partitioned fluid-structure interaction simulations. *Computers and Mathematics with Applications*, 71(4):869–891, 2016.

[105] Christiane Forster, Wolfgang A. Wall, and Ekkehard Ramm. Artificial added mass instabilities in sequential staggered coupling of nonlinear structures and incompressible viscous flows. *Computer Methods in Applied Mechanics and Engineering*, 196(7):1278–1293, 2007.

[106] P. Causin, J. F. Gerbeau, and Fabio Nobile. Added-mass effect in the design of partitioned algorithms for fluid-structure problems. *Computer Methods in Applied Mechanics and Engineering*, 194(42-44):4506–4527, 2005.

[107] Jean-Frédéric Gerbeau, Marina Vidrascu, and Pascal Frey. Fluid-structure interaction in blood flows on geometries based on medical imaging. *Computers & Structures*, 83(2-3):155–165, 2005.

[108] Ulrich Küttler and Wolfgang A. Wall. Fixed-point fluid-structure interaction solvers with dynamic relaxation. *Computational Mechanics*, 43(1):61–72, 2008.

[109] C. G. Broyden. A Class of Methods for Solving Nonlinear Simultaneous Equations. *Mathematics of Computation*, 19(92):577, 1965.

[110] Joris Degroote, Klaus Jürgen Bathe, and Jan Vierendeels. Performance of a new partitioned procedure versus a monolithic procedure in fluid-structure interaction. *Computers and Structures*, 87(11-12):793–801, 2009.

[111] Albert Einstein. The foundation of the generalised theory of relativity. *On a Heuristic Point of View about the Creation and Conversion of Light*, 22:22, 1916.

[112] Klaudius Scheufele. *Robust Quasi-Newton Methods for Partitioned Fluid-Structure Simulations*. PhD thesis, 2015.

[113] Jan Vierendeels, Lieve Lanoye, Joris Degroote, and Pascal Verdonck. Implicit coupling of partitioned fluid-structure interaction problems with reduced order models. *Computers and Structures*, 85(11-14):970–976, 2007.

[114] Dianne P O'Leary and Peter Whitman. Parallel qr factorization by householder and modified gram-schmidt algorithms. *Parallel computing*, 16(1):99–112, 1990.

[115] G. Houzeaux, J. C. Cajas, M. Discacciati, B. Eguzkitza, A. Gargallo-Peiro, M. Rivero, and M. Vazquez. Domain Decomposition Methods for Domain Composition Purpose: Chimera, Overset, Gluing and Sliding Mesh Methods. *Archives of Computational Methods in Engineering*, pages 1–38, 2016.

[116] Daniel Romero, Rafael Sebastian, Bart H. Bijnens, Viviana Zimmerman, Patrick M. Boyle, Edward J. Vigmond, and Alejandro F. Frangi. Effects of the purkinje system and cardiac geometry on biventricular pacing: A model study. *Annals of Biomedical Engineering*, 38(4):1388–1398, 2010.

[117] Mathieu De Craene, Stéphanie Marchesseau, Brecht Heyde, Hang Gao, M Alessandrini, Olivier Bernard, Gemma Piella, AR Porras, Lennart Tautz, Anja Hennemuth, et al. 3d strain assessment in ultrasound (straus): A synthetic comparison of five tracking methodologies. *IEEE transactions on medical imaging*, 32(9):1632–1646, 2013.

[118] Thomas Fritz, Christian Wieners, Gunnar Seemann, Henning Steen, and Olaf Dossel. Simulation of the contraction of the ventricles in a human heart model including atria and pericardium: Finite element analysis of a frictionless contact problem. *Biomechanics and Modeling in Mechanobiology*, 13(3):627–641, 2014.

[119] Alfonso Santiago, Jazmin Aguado-Sierra, M. Zavala, Ruben Doste-Beltran, Samuel Gomez, Ruth Arís, Eva Casoni, and Mariano Vazquez. Fluid-electro-mechanical model of the human heart for supercomputers. *International Journal for Numerical Methods in Biomedical Engineering (submitted)*, 2017.

[120] Y. Bazilevs, J. R. Gohean, T. J R Hughes, R. D. Moser, and Y. Zhang. Patient-specific isogeometric fluid-structure interaction analysis of thoracic aortic blood flow due to implantation of the Jarvik 2000 left ventricular assist device. *Computer Methods in Applied Mechanics and Engineering*, 198(45-46):3534–3550, 2009.

[121] Wei Sun. Simulated Bioprosthetic Heart Valve Deformation under Quasi-Static Loading. *Journal of Biomechanical Engineering*, 127(6):905, jul 2005.

[122] Matteo Astorino, J. F. Gerbeau, Olivier Pantz, and K. F. Traoré. Fluid-structure interaction and multi-body contact: Application to aortic valves. *Computer Methods in Applied Mechanics and Engineering*, 198(45-46):3603–3612, 2009.

[123] Boyce E. Griffith. Immersed boundary model of aortic heart valve dynamics with physiological driving and loading conditions. *International journal for numerical methods in biomedical engineering*, pages 1–29, 2011.

[124] David Kamensky, Ming-chen Hsu, Dominik Schillinger, John A Evans, Ankush Aggarwal, Michael S Sacks, and Thomas J. R. Hughes. A variational immersed boundary framework for fluid - structure interaction : Isogeometric implementation and application to bioprosthetic heart valves. *ICES REPORT 14-12*, 2014.

[125] Matthew J. Gonzales, Gregory Sturgeon, Adarsh Krishnamurthy, Johan Hake, René Jonas, Paul Stark, Wouter Jan Rappel, Sanjiv M. Narayan, Yongjie Zhang, W. Paul Segars, and Andrew D. McCulloch. A three-dimensional finite element model of human atrial anatomy: New methods for cubic Hermite meshes with extraordinary vertices. *Medical Image Analysis*, 17(5):525–537, 2013.

[126] Steven a Niederer, Eric Kerfoot, Alan P Benson, Miguel O Bernabeu, Olivier Bernus, Chris Bradley, Elizabeth M Cherry, Richard Clayton, Flavio H Fenton, Alan Garny, Elvio Heidenreich, Sander Land, Mary Maleckar, Pras Pathmanathan, Gernot Plank, José F Rodríguez, Ishani Roy, Frank B Sachse, Gunnar Seemann, Ola Skavhaug, and Nic P Smith. Verification of cardiac tissue electrophysiology simulators using an N-version benchmark. *Philosophical transactions. Series A, Mathematical, physical, and engineering sciences*, 369(1954):4331–51, nov 2011.

[127] Guillaume Houzeaux, Raúl de la Cruz, Herbert Owen, and Mariano Vázquez. Parallel uniform mesh multiplication applied to a Navier-Stokes solver. *Computers and Fluids*, 80(1):142–151, 2013.

[128] JP Keener. Propagation and its failure in coupled systems of discrete excitable cells. *SIAM Journal on Applied Mathematics*, 47(3):556–572, 1987.

[129] P. Pathmanathan, M.O. Bernabeu, S.A. Niederer, D.J. Gavaghan, and D. Kay. Computational modelling of cardiac electrophysiology: explanation of the variability of results from different numerical solvers. *International Journal for Numerical Methods in Biomedical Engineering*, 28(8):890–903, aug 2012.

[130] Hermenegild Arevalo, Blanca Rodriguez, and Natalia Trayanova. Arrhythmogenesis in the heart: Multiscale modeling of the effects of defibrillation shocks and the role of electrophysiological heterogeneity. *Chaos (Woodbury, N.Y.)*, 17(1):015103, mar 2007.

[131] R. I. Griffiths. Shortening of muscle fibres during stretch of the active cat medial gastrocnemius muscle: the role of tendon compliance. *Journal of Physiology*, 436:219–236, 1991.

[132] L. Zhong, L. Gobeawan, Y. Su, J.-L. Tan, D. Ghista, T. Chua, R.-S. Tan, and G. Kassab. Right ventricular regional wall curvedness and area strain in patients with repaired tetralogy of Fallot. *AJP: Heart and Circulatory Physiology*, 302:H1306–H1316, 2012.

[133] Martino Alessandrini, Bidisha Chakraborty, Brecht Heyde, Olivier Bernard, Mathieu De Craene, Maxime Sermesant, and Jan Dhooge. Realistic vendor-specific synthetic ultrasound data for quality assurance of 2d speckle tracking echocardiography: Simulation pipeline and open access database. *IEEE Transactions on Ultrasonics, Ferroelectrics, and Frequency Control*, 2017.

[134] Leonid Zhukov and Alan H. Barr. Heart-Muscle Fiber Reconstruction from Diffusion Tensor MRI. *Proceedings of the IEEE Visualization Conference*, (4):597–602, 2003.

[135] James D. Thomas and Zoran B. Popović. Assessment of Left Ventricular Function by Cardiac Ultrasound. *Journal of the American College of Cardiology*, 48(10):2012–2025, 2006.

[136] Partho P. Sengupta, Josef Korinek, Marek Belohlavek, Jagat Narula, Mani A. Vannan, Arshad Jahangir, and Bijoy K. Khandheria. Left Ventricular Structure and Function. Basic Science for Cardiac Imaging. *Journal of the American College of Cardiology*, 48(10):1988–2001, 2006.

[137] Jaroslav Hron and Stefan Turek. Proposal for numerical benchmarking of fluid-structure interaction between an elastic object and laminar incompressible flow. *Fluid-Structure Interaction*, 53:371–385, 2006.

[138] Catalina Tobon-Gomez, Mathieu De Craene, Kristin Mcleod, Lennart Tautz, Wenzhe Shi, Anja Hennemuth, Adityo Prakosa, Hengui Wang, Gerry Carr-White, Stam Kapetanakis, et al. Benchmarking framework for myocardial tracking and deformation algorithms: An open access database. *Medical image analysis*, 17(6):632–648, 2013.

[139] C C Moore, E R McVeigh, and E A Zerhouni. Quantitative tagged magnetic resonance imaging of the normal human left ventricle. *Topics in magnetic resonance imaging : TMRI*, 11(6):359–71, 2000.

[140] Leon Axel, Albert Montillo, and Daniel Kim. Tagged magnetic resonance imaging of the heart: A survey. *Medical Image Analysis*, 9(4 SPEC. ISS.):376–393, 2005.

[141] Nico
Bruining, Clemens Von Birgelen, Pim J. De Feyter, Jurgen Ligthart, Wenguang Li, Patrick W. Serruys, and Jos R.T.C. Roelandt. ECG-gated versus nongated three-dimensional intracoronary ultrasound analysis: Implications for volumetric measurements. *Catheterization and Cardiovascular Diagnosis*, 43(3):254–261, 1998.

[142] Rainer Hoffmann, Giuseppe Barletta, Stephan von Bardeleben, Jean Louis Vanoverschelde, Jaroslaw Kasprzak, Christian Greis, and Harald Becher. Analysis of left ventricular volumes and function: a multicenter comparison of cardiac magnetic resonance imaging, cine ventriculography, and unenhanced and contrast-enhanced two-dimensional and three-dimensional echocardiography. *Journal of the American Society of Echocardiography*, 27(3):292–301, 2014.

[143] Mir-Hossein Moosavi, Nasser Fatouraee, Hamid Katoozian, Ali Pashaei, Oscar Camara, and Alejandro F Frangi. Numerical simulation of blood flow in the left ventricle and aortic sinus using magnetic resonance imaging and computational fluid dynamics. *Computer methods in biomechanics and biomedical engineering*, 17(7):740–749, 2014.

[144] Leidulf Segadal and Knut Matre. Blood velocity distribution in human ascending aorta. *Circulation of diagnose methods in valvular heart disease*, 76(December 1987):2416–2422, 1987.

[145] J. C. R. Hunt, A. A. Wray, and P. Moin. Eddies, Streams, and Convergence Zones in Turbulent Flows. *Center of Turbulence Research*, (1988), 1988.

[146] Pinaki Chakraborty, S. Balachandar, and Ronald J. Adrian. On the relationships between local vortex identification schemes. *Journal of Fluid Mechanics*, 535:189–214, 2005.

[147] El-Sayed H Ibrahim, Kevin R Johnson, Alan B Miller, Jean M Shaffer, and Richard D White. Measuring aortic pulse wave velocity using high-field cardiovascular magnetic resonance: comparison of techniques. *Journal of cardiovascular magnetic resonance : official journal of the Society for Cardiovascular Magnetic Resonance*, 12(1):26, 2010.

[148] John Peder Escobar Kvitting, Tino Ebbers, Lars Wigström, Jan Engvall, Christian L. Olin, and Ann F. Bolger. Flow patterns in the aortic root and the aorta studied with time-resolved, 3-dimensional, phase-contrast magnetic resonance imaging: Implications for aortic valve-sparing surgery. *Journal of Thoracic and Cardiovascular Surgery*, 127(6):1602–1607, 2004.

[149] Michael Markl, Mary T. Draney, D. Craig Miller, Jonathan M. Levin, Eric E. Williamson, Norbert J. Pelc, David H. Liang, and Robert J. Herfkens. Time-resolved three-dimensional magnetic resonance velocity mapping of aortic flow in healthy volunteers and patients after valve-sparing aortic root replacement. *Journal of Thoracic and Cardiovascular Surgery*, 130(2):456–463, 2005.

[150] E. Soudah, J. Casacuberta, P. J. Gamez-Montero, J. S. Perez, M. Rodriguez-Cancio, G. Raush, C. H. Li, F. Carreras, and R. Castilla. Estimation of Wall Shear Stress Using 4D Flow Cardiovascular Mri and Computational Fluid Dynamics. *Journal of Mechanics in Medicine and Biology*, 17(03):1750046, 2017.

[151] Zoran Stankovic, Bradley D Allen, Julio Garcia, Kelly B Jarvis, and Michael Markl. 4D flow imaging with MRI. *Cardiovascular diagnosis and therapy*, 4(2):173–92, 2014.

[152] Michael Markl and Philip J Kilner. Comprehensive 4D velocity mapping of the heart and great vessels by cardiovascular magnetic resonance. *Journal of Cardiovascular Magnetic Resonance*, 13(1):7, 2011.

[153] Jacob I. Haft, Michael V. Herman, and Richard Gorlin. Left bundle branch block: Etiologic, Hemodynamic and Ventriculographic Considerations. *Circulation*, XLIII, 1971.

[154] Cindy L. Grines, Thomas M. Bashore, Harisios Boudoulas, Shari Olson, Phillip Shafer, and Charles F. Wooley. Functional Abnormalities in Isolated Left Bundle Branch Block: The effect of Interventricular Asynchrony. *Circulation*, 79(4):845–853, 1988.

[155] Chirine Parsai, Bart Bijnens, George Ross Sutherland, Aigul Baltabaeva, Piet Claus, MacIej Marciniak, Vince Paul, Mike Scheffer, Erwan Donal, Genevive Derumeaux, and Lisa Anderson. Toward

understanding response to cardiac resynchronization therapy: Left ventricular dyssynchrony is only one of multiple mechanisms. *European Heart Journal*, 30(8):940–949, 2009.

[156] Simon G. Duckett, Oscar Camara, Matthew R. Ginks, Julian Bostock, Phani Chinchapatnam, Maxime Sermesant, Ali Pashaei, Pier D. Lambiase, Jaswinder S. Gill, Gerry S. Carr-White, Alejandro F. Frangi, Reza Razavi, Bart H. Bijnens, and C. Aldo Rinaldi. Relationship between endocardial activation sequences defined by high-density mapping to early septal contraction (septal flash) in patients with left bundle branch block undergoing cardiac resynchronization therapy. *Europace*, 14(1):99–106, 2012.

[157] M Sermesant, R Chabiniok, P Chinchapatnam, T Mansi, F Billet, P Moireau, J M Peyrat, K Wong, J Relan, K Rhode, M Ginks, P Lambiase, H Delingette, M Sorine, C a Rinaldi, D Chapelle, R Razavi, and N Ayache. Patient-specific electromechanical models of the heart for the prediction of pacing acute effects in CRT: a preliminary clinical validation. *Medical image analysis*, 16(1):201–15, jan 2012.

[158] C. Tobon-Gomez, N. Duchateau, R. Sebastian, S. Marchesseau, O. Camara, E. Donal, M. De Craene, A. Pashaei, J. Relan, M. Steghofer, P. Lamata, H. Delingette, S. Duckett, M. Garreau, A. Hernandez, K. S. Rhode, M. Sermesant, N. Ayache, C. Leclercq, R. Razavi, N. P. Smith, and A. F. Frangi. Understanding the mechanisms amenable to CRT response: From pre-operative multimodal image data to patient-specific computational models. *Medical and Biological Engineering and Computing*, 51(11):1235–1250, 2013.

[159] Jonathan M. Behar, Tom Jackson, Eoin Hyde, Simon Claridge, Jaswinder Gill, Julian Bostock, Manav Sohal, Bradley Porter, Mark O'Neill, Reza Razavi, Steve Niederer, and Christopher Aldo Rinaldi. Optimized Left Ventricular Endocardial Stimulation Is Superior to Optimized Epicardial Stimulation in Ischemic Patients With Poor Response to Cardiac Resynchronization Therapy. *JACC: Clinical Electrophysiology*, 2(7), 2016.

[160] Thomas Pheiffer, David Soto-iglesias, Yaroslav Nikulin, Tiziano Passerini, Julian Krebs, Marta Sitges, Antonio Berruezo, Oscar Camara, and Tommaso Mansi. Functional Imaging and Modelling of the Heart. 10263:239–248, 2017.

[161] Fijoy Vadakkumpadan, Hermenegild Arevalo, Can Ceritoglu, Michael Miller, and Natalia Trayanova. Image-Based Estimation of

Myocardial Fiber Orientations for Patient-Specific Models of Cardiac Electrophysiology. *Heart Rhythm*, 6(11):1688–1688, 2009.

[162] C. Tobon-Gomez, N. Duchateau, R. Sebastian, S. Marchesseau, O. Camara, E. Donal, M. De Craene, A. Pashaei, J. Relan, M. Steghofer, P. Lamata, H. Delingette, S. Duckett, M. Garreau, A. Hernandez, K. S. Rhode, M. Sermesant, N. Ayache, C. Leclercq, R. Razavi, N. P. Smith, and A. F. Frangi. Understanding the mechanisms amenable to CRT response: From pre-operative multimodal image data to patient-specific computational models. *Medical and Biological Engineering and Computing*, 51(11):1235–1250, 2013.

[163] François Faure, Christian Duriez, Hervé Delingette, Jérémie Allard, Benjamin Gilles, Stéphanie Marchesseau, Hugo Talbot, Hadrien Courtecuisse, Guillaume Bousquet, Igor Peterlik, et al. Sofa: A multi-model framework for interactive physical simulation. In *Soft Tissue Biomechanical Modeling for Computer Assisted Surgery*, pages 283–321. Springer, 2012.

[164] Henrik Finsberg, Gabriel Balaban, Stian Ross, Trine F. Håland, Hans Henrik Odland, Joakim Sundnes, and Samuel Wall. Estimating cardiac contraction through high resolution data assimilation of a personalized mechanical model. *Journal of Computational Science*, 2017.

[165] Pietro Francia, Cristina Balla, Francesco Paneni, and Massimo Volpe. Left bundle-branch block - pathophysiology, prognosis, and clinical management. *Clinical Cardiology*, 30(3):110–115, mar 2007.

[166] Hoa L. Nguyen, Darleen Lessard, Frederick A. Spencer, Jorge Yarzebski, Juan C. Zevallos, Joel M. Gore, and Robert J. Goldberg. Thirty-year trends (1975-2005) in the magnitude and hospital death rates associated with complete heart block in patients with acute myocardial infarction: A population-based perspective. *American Heart Journal*, 156(2):227–233, 2008.

[167] Gustavo Abuin, Alejandro Nieponice, Adelina Rojas-granados, and Patricia Herrera-saint Leu. Anatomical Reasons for the Discrepancies in Atrioventricular Block. 36(1):8–11, 2009.

[168] Reinaldo B. Bestetti, Patrícia M. Cury, Tatiana A D Theodoropoulos, and Daniel Villafanha. Trypanosoma cruzi myocardial infection reactivation presenting as complete atrioventricular block in a Chagas' heart transplant recipient. *Cardiovascular Pathology*, 13(6):323–326, 2004.

[169] Kenneth Dickstein, Panos E Vardas, Angelo Auricchio, Jean-Claude Daubert, Cecilia Linde, John McMurray, Piotr Ponikowski, Silvia Giuliana Priori, Richard Sutton, Dirk J Van Veldhuisen, et al. 2010 focused update of esc guidelines on device therapy in heart failure: An update of the 2008 esc guidelines for the diagnosis and treatment of acute and chronic heart failure and the 2007 esc guidelines for cardiac and resynchronization therapy developed with the special contribution of the heart failure association and the european heart rhythm association. *European heart journal*, 31(21):2677–2687, 2010.

[170] Patrick Houthuizen, Frank ALE Bracke, and Berry M van Gelder. Atrioventricular and interventricular delay optimization in cardiac resynchronization therapy: physiological principles and overview of available methods. *Heart failure reviews*, 16(3):263, 2011.

[171] Robert H. Helm, Melissa Byrne, Patrick A. Helm, Samantapudi K. Daya, Nael F. Osman, Richard Tunin, Henry R. Halperin, Ronald D. Berger, David A. Kass, and Albert C. Lardo. Three-dimensional mapping of optimal left ventricular pacing site for cardiac resynchronization. *Circulation*, 115(8):953–961, 2007.

[172] A. L A J Dekker, B. Phelps, B. Dijkman, T. Van Der Nagel, F. H. Van Der Veen, G. G. Geskes, and J. G. Maessen. Epicardial left ventricular lead placement for cardiac resynchronization therapy: Optimal pace site selection with pressure-volume loops. *Journal of Thoracic and Cardiovascular Surgery*, 127(6):1641–1647, 2004.

[173] Nirmal Panthee, Jun-Ichi Okada, Takumi Washio, Youhei Mochizuki, Ryohei Suzuki, Hidekazu Koyama, Minoru Ono, Toshiaki Hisada, and Seiryo Sugiura. Tailor-made heart simulation predicts the effect of cardiac resynchronization therapy in a canine model of heart failure. *Medical image analysis*, 31:46–62, 2016.

[174] Cheuk-Man Yu and David L. Hayes. Cardiac resynchronization therapy: state of the art 2013. *European Heart Journal*, 34(19):1396–1403, 2013.

[175] Frits W. Prinzen, Kevin Vernooy, and Angelo Auricchio. Cardiac resynchronization therapy: State-of-the-art of current applications, guidelines, ongoing trials, and areas of controversy. *Circulation*, 128(22):2407–2418, 2013.

[176] O. S. Narula, B. J. Scherlag, R. Javier, F. Hildner, and P. Samet. Analysis of the AV Conduction Defect in Complete Heart Block Utilizing His Bundle Electrograms.

[177] Dwight Reynolds, Gabor Z. Duray, Razali Omar, Kyoko Soejima, Petr Neuzil, Shu Zhang, Calambur Narasimhan, Clemens Steinwender, Josep Brugada, Michael Lloyd, Paul R. Roberts, Venkata Sagi, John Hummel, Maria Grazia Bongiorni, Reinoud E. Knops, Christopher R. Ellis, Charles C. Gornick, Matthew A. Bernabei, Verla Laager, Kurt Stromberg, Eric R. Williams, J. Harrison Hudnall, Philippe Ritter, and Micra Transcatheter Pacing Study Group. A Leadless Intracardiac Transcatheter Pacing System. *The New England journal of medicine*, 374(6):151109124543001, 2015.

[178] Samuel Asirvatham, K. L. Venkatachalam, and Suraj Kapa. *Remote Monitoring and Physiologic Sensing Technologies and Applications, An Issue of Cardiac Electrophysiology Clinics, Volume 5-3*. Elsevier, Philadelphia, 1 edition, 2013.

[179] Pablo J Blanco, Jorge S Leiva, and Gustavo C Buscaglia. A black-box decomposition approach for coupling heterogeneous components in hemodynamics simulations. *International journal for numerical methods in biomedical engineering*, 29(November 2012):408–427, 2013.

[180] Jorge S Leiva, Pablo J Blanco, and Gustavo C Buscaglia. Partitioned Analysis for Dimensionally-Heterogeneous Hydraulic Networks. *Multiscale Modeling & Simulation*, 9(2):872–903, apr 2011.

[181] Pablo Blanco, Sansuke Watanabe, Marco Passos, Pedro Lemos, and Raul A. Feijóo. An anatomically detailed arterial network model for one-dimensional computational hemodynamics. *IEEE transactions on biomedical engineering*, 9294(c):1–18, oct 2014.

[182] Pablo J Blanco, Jorge S Leiva, Raul A. Feijóo, and Gustavo C. Buscaglia. Black-box decomposition approach for computational hemodynamics: One-dimensional models. *Computer Methods in Applied Mechanics and Engineering*, 200(13-16):1389–1405, mar 2011.

To see the world, things dangerous to come to,
to see behind walls, draw closer,
to find each other, and feel
- that is the purpose of life.